JOURNAL OF PETROLOGY | VOLUME 52 | NUMBER 9 | PAGES 1679–1735 | 2011 | doi:10.1093/petrology/egr026

Petrogenesis of Pyroxenites and Melt Infiltrations in the Ultramafic Complex of Beni Bousera, Northern Morocco

ALEXANDER P. GYSI[1,2]*, OLIVER JAGOUTZ[3], MAX W. SCHMIDT[2] AND KAMAL TARGUISTI[4]

[1]INSTITUTE OF EARTH SCIENCES, UNIVERSITY OF ICELAND, 101 REYKJAVIK, ICELAND

[2]INSTITUTE OF GEOCHEMISTRY AND PETROLOGY, ETH, 8092 ZURICH, SWITZERLAND

[3]DEPARTMENT OF EARTH, ATMOSPHERIC, AND PLANETARY SCIENCES, MASSACHUSETTS INSTITUTE OF TECHNOLOGY, CAMBRIDGE, MA 02139-4307, USA

[4]FACULTÉ DES SCIENCES, UNIVERSITÉ ABDELMALEK ESSAÂDI, 2121 TÉTOUAN, MOROCCO

RECEIVED DECEMBER 28, 2009; ACCEPTED MAY 3, 2011
ADVANCE ACCESS PUBLICATION AUGUST 3, 2011

The origin of pyroxenites and their relation to melt migration in the mantle have been investigated in two pyroxenite-rich zones in the Beni Bousera massif. Based on combined field, microtextural, mineralogical and geochemical observations, the pyroxenites were separated into four types. Type-I Cr-diopside websterites contain bright green diopside and have primitive bulk Ni, Cr and Mg-number. Their trace element systematics are characterized by slight light rare earth element (LREE) enrichment compared with the middle (MREE) and heavy (H) REE, and negative high field strength element (HFSE) anomalies in bulk-rock and mineral compositions suggesting that they result from melting of metasomatized mantle. Trace element concentrations of melts calculated to be in equilibrium with Type-I cpx have a subduction-like signature and show a close similarity to certain lavas erupted in the Alboran Basin. Calculated mineral equilibration temperatures of ~1200 to 1350°C are close to the basalt liquidus and higher than for other pyroxenite types in Beni Bousera, which generally yield <1100°C. Type-II spinel websterites are also primitive, but contain augitic clinopyroxene; their whole-rock compositions are characterized by high Ti, Ni, and Mg-number, intermediate Cr and trace element patterns with LREE depletion over the MREE and HREE. Type-III garnet pyroxenites, which include the famous diamond-pseudomorph-bearing garnet pyroxenites, are more evolved than Types-I and -II and have low and variable Mg-number correlating with an Fe-enrichment trend. High bulk-rock and garnet HREE to LREE ratios result from high-pressure fractionation of garnet and augitic cpx at calculated pressures of >45 to 20–30 kbar. Type-III pyroxenites display strong variations of LREE and HFSE depletion and strong bulk Nb/Ta fractionation. Calculated melts in equilibrium with augitic cpx are variably enriched in incompatible trace elements similar to intraplate basalts. Type-IV pyroxenites are composed of green diopside, opx, garnet and plagioclase and/or spinel. Whole-rocks have high Na_2O, CaO and Al_2O_3 concentrations and high Mg-number, are HREE depleted, and have positive Eu and Sr anomalies. Garnets are characterized by low HREE/MREE and positive Eu anomalies. The absence of bulk-rock HREE enrichment indicates a metamorphic origin for this garnet, which is corroborated by the presence of Al-rich metamorphic spinels. Relict magmatic plagioclase indicates a shallower (<10 kbar) crustal origin for these pyroxenites. Their metamorphic assemblage yields temperatures and pressures of 800–980°C and 14 kbar, indicating a pressure increase during the metamorphic overprint. The whole-rock geochemistry of Type-IV pyroxenites is comparable with that of rocks from the lower crustal section of the Kohistan (northern Pakistan) paleo-arc, indicating a possible origin of these rocks as cumulates in the deeper arc crust and subsequent delamination into the underlying mantle.

KEY WORDS: *mantle geochemistry; metasomatism; pyroxenites; refertilization; ultramafic; mafic; REE; clinopyroxene; garnet*

*Corresponding author. Telephone: +354 5255248. E-mail: apg2@hi.is

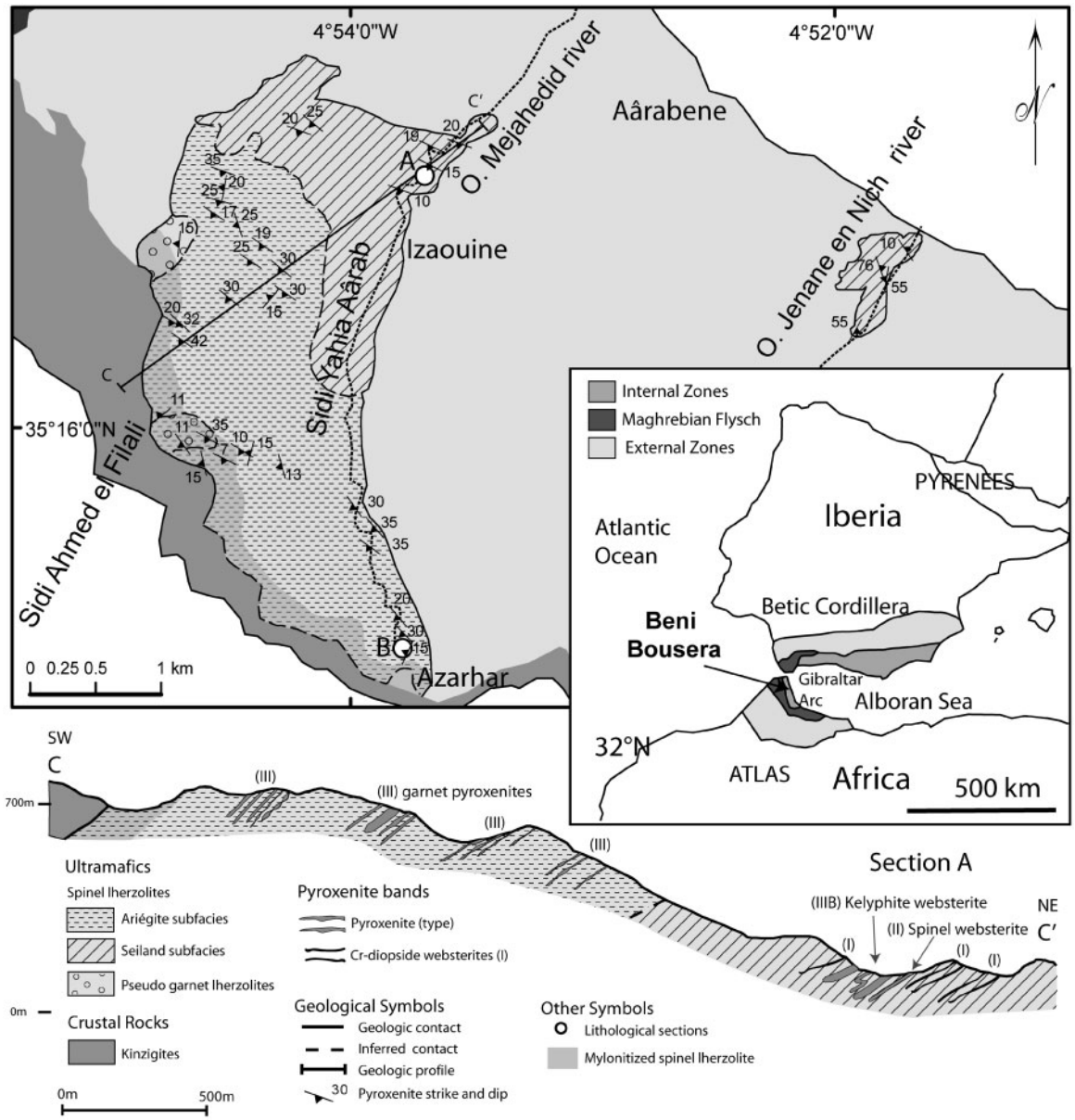

Fig. 1. Geological map and NE–SW profile of the valley of Sidi Yahia Aârab in the Beni Bousera massif, northern Morocco. Also shown on the map are the locations of sections A and B, and a schematic structural map of the western Mediterranean region. Peridotite body and kinzigites after Kornprobst (1969). Ariegite and Seiland subfacies of spinel lherzolites following the definition of O'Hara (1968). Pyroxenites in the profile are exaggerated in size for schematic representation.

INTRODUCTION

The nature and origin of mantle heterogeneities is a long-standing problem in the Earth Sciences. Mantle rocks are brought to the surface as kilometer-scale tectonic slivers (so-called alpine-type peridotites) or as small centimeter- to decimeter-scale xenoliths in volcanic eruptions. In contrast to the mantle xenoliths exhumed by alkali basalts and kimberlites, alpine-type peridotites allow assessment of large-scale mantle heterogeneities and have not necessarily interacted with large ion lithophile element (LILE)-enriched magmas, yet might record multiple, complex subsolidus re-equilibration processes. Thus, large-scale mantle outcrops such as the Beni Bousera massif in northern Morocco and the Ronda massif in southern Spain (Fig. 1) can provide valuable insights into upper mantle processes (e.g. Blichert-Toft *et al.*, 1999). Both massifs are famous for their abundant and highly variable, partly garnet-bearing, pyroxene-rich rocks (Kornprobst, 1969; Pearson *et al.*, 1989, 1991, 1993; Kornprobst *et al.*, 1990;

Davies *et al.*, 1993; Kumar *et al.*, 1996; Garrido & Bodinier, 1999; Morishita *et al.*, 2001; Pearson & Nowell, 2004; Bodinier *et al.*, 2008). Understanding the origin of these (garnet-) pyroxenites allows constraints to be made on melt–mantle interaction, which in turn contributes to greater understanding of the chemical characteristics of the source of mid-ocean ridge basalts (MORB) (Hirschmann & Stolper, 1996).

The origin of the pyroxenites remains a subject for debate. The parental melts may result from partial melting of the surrounding host peridotite, and may have experienced various degrees of crystal fractionation and melt–rock reaction (Kornprobst, 1969; Dickey, 1970; Obata, 1980). Nevertheless, isotopic data provide evidence for disequilibrium between some of the pyroxenites and the surrounding peridotites, implying that some represent crystal segregations from melts not directly derived from the host peridotite (Suen & Frey, 1987; Pearson *et al.*, 1991, 1993; Kumar *et al.*, 1996; Pearson & Nowell, 2004). Alternatively, other pyroxenites have been considered to represent metamorphosed basalts and gabbros that were formerly parts of subducted oceanic crust (Kornprobst *et al.*, 1990) that has been stretched and thinned in the convecting mantle (Allègre & Turcotte, 1986).

For the pyroxenites of Beni Bousera, various formation mechanisms have been suggested. Kornprobst *et al.* (1990) subdivided the garnet pyroxenites into two geochemically defined groups. Type-I pyroxenites are characterized by an Fe-enrichment trend and thought to represent high-pressure crystal cumulates. Type-II are characterized by high and nearly constant Mg/Fe ratios and variable Ca and Al concentrations, and include corundum-bearing garnet pyroxenites interpreted as fragments of recrystallized subducted gabbroic oceanic crust. Based on isotopic studies, Pearson *et al.* (1991, 1993) and Pearson & Nowell (2004) suggested that most of the garnet pyroxenites represent high-pressure crystal segregates from melts originating from hydrothermally altered subducted oceanic crust. Although garnet-free pyroxenites are frequently observed in the Beni Bousera massif, they have been mainly studied in composite garnet pyroxenite bands characterized by symmetrical zoning and interpreted to result from high-pressure fractionation of magmas migrating along conduits (e.g. Kornprobst, 1969; Pearson *et al.*, 1993; Kumar *et al.*, 1996). In the Ronda massif, Cr-diopside websterites have been interpreted to represent hot asthenospheric melts infiltrating the base of the lithospheric mantle during the Alboran Sea rifting (Van der Wal & Vissers, 1993; Van der Wal & Bodinier, 1996; Garrido & Bodinier, 1999; Lenoir *et al.*, 2001). Similar bands occur in the central parts of the Beni Bousera massif but have never been investigated in detail.

In this study we present petrographic and compositional data for a large variety of pyroxenite and peridotite samples from Beni Bousera with emphasis on two detailed field sections. One sample from the famous garnet pyroxenites containing graphite pseudomorphs after diamond (Slodkevitch, 1983; Pearson *et al.*, 1989, 1993), exposed to the SE of one of our sections (B in Fig. 1), was included to document its relation to the other garnet pyroxenites in the massif.

GEOLOGICAL SETTING

The Beni Bousera massif extends over an area of 75 km^2 in the Rif mountains, 60 km SE of Tetouan, on the Alboran coast of northern Morocco. Together with the Ronda massif, it forms part of the arcuate Betic–Rif orogenic belt forming an orocline around the Alboran Sea with the Gibraltar arc located at the westernmost end (Fig. 1). The Betic–Rif orogen consists of the Alboran Terrane thrust over the African and Iberian margins (Chalouan *et al.*, 2001; Michard *et al.*, 2002). The Rif is divided into three structural domains (Chalouan & Michard, 2004): the External Zones, the Maghrebian Flysch Nappes and the Internal Zones (Fig. 1). Beni Bousera belongs to the Sebtide nappes of the Internal Zones, more precisely to the Beni Bousera unit composed of kinzigites (granulitic lower crust) surrounding the ultramafic rocks, together forming a late anticlinal structure with a NW–SE-oriented fold axis (Kornprobst, 1969). The peridotites in the Beni Bousera massif are mainly spinel lherzolites, harzburgites and minor amounts of dunite. Pyroxenite bands constitute up to 5–10% of the massif and are associated with zones that are highly variable in their mineralogy, geochemistry and deformation structures (e.g. Kornprobst, 1969; Draoui, 1992; Pearson *et al.*, 1993). The presence of graphite pseudomorphs after diamond in garnet pyroxenites in both the Beni Bousera and Ronda massifs constrains the depth of origin of the melts forming these pyroxenites to >150 km; that is, within the diamond stability field (Slodkevitch, 1983; Pearson *et al.*, 1989, 1993; Davies *et al.*, 1993). During Oligocene–Miocene times, slab retreat and a rapid phase of extension in the Alboran Sea back-arc domain resulted in uplift and Neogene emplacement of the mantle peridotite bodies into the crust at about 22 Ma (e.g. Loomis, 1972; Reisberg *et al.*, 1989; Blichert-Toft *et al.*, 1999; Pearson & Nowell, 2004).

FIELD RELATIONS

Our study area is located in the northwestern part of the Beni Bousera massif in the valley of Sidi Yahia Aârab, transected by the Oued Mejahedid river originating near Azarhar in the south and flowing north in the direction of Aârabene. The pyroxenites form bands and/or dykes of different types and are mostly concordant with the SW-dipping general foliation. Rare isoclinal folds indicate an at least locally strong ductile deformation (Kornprobst,

1969). The geological map of the Ministère de l'Énergie et des Mines (Royaume du Maroc, carte géologique du Rif, Bou Ahmed, 1/50 000) gives an overview of the geology of the peridotite body and the surrounding Sebtide nappes composed of micaschists, gneisses, kinzigites–granulites and metasediments. A new detailed geological map covering ~10 km^2 and a SW–NE geological profile are presented in this study, showing the spatial distribution of spinel lherzolites and pyroxenites (Fig. 1). On the map we have differentiated areas affected by metamorphic overprinting in the Seiland subfacies of spinel lherzolite (north, NW and central parts of the massif) from areas where relicts from the ariegite subfacies (south, SW and west) are more abundant and consequently garnet pyroxenites are more frequently observed. 'Pseudo' garnet peridotites are found at the structural top of the massif (west) and have been interpreted to originate from tectonic mixing of garnet pyroxenites with the host peridotite through deformation at decreasing temperatures (Tabit *et al.*, 1997). The border zone between the ultramafic rock and the kinzigites is characterized by intense shear deformation and mylonitized peridotites. Localized areas of the massif are heavily intruded by granitic dykes and veins, especially towards the border zones. These granites have quartz and feldspars forming eutectic intergrowths, and contain black tourmaline and vermiculite among other minerals. The granitic dykes may amount to as much as 5–10% of an outcrop and in these areas the peridotites are heavily serpentinized and weathered. Generally, however, the massif shows only a low degree of serpentinization with small black serpentine veins cross-cutting the peridotites locally and in 3–10 cm thick faults.

Pyroxenites are unevenly distributed throughout the massif. Whereas centimeter-thick pyroxenite bands are sporadically present throughout the entire massif, garnet pyroxenites and Cr-diopside pyroxenites (Kornprobst *et al.*, 1990; Pearson *et al.*, 1993) constitute up to 40–80 vol. % of the outcrop in restricted zones up to hundreds of meters wide. Within such pyroxenite-rich zones, most of the pyroxenite dykes are significantly thicker (tens of centimeters to meters) and usually associated with replacive dunites, harzburgites and refertilized lherzolites, referred to here as 'secondary lherzolites'. The latter are characterized by a honeycomb texture of pyroxene grains interstitial to larger olivine grains. Based on the lithological variability of the peridotites and secondary lherzolite, we interpret the pyroxenite-rich zones as the product of melt infiltration.

Two representative sections (A and B) of pyroxenite-rich zones have been investigated in detail for this study (Figs 1 and 2). Based on field, microtextural and geochemical criteria, we have grouped the Beni Bousera pyroxenites into four main types: Type-I, bright green Cr-diopside websterites; Type-II, grey–brown spinel websterites; Type-III, greyish to black garnet-bearing pyroxenites; Type-IV, greyish to green garnet metagabbros. The garnet-bearing pyroxenites were further subdivided into two subgroups: Type-IIIA, greenish to black garnet clinopyroxenites; Type-IIIB, greyish pink (garnet-) kelyphite websterites. Our new grouping of the pyroxenite types is in agreement with the previous grouping of Kornprobst *et al.* (1990), whereby our Type-IIIA and -IIIB garnet-bearing pyroxenites correspond to the Type-I pyroxenites of Kornprobst *et al.* (1990) and Type-IV garnet metagabbros correspond to Type-II of Kornprobst *et al.* (1990). In the following discussion, we first describe the field relations of the two detailed sections studied and then present petrological and geochemical data for the pyroxenites in support of our grouping scheme. A summary of the pyroxenite types, their modal compositions and thicknesses is given in Table 1 and Appendix 1.

FIELD OBSERVATIONS

Section A

Section A (Fig. 2a) is located in the Oued Mejahedid River (35°17′02.5″N, 4°53′41.5″W) and is a ~50 m long NE–SW-oriented outcrop exposing a structurally ~15 m thick package of peridotites and pyroxenites considered representative for the lithological variability observed within this large pyroxenite-rich zone (~100 m wide) in the central part of the massif. The foliation in this section generally dips gently (~15°) to the SSW. The section is dominantly composed of harzburgite, dunite and secondary lherzolite associated with numerous tens-of-centimeter thick pyroxenite bands. The pyroxenite bands consist mainly of Cr-diopside websterites (Type-I), (garnet-) kelyphite websterites (Type-IIIB) (rarely with garnet cores preserved) and to a lesser extend spinel websterites (Type-II). The Cr-diopside websterites (I) are unevenly distributed and have both sharp and diffuse contacts with the surrounding peridotite. They are generally several centimeters thick and occasionally grade into secondary lherzolite in which the amount of olivine gradually increases until the pyroxene minerals occur as interstitial phases between larger olivine grains (Fig. 3a and c). Patches of Cr-diopside and Cr-spinel several centimeters wide are also present in some secondary lherzolites (Fig. 3b) providing evidence for melt infiltration. Garnet kelyphite websterites (IIIB) form ~20 cm thick dykes that have sharp contacts with the host peridotite and are concordant with the main foliation. Locally, they exhibit tight isoclinal folds with axial planes parallel to the regional foliation (Fig. 3d). In this zone of the massif, the pyroxenites are generally garnet-free and former garnets in (garnet-) kelyphite websterites appear to have been destabilized during retrograde metamorphism (i.e. subsolidus re-equilibration in the Seiland subfacies).

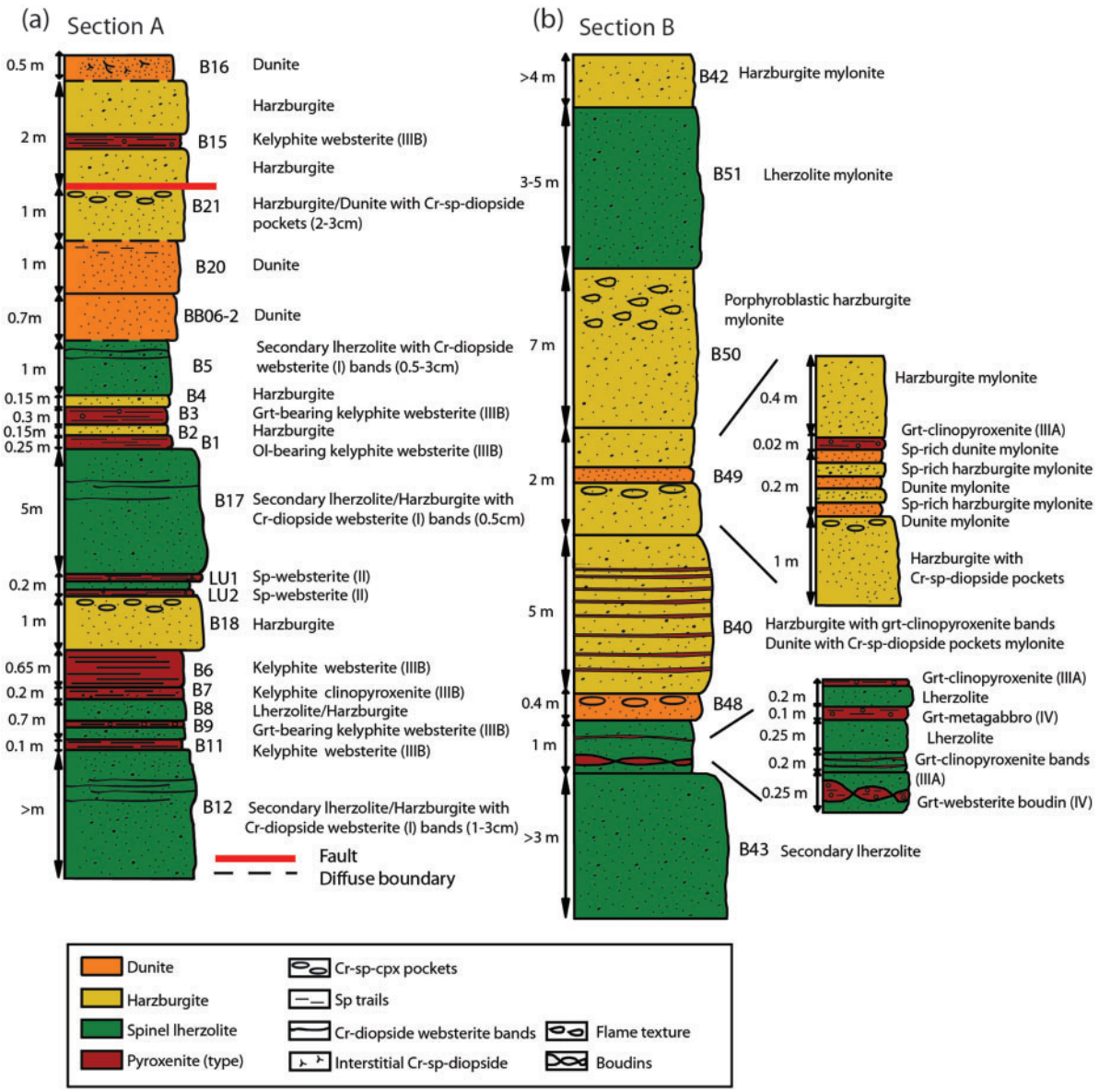

Fig. 2. The two pyroxenite-rich sections A and B in the Beni Bousera massif. (a) In section A, the spinel lherzolites are secondary lherzolites formed through infiltration of melts parental to the Cr-diopside websterites (Type-I). Pyroxenites consist of Type-I Cr-diopside websterites, Type-II spinel websterites and Type-IIIB (garnet-) kelyphite websterites. (b) In section B, pyroxenites consist mainly of variably deformed boudins and micro-boudins of Type-IIIA garnet pyroxenites and a few Type-IV garnet metagabbros.

Section B

Section B (Fig. 2b) is a NW–SE section located at the periphery of the massif in the uppermost part of the Sidi Yahia Aârab valley (35°15′05.3″N, 4°53′47.1″W) and was in part previously studied by Kornprobst *et al.* (1990). The section comprises ~25 m of peridotites and pyroxenites, and is perpendicular to the foliation, which generally dips 20° to the WSW. The section outcrop is located within a west-facing cliff in the extreme south of the Oued Mejahedid river valley. This pyroxenite-rich zone is strongly deformed with porphyroblastic textures, mylonitic rocks, boudins and micro-boudins on a meter to centimeter scale (Fig. 4). Lithological associations observed in section B are similar to those in section A except that the garnets in the pyroxenites are much less kelyphitized and that garnet pyroxenites are more abundant. Therefore, the peridotites of this section have been mapped as dominantly recording conditions of the ariegite subfacies of spinel lherzolite. The pyroxenites are mainly garnet clinopyroxenites (IIIA) forming parallel bands concordant to the foliation

Table 1: Characteristics of the four main pyroxenite types and subtypes occurring in the Beni Bousera massif

Pyroxenite type	Subtype	Color	Modal composition	Geometry	Distribution	Bulk geochemistry	Mineral geochemistry
(I) Cr-diopside websterites	Cr-diopside websterites	greenish	60–80% opx 20–40% cpx 5–10% sp <1% ol	2–5 cm bands, interstitial Cr-sp-diopside and pockets	Central parts of the massif, Seiland subfacies	primitive (high Mg-no., Ni-Cr); high LREE/HREE; neg. HFSE and pos. Pb anomalies; low Nb/Ta fract.	low CaTs, high Cr and X_{Mg} (cpx); Cr-rich magm. sp; high LREE/HREE cpx; $Th_N \geq U_N$ (low P), Nb/Ta fract. and HFSE depleted (cpx)
(II) Spinel websterites	Spinel websterites	grey	40–50% opx 5–20% cpx 5–15% sp <5–40% ol 0–1% py	3–6 cm bands	Central parts of the massif, Seiland subfacies	primitive (high Mg-no., high Ni, intermediate Cr); flat REE	high Al and Ti (cpx); magm. spinel (intermediate Cr-no. and Ti), no fract. MREE/HREE (cpx)
(III) Garnet-bearing pyroxenites (Type I Kornprobst *et al.*, 1990)	(A) Garnet clinopyroxenites	greenish grey to black-reddish	10–80% grt 2–3% kel 20–75% cpx 2–5% plag 1–5% amph 0–1% py	0·5–1·5 cm boudins, 3–5 cm bands, 5–25 cm dykes	W and SW part of the massif, ariegite subfacies	low Mg-no. and correlation with SiO_2 (magm. grt); variable FeO/MgO vs Al_2O_3; intermediate to high MREE/HREE fract. (magm. grt); Nb/Ta fract.; neg. Eu anomalies	low X_{Mg} (cpx); subcalcic augite to augite trend; Fe-Ca variations, Fe-rich grt; HREE depleted, PSD with neg. Eu anomaly and depleted LREE, Nb/Ta and Zr/Hf fract. (cpx); magm. grt HREE enriched
	(B) (Grt-) kelyphite websterites	greyish pink	1–15% grt 5–15% kel 35–85% cpx 5–50% opx 1–5% sp/plag 1–5% amph 0–1% py	2–30 cm dykes, rare isoclinal folds	W, SW and central parts of the massif, ariegite and Seiland subfacies	intermediate Mg-no.; low FeO/MgO and variable Al_2O_3; intermediate REE/HREE fract.; Nb/Ta fract.	high CaTs variations (cpx); Mg-rich (grt); HREE depleted, LREE enrichment, Nb/Ta fract. (cpx); magm. grt HREE enriched
(IV) Garnet metagabbros (Type II Kornprobst *et al.*, 1990)	(a) Grt-sp and (b) grt-plag clinopyroxenites/ websterites	grey-green	20–65% grt 5–8% kel 20–40% cpx <5–10% opx 5–8% sp/or plag	0·5–1·5 cm boudins, 0·8–10 cm bands	Section 2, ariegite subfacies	intermediate Mg-no.; high Al_2O_3, Na_2O and CaO (magm. plag.); low FeO/MgO and variable Al_2O_3, no MREE/HREE fract. (metam. grt); pos. Eu and Sr anomalies (magm. Plag); neg. HFSE; Nb/Ta fract.	high CaTs, Na and Al variations (cpx); Al-rich metam. sp; Mg-rich grt; slight fract. LREE and HREE to the MREE, pos. Eu and Sr anomaly, low HFSE (cpx); pos. Eu anomaly, low HREE (grt). metam. Grt and cpx

Graphite pseudomorph after diamond garnet clinopyroxenites (PSD) show a similar band geometry and geochemistry to specific IIIA garnet clinopyroxenites. Modal composition mineralogy consists of: grt, garnet; sp, spinel; cpx, clinopyroxene; opx, orthopyroxene; ol, olivine; plag, plagioclase; amph, amphibole; kel, kelyphite; py, pyrite. Other abbreviations: magm., magmatic; metam., metamorphic; pos., positive; neg., negative; fract., fractionation.

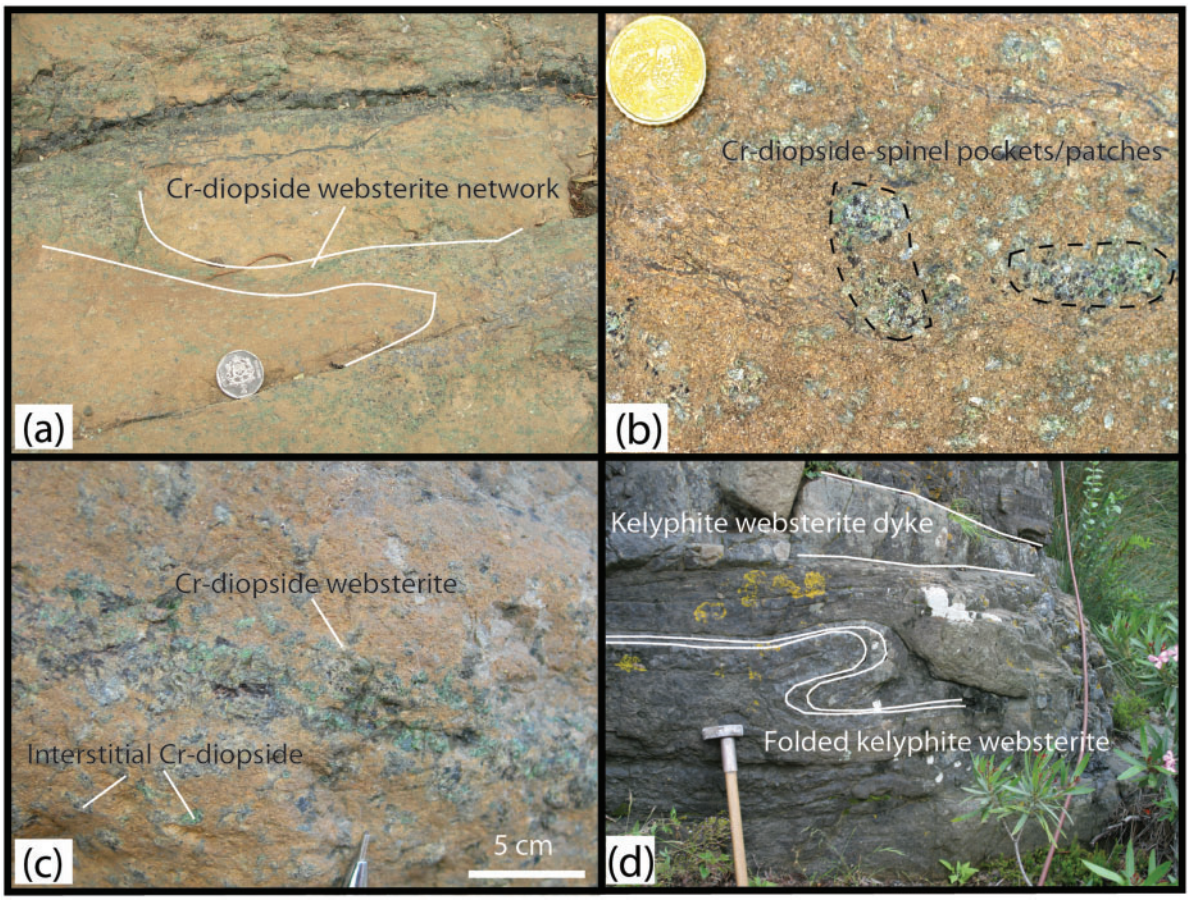

Fig. 3. Field relations showing melt infiltrations and pyroxenite bands in pyroxenite-rich zones such as in section A. (a) Cr-diopside websterites (Type-I) forming melt networks grading into secondary spinel lherzolite (north of section A). (b) Cr-diopside–spinel pockets or patches representing melt accumulations in secondary spinel lherzolite (section A). (c) Cr-diopside websterite (2–3 cm thick) and interstitial infiltrations in secondary spinel lherzolite (valley of Jenane en Nich). (d) Isoclinally folded kelyphite websterite (Type-IIIB) and less deformed 10–30 cm thick kelyphite websterite dyke (section A, direction east–west, top to SE).

(Fig. 4a) as well as a few garnet (-kelyphite) websterites (IIIB) and garnet metagabbros (IV). Cr-diopside websterite bands (I) are lacking but centimeter-scale Cr-diopside–spinel pockets of Type-I pyroxenite, similar to those from section A, are present locally in the harzburgites and dunites. Dunite and harzburgite bands occur in the middle of reaction zones intercalated within the garnet pyroxenites (Fig. 4d) and have generally higher modal Cr-spinel contents than in section A.

PETROGRAPHY, STRUCTURES AND MICROSTRUCTURES

Type-I: Cr-diopside websterites

Type-I pyroxenites are composed of dark to bright green Cr-diopside, dark brown to black Cr-spinel and brown opx porphyroclasts. They form 2–5 cm thick bands with diffuse to sharp boundaries and occur sporadically throughout the massif, but more frequently in the pyroxenite-rich zones described above (Fig. 3). In these zones, centimeter-sized pockets or patches of Cr-spinel and Cr-diopside are common in the peridotite (Fig. 3b). Based on the preserved diffuse contacts and irregular shapes, the Cr-diopside websterite bands appear macroscopically undeformed. Additionally, they sometimes form interconnected networks crosscutting the local foliation (Fig. 3a). Frequently, the Cr-diopside websterites are located in the centers of replacive dunite bands and exhibit diffuse boundaries grading from dunite into secondary lherzolite in which the pyroxenes form an interstitial honeycomb texture to larger olivine grains (Fig. 3c). Petrographic observations indicate the presence of two mineral generations (Fig. 5a). The primary magmatic mineral assemblage is composed of large brownish grey opx, green cpx porphyroclasts (1–5 mm) and associated granoblastic Cr-spinel (1–1·5 mm). Secondary minerals are

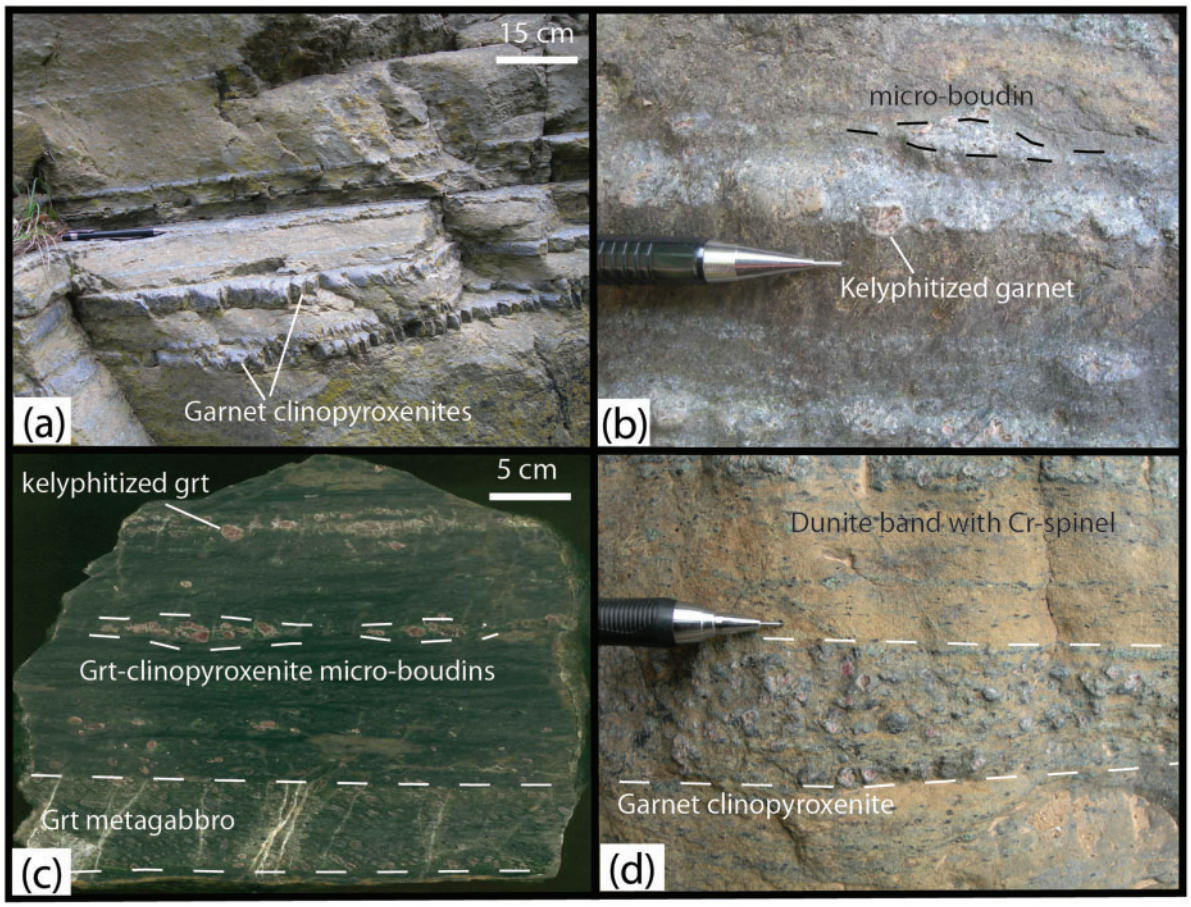

Fig. 4. Garnet pyroxenites in pyroxenite-rich zones such as section B. (a) Parallel garnet clinopyroxenite (Type-IIIA) bands concordant with the main foliation (top to west). (b, c) Garnet clinopyroxenite (Type-IIIA) and garnet metagabbro (Type-IV) bands, and deformed micro-boudins with kelyphitic rims around fragmented garnets. (d) Deformed and partially replaced garnet pyroxenite band bordering a replacive dunitic band containing Cr-spinel trails.

constituted by recrystallized anhedral cpx clusters and subgrains (CPX II) (≤0·3–0·7 mm), with holly leaf-shaped Cr-spinel trails (0·2–1 mm) and interstitial Cr-spinel (SP II) (0·1 mm). From the above field and textural observations, we interpret Type-I pyroxenites as the products of pervasive melt infiltration and metasomatic reaction with the surrounding peridotites. The mineralogical and field relations of Type-I pyroxenites are similar to the 'group D' pyroxenites in Ronda, interpreted to result from melt infiltration and associated melt–rock reaction (Garrido & Bodinier, 1999).

Type-II: spinel websterites

Type-II pyroxenites form greyish 3–6 cm thick bands with sharp boundaries to the host peridotite. In thin section contacts are gradual over several millimeters. A few Type-II pyroxenites occur in section A. They consist of primary large brown opx porphyroclasts (4–6 mm), black augitic cpx porphyroclasts (0·5–1·5 mm) and interstitial greenish hercynitic spinel (0·1–1 mm) (Fig. 5b). Secondary phases include opx clusters replacing originally polygonal cpx with interlobate boundaries (0·1–0·7 mm), and pargasitic amphibole at cpx grain boundaries (≤0·1 mm). Spinel websterites are devoid of garnet but frequently contain undeformed symplectites (0·1–0·2 mm) consisting of cpx, opx, plagioclase and amphibole. Texturally, these symplectites replace primary hercynite and secondary cpx + opx assemblages. The matrix contains variable amounts of olivine ranging from <5 to 60% in some samples grading into the peridotite, or larger primary opx porphyroclasts (4–6 mm) in an olivine matrix.

Type-III: garnet-bearing pyroxenites

Type-IIIA: garnet clinopyroxenites

Type-IIIA pyroxenites occur exclusively in the ariegite zone at the periphery of the massif (section B) either as strongly deformed 0·5–2 cm thick greenish colored micro-boudins or undeformed 3–5 cm wide grayish colored dykes and 5–25 cm wide pinkish to black dykes (Fig. 4). Larger pink–black dykes occur near the mylonitic

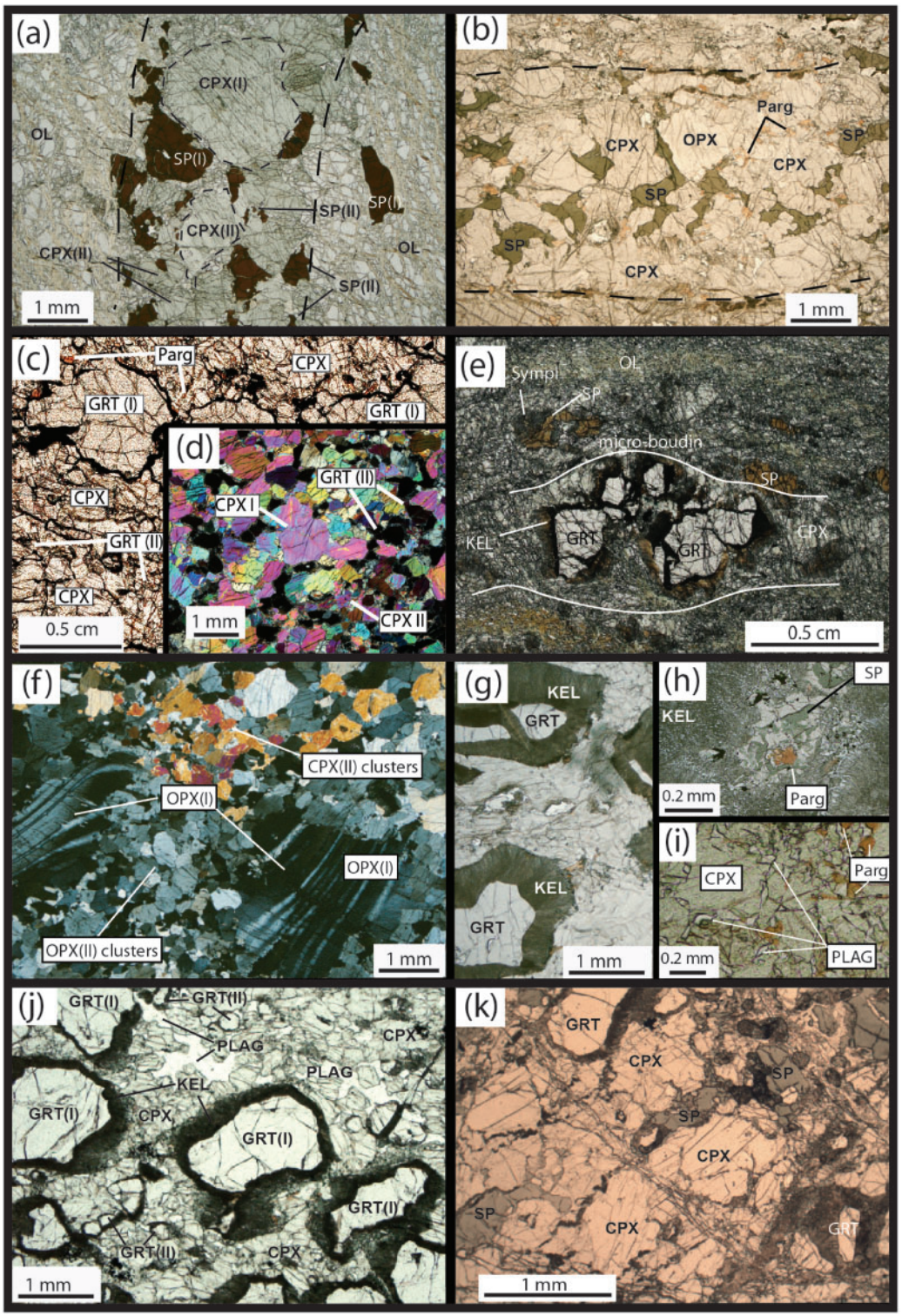

Fig. 5. Photomicrographs of the pyroxenite types. (a) Type-I Cr-diopside websterite with greenish Cr-diopside and holly leaf-shaped brown Cr-spinel, primary cpx porphyroclasts (CPX I), secondary cpx clusters (CPX II), and secondary deformed spinel (SP II). (b) Type-II spinel websterite with large pyroxene and interstitial magmatic hercynitic spinel and pargasitic amphibole (Parg). (c, d) Type-IIIA garnet clinopyroxenite with cumulate texture, primary magmatic garnet (GRT I) and cpx (CPX I), secondary interstitial garnet (GRT II) and recrystallized cpx clusters (CPX II). (e) Deformed Type-IIIA garnet clinopyroxenite micro-boudin with fragmented and kelyphitized garnet. (f) Type-IIIB (garnet-) kelyphite pyroxenite with a large deformed primary opx porphyroclast (OPX I) showing undulose extinction and recrystallized to secondary opx and cpx clusters (CPX II). (g–i) Type-IIIB pyroxenite with kelyphitized (KEL) garnet, pargasitic amphibole (Parg), plagioclase, cpx and intergrowth of hercynite (SP). (j) Type-IV garnet metagabbro with interstitial magmatic plagioclase coexisting with deformed garnet porphyroclasts (GRT I), unoriented cpx granoblasts and secondary garnet granoblasts (GRT II). (k) Type-IV pyroxenite with interstitial metamorphic spinel (hercynite), forming along cpx grain boundaries, coexisting with garnet and cpx.

western border facies of the Beni Bousera massif and are texturally and mineralogically similar to the garnet pyroxenites with graphitic diamond pseudomorphs, herein abbreviated as PSD, near the southern border of the massif (Pearson *et al.*, 1989, 1993). They form sharp boundaries with the surrounding peridotites and become more abundant in reaction zones such as in section B.

The complex history of these pyroxenites is reflected in multiple subsolidus exsolution phenomena and the presence of at least two generations of garnet and cpx. Primary coarse (1–4 mm) porphyroclastic garnets (GRT I) are frequently replaced at the rims by very fine-grained kelyphites consisting of cpx ± opx ± spinel ± plagioclase ± pargasite (Fig. 5c). The primary garnets may contain poikiloblastic inclusions of cpx and rarely also of rutile, hercynite and other oxides. Secondary garnets occur as interstitial phases or form neoblasts (<0·5 mm) between larger (~1 mm) cpx porphyroclast relicts (CPX I), which are frequently recrystallized to secondary cpx (0·3–0·6 mm) aggregates (CPX II, Fig. 5d). Primary coarse (3–5 mm) porphyroclastic subcalcic augites are only present in the PSD and exhibit up to ~50% opx exsolution lamellae, recrystallized garnet and spinel exsolution (10%) as well as some plagioclase that indicates very high formation pressures (Fig. 6a). Neoblastic garnet is frequently associated with cpx porphyroclasts, and we therefore interpret the secondary garnet in Type-IIIA pyroxenites to have formed from exsolution of cpx, similar to the recrystallized exsolution products present in the PSD. We also conclude that the primary magmatic phases in Type-IIIA pyroxenites consisted of garnet and cpx and in the PSD also of diamonds. The presence of generally small (<0·1 mm) plagioclase granoblasts along secondary garnet and cpx indicates limited late retrograde reactions of garnet and cpx at the grain surfaces. Nevertheless, some Type-IIIA pyroxenites similar to the PSD contain more abundant plagioclase along primary and secondary garnet, as well as interstitially along cpx grain boundaries (Fig. 6b). These textures are interpreted to represent retrograde reactions at higher pressures compared with other Type-IIIA pyroxenites, consistent with the absence or limited kelyphitization of those garnets 'shielded' by plagioclase.

Strongly deformed pyroxenites form micro-boudins and contain primary fragmented, rotated and partly kelyphitized garnet porphyroclasts (1–2 mm) and secondary recrystallized black and green cpx clusters and radial kelyphites (Fig. 5e). Cpx in these pyroxenites is strongly deformed and recrystallized, primary features being mainly preserved in garnet.

Type-IIIB: (garnet-) kelyphite websterites

Type-IIIB pyroxenites form grey–pink 2–30 cm thick bands parallel to the foliation in section A (Fig. 3d). Parallel bands and thin boudinaged bands (2–5 cm) alternating with Type-IIIA pyroxenites are common near the mylonitic western border facies of the Beni Bousera massif. In general, garnet is more retrogressed in section A than at the periphery of the massif. In contrast to Type-IIIA pyroxenites, Type-IIIB are, in addition to the high amount of kelyphite, characterized by primary large brown opx and black augitic cpx porphyroclasts (4–6 mm) with pyroxene exsolution lamellae recrystallized to clusters of cpx and opx neoblasts (Fig. 5f). Kelyphites consist mainly of hercynite, cpx and opx with minor pargasite and plagioclase (Fig. 5g and h). Hercynite is also preserved as 1–3 mm anhedral dark green crystals in some kelyphite websterite bands. Common deformation features in pyroxene porphyroclasts include kinkbands, bent lamellae with undulose extinction, and subgrains at grain boundaries. The plagioclase and pargasitic amphibole intergrowth in the kelyphites are interpreted as metamorphic breakdown products of garnet. Minute interstitial plagioclase and pargasite grains (≤0·1 mm) occur also along pyroxene grain boundaries (Fig. 5i) and sometimes plagioclase forms together with opx within exsolution lamellae in cpx porphyroclasts (Fig. 6c). Such microstructures are interpreted to be of metamorphic origin and indicate exsolution of cpx porphyroclasts and recrystallization along secondary cpx–opx grain boundaries (Morse, 1975). The matrix is dominated by unoriented and undeformed clusters of secondary granoblastic cpx and opx with equilibrated 120° grain junctions and/or interlobate boundaries between cpx and opx granoblasts. Based on the complicated microtextures and mineral assemblages, we interpret that the primary minerals in Type-IIIB pyroxenites consisted of garnet, cpx and opx porphyroclasts that underwent at least two major, dominantly static recrystallization events: first a recrystallization of large opx and cpx porphyroclasts to smaller undeformed neoblast clusters and second, re-equilibration of garnet at lower pressures leading to abundant kelyphite and recrystallization of plagioclase along pyroxene grain boundaries. Backscattered electron images of preserved garnet porphyroclasts (Fig. 6d) show that the garnets are unzoned and that the kelyphites are frequently associated with garnet and cpx and may result from the reaction

$$\mathrm{grt} + \mathrm{cpx} = \mathrm{opx} + \mathrm{sp} + \mathrm{plag}. \quad (1)$$

Type-IV: garnet metagabbros

Type-IV pyroxenites occur as grey–green 0·5–10 cm thick bands (Fig. 4b and c) and as meter-scale boudins in section B at the periphery of the massif. Based on the aluminous phase, two subgroups can be distinguished: Type-IVA contains relict magmatic plagioclase, whereas sub-Type-IVB has no plagioclase preserved but spinel coexisting with garnet (Fig. 5j and k). Nevertheless, all Type-IV pyroxenites have a whole-rock geochemistry indicating that they originally contained magmatic plagioclase. Type-IV

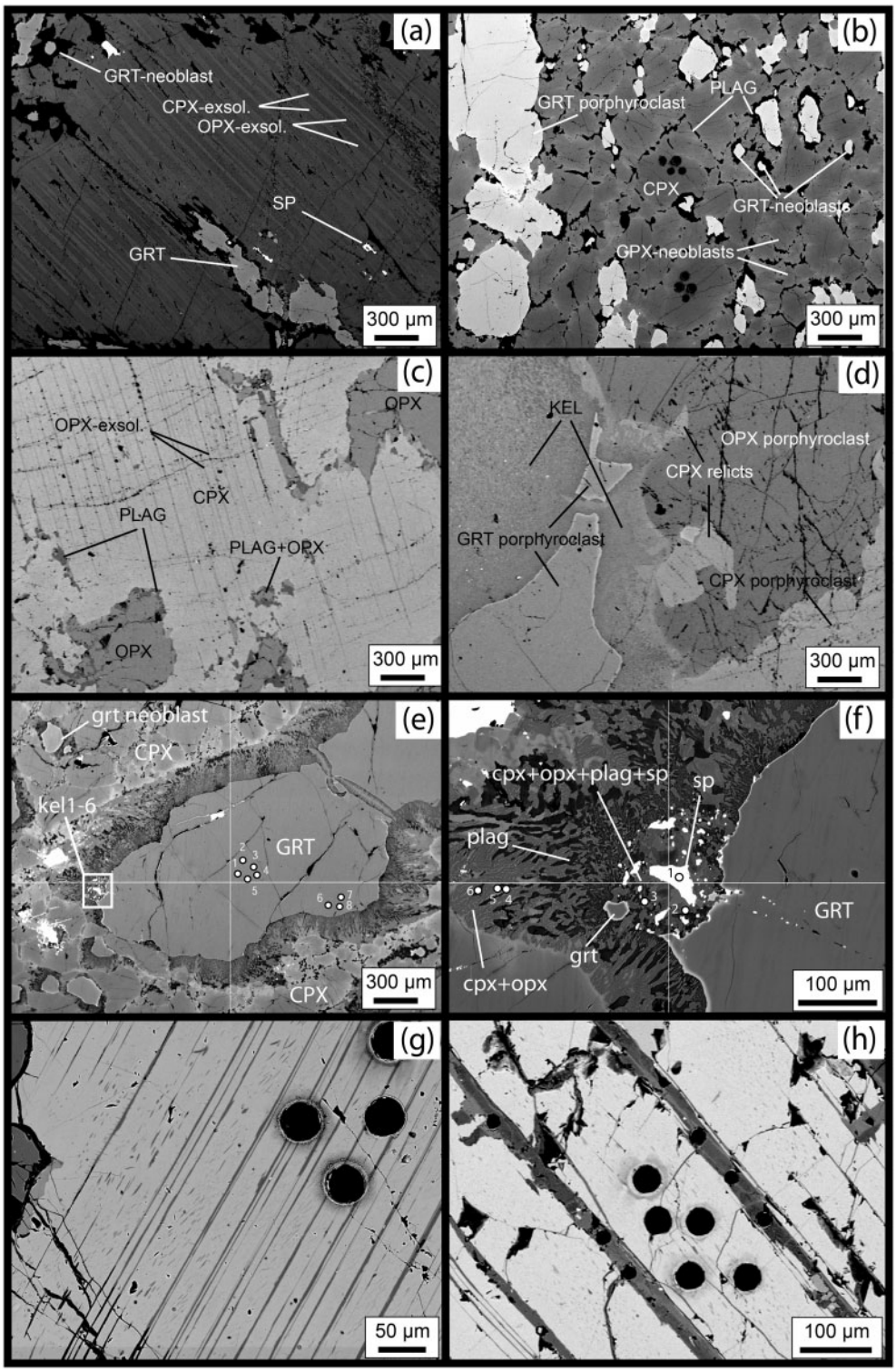

Fig. 6. Backscattered electron images showing metamorphic exsolution phenomena and retrograde reactions in the Beni Bousera pyroxenites. (a) Subcalcic augite in the PSD with exsolution lamellae of opx and cpx, and with recrystallized garnet and spinel exsolutions. (b) Type-IIIA pyroxenite with zoned augite, secondary garnet recrystallized as neoblasts along cpx triple grain boundaries, larger garnet porphyroclast trails, and plagioclase forming on the garnet and along cpx grain boundaries. (c) Cpx porphyroclast in Type-IIIB pyroxenite with secondary exsolution of plagioclase and opx recrystallized along grain boundaries. (d) Garnet in Type-IIIB pyroxenite destabilized to kelyphite by reaction with cpx. (e, f) Garnet porphyroclast, garnet neoblasts, kelyphitic rims (kel 1–6) and chemically zoned cpx porphyroclasts in Type-IV garnet–plagioclase metagabbro (numbers indicate analyses given in Electronic Appendix 7). (f) Kelyphites composed of spinel, garnet relicts, cpx, opx and plagioclase and Fe–Ti oxides. (g) Cpx from dunite with two generations of opx exsolution lamellae with variable styles. (h) Large opx exsolution lamellae in Cr-diopside from Type-I pyroxenites (trace element data for opx exsolution lamellae given in Electronic Appendix 8). LA-ICP-MS crater size (circles) in the host is 40 μm.

pyroxenites contain porphyroclastic anhedral garnet (0·5–1·5 mm) (GRT I) surrounded by deformed kelyphitic rims, green anhedral granoblastic diopside and sometimes opx (0·5 mm), small secondary anhedral granoblastic garnets (0·3–0·5 mm) (GRT II) and green interstitial hercynitic spinel (Type-IVB) or interstitial plagioclase (Type-IVA). The cpx show chemical zoning in backscattered electron images with secondary garnet neoblasts forming between cpx triple junctions (Fig. 6e). Deformed elongated kelyphites are oriented parallel to trails of deformed garnet porphyroclasts and neoblasts indicating that garnet was destabilized during deformation. Recrystallized secondary cpx and opx (0·1–0·4 mm) have sutured to interlobate grain boundaries and subgrains. The mineral chemistry of these rocks indicates a metamorphic composition for the cpx and garnet, whereas the bulk-rock chemistry indicates that plagioclase was a primary phase present in Type-IV pyroxenites.

Spinel lherzolites

Based on textural criteria, two groups of spinel lherzolites can be distinguished; primary lherzolites located mostly outside the pyroxenite-rich zones and secondary spinel lherzolites associated with the pyroxenite-rich zones. Compared with the generally porphyroclastic primary lherzolites, the secondary spinel lherzolites are characterized by honeycomb textures defined by pyroxene neoblasts forming an irregular intergranular network between larger olivine grains (Fig. 3c). They mostly occur in the vicinity of Type-I Cr-diopside websterites that have diffuse boundaries to peridotite. Distinguishing between the two groups in the field can be challenging; because we focus here on the origin of the pyroxenites, the different lherzolite types are mostly described together. A detailed differentiation of the primary and secondary lherzolites is part of our continuing work.

Harzburgites

Harzburgites are heterogeneously distributed within the spinel lherzolites and form 10 to >50 m wide zones. Their texture is porphyroclastic to porphyroblastic–granular with 5–20% opx (3–5 mm) in a fine-grained (<2 mm) olivine matrix containing 1–3% interstitial vermicular Cr-spinel (1–2 mm) and 3–5% cpx. Harzburgites are abundant within the pyroxenite-rich zones and form 10 cm to 5 m thick bands associated with composite pyroxenite bands alternating with harzburgitic and dunitic bands (Fig. 2, sections A and B). Harzburgites within the pyroxenite-rich zones contain porphyroblastic to porphyroclastic orthopyroxene (3–5 mm). Furthermore, some harzburgites have 1–5 cm Cr-diopside–spinel pockets indicating refertilization by melt infiltration accumulating in pockets or patches (Fig. 3b).

Dunites

Dunites are generally present in the pyroxenite-rich zones and occur commonly as 0·3–2 m thick bands spatially associated with harzburgites and pyroxenite bands (Fig. 2, sections A and B). In section B the dunites are more deformed with holly leaf-shaped to granoblastic Cr-spinel. In contrast, dunites from section A have equigranular mosaic textures and contain rounded Cr-spinel between triple junctions formed by olivine grain boundaries. We interpret that the dunites formed from lherzolites by pyroxene-consuming and olivine-forming reactions during melt percolation (e.g. Kelemen, 1990; Kelemen *et al.*, 1995). This is corroborated by the presence of Cr-spinel trails, by dunites spatially associated with 3–6 mm thick Cr-diopside–spinel pockets or patches and by dunites with interstitial Cr-diopside grains. Figure 4d illustrates dunitic bands with Cr-spinel trails between Type-III pyroxenite bands. These dunites are interpreted to have formed during progressive channeling of melts undergoing focused porous flow (Kelemen *et al.*, 1995).

Interpretation of field relations and microtextures–petrography

Pyroxenite-rich zones are focused in specific locations, such as in sections A and B where they form 100 m wide zones. The different characteristic lithologies and their field relations in the pyroxenite-rich zones are illustrated in a block diagram in Fig. 7. Type-I and -II pyroxenites show only limited subsolidus re-equilibration and conserve many of their primary magmatic features, whereas Type-III and -IV pyroxenites display a more pronounced metamorphic overprint. Type-III pyroxenites are concentrated at the periphery of the massif (section B) whereas Type-I pyroxenites mostly occur in the central parts of the massif (section A) associated with overprinted retrograde recrystallized garnet-bearing pyroxenites (Type-IIIB) and secondary spinel lherzolites that have been modified texturally compared with the host peridotite of the massif. In section B, Type-IV pyroxenites show strong evidence of a metamorphic overprint. Recrystallized garnet exsolution from cpx in Type-IIIA and PSD pyroxenites indicate relatively high formation pressures. Melt infiltration in pyroxenite-rich zones, largely related to the melts parental to the Cr-diopside websterites (Type-I), modify the original lherzolites considerably and result in: (1) refertilized secondary lherzolites with a honeycomb texture of Cr-diopside occurring interstitially between larger olivine grains; (2) Cr-diopside websterite bands with diffuse boundaries grading into secondary lherzolites or exhibiting a dunitic halo; (3) Cr-diopside websterite bands joining into networks; (4) Cr-diopside pockets or patches in lherzolites, harzburgites and dunites; (5) replacive dunite bands with diffuse boundaries to pyroxenite bands. These characteristics may vary between different pyroxenite-rich zones,

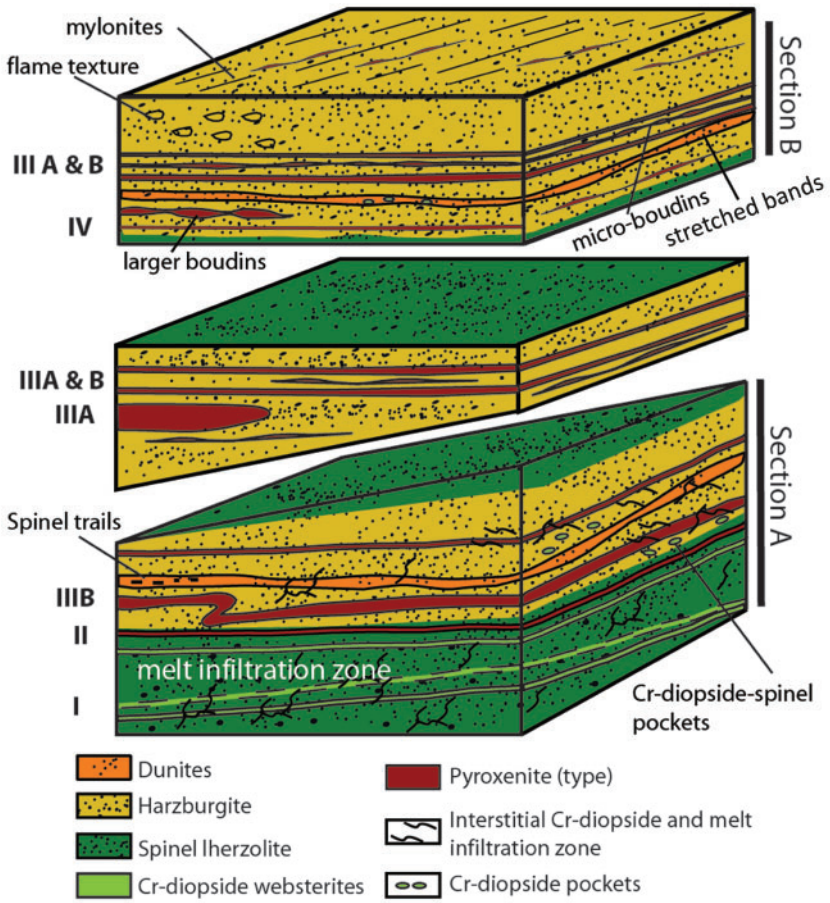

Fig. 7. Schematic block diagram illustrating the relations, structures and variety of pyroxenite types in the pyroxenite-rich zones of the Beni Bousera massif. The lower part (section A) is overprinted by pervasive melt infiltration (Type-I pyroxenites) of the lherzolites, forming secondary lherzolites. The middle part corresponds to other reaction zones encountered in the valley of Sidi Yahia Aârab with parallel, thinned or stretched Type-III garnet clinopyroxenites and websterites, and larger Type-IIIA dykes similar to the pseudomorph after diamond-bearing garnet pyroxenites (PSD). The upper strongly deformed part (section B) shows Type-III and Type-IV pyroxenites that have been stretched to boudins and micro-boudins. It should be noted that the pyroxenite bands are concordant with the main foliation but do not imply a stratigraphic layering. The interstitial Cr-diopside and melt infiltration signature is symbolic and indicates pervasive infiltration in secondary lherzolites forming diffuse networks of Type-I pyroxenites (see Fig. 3a).

which in part equilibrated at different P–T conditions, such as in sections A and B. Field and petrographic observations of both sections show direct evidence for pervasive as well as focused melt infiltration and associated wall-rock reaction.

ANALYTICAL METHODS

Bulk-rock major and trace element analysis

Sixty representative samples encompassing all pyroxenite and peridotite types have been collected and analyzed with emphasis on sections A and B (Tables 2 and 3). Whole-rock major element analyses were performed by wavelength-dispersive X-ray fluorescence (WD-XRF, Axios, PANalytical) on fused lithium tetraborate glass beads (Claisse M4 fluxer) at the Institute for Geochemistry and Petrology, ETH Zurich. Counting statistics errors are $\leq$0·1% for major elements and average detection limits are 50–100 ppm for SiO_2, MgO, Al_2O_3 and Na_2O, and 5–10 ppm for TiO_2, Fe_2O_3, MnO, CaO, K_2O and P_2O_5. Samples of Cr-diopside websterite and spinel websterite had to be cut from pyroxenite bands a few centimeters thick prior to crushing. The diffuse contacts between the Cr-diopside websterites and the surrounding peridotites make perfect separation of the two lithologies difficult. Therefore, bulk-rock analyses for these pyroxenites might contain some peridotite component. Whole-rock trace element analyses were performed by solution inductively coupled plasma mass spectromtry (ICP-MS) on a VG-PQ2 quadrupole instrument at Géosciences Montpellier (CNRS–Université de Montpellier II, France).

Sample preparation and analytical details have been described by Ionov *et al.* (1992) and Garrido *et al.* (2000). Concentrations were determined by external calibration for most elements (Merck multi-element standard solutions) except for Nb and Ta, which were calibrated by using Zr and Hf, respectively, as internal standards to avoid memory effects owing to the introduction of concentrated Nb–Ta solutions in the instrument. This technique is an adaptation of the ICP-MS analytical method described by Jochum *et al.* (1990) for the determination of Nb by spark-source mass spectrometry. The reproducibility of the method based on repeated analyses of the

Table 2: XRF bulk-rock major element analyses

Sample:	6X	9X	CP2X	CP2XX	LU1*	B15-3	LU1	F2	F6	G7	P16	P21
Type:	I	I	I	I	II	II	II	IIIA	IIIA	IIIA	IIIA	IIIA
SiO_2 (wt %)	45·28	48·56	44·98	46·61	43·15	45·23	44·14	46·73	48·12	47·58	42·68	46·27
TiO_2	0·14	0·15	0·17	0·16	0·08	0·47	0·11	0·38	0·66	0·55	0·31	0·66
Al_2O_3	6·10	6·80	5·65	4·10	1·48	7·53	2·49	14·27	12·25	12·62	17·59	12·49
FeO(tot)	7·03	6·39	6·85	6·60	9·61	10·64	9·64	9·47	9·52	11·77	15·54	10·15
MnO	0·11	0·11	0·11	0·11	0·13	0·14	0·14	0·17	0·21	0·19	0·40	0·20
MgO	32·83	30·29	33·36	32·78	43·79	27·59	41·18	14·27	18·96	15·05	12·21	15·88
CaO	5·11	5·04	5·96	7·37	1·13	6·63	1·67	13·21	9·12	10·98	10·14	13·08
Na_2O	0·37	0·39	0·35	0·54	0·02	0·77	0·08	1·21	0·95	1·41	0·55	1·11
K_2O	0·00	0·01	0·00	0·00	0·00	0·00	0·00	0·04	0·00	0·00	0·02	0·00
P_2O_5	0·01	0·01	0·01	0·01	0·01	0·03	0·01	0·03	0·02	0·02	0·01	0·01
Cr_2O_3	2·29	1·91	1·20	1·28	0·27	0·31	0·25	0·16	0·20	0·06	0·06	0·14
NiO	0·20	0·22	0·27	0·22	0·30	0·17	0·28	0·05	0·09	0·07	0·02	0·05
LOI	2·48	2·67	3·04	3·33	2·52	0·16	2·17	0·24	0·01	−0·30	−0·89	0·89
Total	99·47	99·88	98·91	99·79	99·96	99·50	99·99	99·97	100·08	100·30	99·51	100·05
FeO†	6·33	5·75	6·17	5·94	8·64	9·57	8·68	8·52	8·57	10·59	13·98	9·14
Mg-no.‡	90·24	90·37	90·60	90·77	90·03	83·71	89·43	74·91	79·78	71·69	60·87	75·59

Sample:	B44	BB91	P33	B7	B9	B1	B3	B6	B6-2	B11	B15	B45
Type:	IIIA	PSD	IIIB	IIIB	IIIB	IIIB	IIIB	IIIB	IIIB	IIIB	IIIB	IV
SiO_2 (wt %)	44·01	47·11	45·23	45·36	45·71	47·00	47·85	46·66	47·71	47·21	50·61	46·97
TiO_2	0·44	0·63	0·43	0·41	0·57	0·52	0·50	0·50	0·50	0·42	0·45	0·24
Al_2O_3	16·69	12·21	16·94	16·45	16·09	14·48	13·12	12·00	10·11	13·40	9·24	15·77
FeO(tot)	11·99	14·19	8·37	8·46	7·77	8·37	7·43	7·73	7·62	8·60	7·64	6·54
MnO	0·24	0·39	0·19	0·16	0·20	0·18	0·17	0·17	0·15	0·17	0·15	0·11
MgO	12·47	15·27	18·63	15·11	18·28	18·98	19·41	18·51	19·27	19·00	22·08	14·91
CaO	12·91	8·96	9·16	12·24	10·87	9·64	10·17	12·99	13·47	9·89	8·64	13·06
Na_2O	0·92	1·27	0·68	1·36	0·66	1·03	1·09	0·85	0·91	1·26	1·00	1·65
K_2O	0·00	0·00	0·01	0·01	0·01	0·01	0·00	0·01	0·00	0·01	0·00	0·01
P_2O_5	0·03	0·02	0·04	0·02	0·03	0·02	0·02	0·02	0·02	0·03	0·01	0·01
Cr_2O_3	0·07	0·12	0·15	0·12	0·15	0·18	0·18	0·24	0·28	0·23	0·21	0·16
NiO	0·03	0·01	0·04	0·05	0·06	0·07	0·09	0·11	0·10	0·08	0·10	0·06
LOI	−0·47	−0·30	0·18	0·25	0·06	0·02	0·21	0·19	0·32	0·25	0·14	0·18
Total	99·78	100·18	99·87	99·75	100·39	100·49	100·04	99·76	100·13	100·28	100·11	99·50
FeO†	10·79	12·77	7·53	7·61	7·00	7·53	6·69	6·96	6·86	7·74	6·87	5·89
Mg-no.‡	67·32	68·07	81·51	77·96	82·32	81·79	83·80	82·58	83·36	81·40	85·13	81·87

(continued)

Table 2: Continued

Sample:	B46-3	P1	P2	F3	F4	LZP	LZP*	LZP3	LZP4	STO1	G5	B51
Rock type:	IV	Grt Lz	Grt Lz	Grt Lz	Grt Lz	Sp Lz	Sp Lz	Sp Lz	Sp Lz	Sp Lz	Sp Lz	Sp Lz
SiO_2 (wt %)	45·82	44·77	44·31	45·61	44·04	44·68	44·29	43·83	44·22	44·25	44·63	44·31
TiO_2	0·20	0·16	0·07	0·22	0·18	0·16	0·15	0·08	0·10	0·14	0·11	0·11
Al_2O_3	16·38	3·50	2·73	4·85	4·26	3·72	3·56	2·25	3·03	3·73	3·40	2·95
FeO(tot)	6·10	9·05	8·76	9·10	9·23	8·99	9·09	8·99	8·78	9·10	8·97	8·92
MnO	0·11	0·13	0·13	0·14	0·14	0·13	0·13	0·13	0·13	0·14	0·13	0·13
MgO	16·04	38·61	41·27	35·23	37·18	38·24	38·86	42·23	40·04	38·94	38·58	40·33
CaO	13·01	3·25	2·19	4·03	3·69	3·45	3·34	1·84	2·76	3·04	3·06	2·47
Na_2O	1·69	0·27	0·09	0·37	0·29	0·26	0·26	0·09	0·15	0·20	0·19	0·19
K_2O	0·00	0·00	0·00	0·00	0·00	0·00	0·00	0·00	0·00	0·00	0·00	0·00
P_2O_5	0·01	0·02	0·01	0·02	0·02	0·01	0·02	0·01	0·01	0·01	0·01	0·01
Cr_2O_3	0·27	0·37	0·40	0·33	0·37	0·38	0·37	0·34	0·35	0·37	0·37	0·37
NiO	0·07	0·26	0·28	0·24	0·25	0·27	0·27	0·28	0·28	0·26	0·26	0·28
LOI	0·81	5·59	6·26	4·74	6·05	1·59	3·03	4·11	4·78	4·14	3·62	2·86
Total	99·70	100·38	100·25	100·13	99·63	100·29	100·34	100·06	99·85	100·19	99·71	100·09
FeO†	5·49	8·14	7·88	8·19	8·30	8·09	8·18	8·09	7·90	8·18	8·07	8·03
Mg-no.‡	83·89	89·42	90·33	88·46	88·87	89·39	89·44	90·29	90·03	89·45	89·50	89·95
X_{Mg} olivine	–	–	–	–	–	–	–	–	0·897	–	–	–
NiO olivine	–	–	–	–	–	–	–	–	0·394	–	–	–

Sample:	P22	LZP2	P8	B17-2	BI7*	B5	B43	B43*	J10	J11	B18	B52
Rock type:	Sp Lz	Sp Lz	Sp Lz	Sp Lz	Sp Lz	Sp Lz	Sp Lz	Sp Lz	Sp Lz	Sp Lz	Sp Lz	Sp Lz
SiO_2 (wt %)	44·84	43·85	44·14	44·00	44·05	46·90	43·76	44·03	44·47	44·19	44·47	44·38
TiO_2	0·11	0·06	0·06	0·09	0·09	0·27	0·06	0·06	0·05	0·06	0·05	0·06
Al_2O_3	3·66	2·56	2·72	1·68	1·74	4·72	2·15	2·22	2·55	2·74	2·57	2·50
FeO(tot)	8·85	8·74	8·61	8·68	8·62	8·31	8·69	8·69	8·55	8·47	8·64	8·71
MnO	0·13	0·13	0·13	0·12	0·12	0·12	0·13	0·13	0·13	0·13	0·13	0·13
MgO	38·29	42·35	41·02	43·16	42·80	34·43	42·40	42·44	41·42	41·33	41·40	41·37
CaO	3·19	2·12	2·32	1·65	1·86	3·88	1·83	1·86	2·41	2·41	2·36	2·27
Na_2O	0·21	0·12	0·11	0·11	0·11	0·40	0·11	0·07	0·12	0·11	0·12	0·11
K_2O	0·00	0·00	0·00	0·00	0·00	0·00	0·00	0·00	0·00	0·00	0·00	0·00
P_2O_5	0·01	0·01	0·01	0·01	0·01	0·02	0·01	0·01	0·01	0·01	0·01	0·01
Cr_2O_3	0·38	0·43	0·40	0·41	0·43	0·74	0·39	0·40	0·45	0·43	0·39	0·38
NiO	0·26	0·29	0·28	0·30	0·30	0·22	0·29	0·29	0·28	0·28	0·28	0·28
LOI	0·72	5·09	4·36	2·88	2·78	1·62	3·34	3·29	7·96	6·40	2·68	2·89
Total	99·93	100·65	99·80	100·21	100·13	100·00	99·80	100·19	100·43	100·14	100·43	100·19
FeO†	7·96	7·86	7·75	7·81	7·76	7·48	7·82	7·82	7·69	7·62	7·78	7·84
Mg-no.‡	89·55	90·56	90·41	90·78	90·77	89·14	90·63	90·63	90·56	90·63	90·46	90·39
X_{Mg} olivine	–	0·898	–	–	0·884	–	–	–	–	–	–	–
NiO olivine	–	0·385	–	–	0·383	–	–	–	–	–	–	–

(continued)

Table 2: Continued

Sample:	B52*	B2	B4	B18-3	B42	B42*	B50	B42*	B50	B49	B21
Rock type:	Sp Lz	Hz	Hz	Hz	Hz	Hz	Hz	Hz	Hz	Hz	Dunite
SiO_2 (wt %)	44·33	44·38	46·10	43·68	44·21	42·63	44·11	42·63	44·11	42·74	43·02
TiO_2	0·06	0·16	0·30	0·01	0·12	0·01	0·01	0·01	0·01	0·02	0·05
Al_2O_3	2·48	2·38	5·32	0·75	3·23	0·75	0·92	0·75	0·92	0·71	0·77
FeO(tot)	8·61	12·21	9·37	8·50	8·79	8·71	8·74	8·71	8·74	8·87	9·23
MnO	0·13	0·13	0·13	0·12	0·13	0·12	0·13	0·12	0·13	0·13	0·12
MgO	41·66	38·86	33·44	45·87	39·80	46·15	45·27	46·15	45·27	46·48	46·25
CaO	2·16	1·63	4·58	0·61	2·76	0·64	0·88	0·64	0·88	0·65	0·53
Na_2O	0·08	0·16	0·48	0·00	0·19	0·00	0·00	0·00	0·00	0·00	0·00
K_2O	0·00	0·00	0·00	0·00	0·00	0·00	0·00	0·00	0·00	0·00	0·00
P_2O_5	0·01	0·02	0·02	0·01	0·01	0·01	0·01	0·01	0·01	0·01	0·01
Cr_2O_3	0·39	0·25	0·43	0·32	0·38	0·37	0·40	0·37	0·40	0·34	0·29
NiO	0·29	0·27	0·23	0·31	0·27	0·33	0·31	0·33	0·31	0·33	0·34
LOI	2·84	2·09	1·23	3·67	2·33	4·29	4·30	4·29	4·30	5·73	1·58
Total	100·18	100·45	100·38	100·18	99·88	99·71	100·77	99·71	100·77	100·27	100·62
FeO†	7·75	10·99	8·43	7·65	7·91	7·83	7·87	7·83	7·87	7·98	8·31
Mg-no.‡	90·55	86·31	87·60	91·44	89·97	91·30	91·12	91·30	91·12	91·21	90·84
X_{Mg} olivine	–	–	–	–	–	–	–	–	–	–	0·904
NiO olivine	–	–	–	–	–	–	–	–	–	–	0·409

Sample:	BB06-2	B16	B20	9H
Rock type:	Dunite	Dunite	Dunite	Dunite
SiO_2 (wt %)	39·92	42·61	42·56	43·31
TiO_2	0·02	0·01	0·04	0·03
Al_2O_3	0·48	0·46	0·71	0·67
FeO(tot)	10·54	8·83	9·23	8·76
MnO	0·13	0·12	0·13	0·12
MgO	48·28	47·05	46·26	45·62
CaO	0·12	0·43	0·53	0·49
Na_2O	0·00	0·00	0·00	0·00
K_2O	0·00	0·00	0·00	0·00
P_2O_5	0·02	0·01	0·02	0·01
Cr_2O_3	0·40	0·37	0·27	0·38
NiO	0·40	0·32	0·35	0·31
LOI	5·18	4·76	4·59	2·43
Total	100·32	100·20	100·10	99·71
FeO†	9·49	7·94	8·31	7·88
Mg-no.‡	90·07	91·35	90·85	91·16
X_{Mg} olivine	–	–	–	–
NiO olivine	–	–	–	–

Pyroxenite types: I, Cr-diopside websterites; II, spinel websterites; IIIA, garnet clinopyroxenites; IIIB, kelyphite websterites; IV, garnet metagabbros; PSD, graphite pseudomorph after diamond. Peridotites: Grt Lz, pseudo-grt lherzolites; Sp Lz, spinel lherzolites; Hz, harzburgites; dunites. LOI, loss on ignition.
[1]FeO (wt %) calculated from Fe total.
[2]In mol %.

Table 3: Solution-ICP-MS bulk-rock trace element concentrations (ppm) of Beni Bousera ultramafic rocks

Sample:	6X	9X	CP2X	CP2XX	B15-3	LU1	F2	F6	G7	P16	P21
Type:	I	I	I	I	II	II	IIIA	IIIA	IIIA	IIIA	IIIA
Cs	0·057	0·135	0·072	0·065	0·060	0·022	0·683	0·133	0·159	0·330	0·073
Rb	0·293	0·565	0·301	0·287	0·389	0·095	2·226	0·277	0·991	2·007	0·308
Ba	1·378	3·410	0·697	1·331	0·448	0·320	3·580	2·307	0·721	4·406	2·234
Th	0·045	0·045	0·021	0·051	0·009	0·007	0·105	0·024	0·009	0·008	0·013
U	0·009	0·008	0·005	0·011	0·003	0·002	0·033	0·007	0·004	0·005	0·005
K	52·003	119·209	53·017	53·017	43·631	19·210	402·140	70·792	55·815	191·288	68·558
Nb	0·075	0·099	0·087	0·112	0·044	0·030	0·057	0·202	0·029	0·015	0·079
Ta	0·012	0·014	0·010	0·017	0·010	0·005	0·027	0·049	0·007	0·017	0·012
La	0·648	0·765	0·376	0·857	0·407	0·109	0·306	0·451	0·097	0·022	0·258
Ce	2·248	2·205	1·384	2·802	1·651	0·387	1·097	1·794	0·604	0·077	1·102
Pb	0·186	1·351	0·234	0·456	0·190	0·102	1·867	0·186	0·092	0·102	0·199
Pr	0·388	0·372	0·267	0·503	0·352	0·063	0·212	0·387	0·157	0·017	0·259
Sr	37·647	34·836	45·481	54·586	22·183	6·091	57·484	46·149	28·582	3·481	39·647
Nd	2·187	2·101	1·611	2·956	2·301	0·351	1·483	3·041	1·238	0·151	1·958
Hf	0·290	0·296	0·275	0·391	0·677	0·098	0·305	1·610	0·311	0·158	0·434
Zr	10·372	11·086	11·409	14·311	25·801	3·639	10·875	73·121	12·018	5·051	12·411
Ti	706·3	769·8	877·4	877·4	2564·0	559·0	2028·3	3520·2	3006·3	1602·6	3553·4
Sm	0·630	0·615	0·548	0·877	0·944	0·120	0·669	1·730	0·555	0·257	1·105
Eu	0·233	0·234	0·227	0·327	0·382	0·051	0·316	0·777	0·232	0·114	0·520
Gd	0·742	0·750	0·825	1·031	1·631	0·203	1·102	3·385	1·008	2·017	2·379
Tb	0·115	0·118	0·149	0·162	0·296	0·040	0·207	0·676	0·219	0·714	0·462
Dy	0·729	0·747	0·995	1·026	2·008	0·289	1·553	5·025	1·848	7·368	3·158
Ho	0·136	0·143	0·185	0·193	0·383	0·058	0·339	1·075	0·444	1·921	0·585
Y	3·277	3·444	5·182	4·736	10·726	1·619	9·049	30·760	13·229	61·393	17·800
Er	0·347	0·371	0·511	0·491	1·076	0·171	0·989	3·083	1·546	6·920	1·631
Tm	0·045	0·050	0·074	0·063	0·160	0·028	0·145	0·447	0·270	1·253	0·246
Yb	0·272	0·309	0·449	0·379	0·988	0·182	0·953	2·902	1·876	8·834	1·497
Lu	0·043	0·050	0·066	0·059	0·151	0·029	0·161	0·479	0·310	1·462	0·217
Nb_N/La_N	0·110	0·123	0·220	0·124	0·102	0·262	0·177	0·423	0·288	0·631	0·289
Gd_N/Yb_N	2·212	1·967	1·489	2·206	1·338	0·905	0·937	0·945	0·435	0·185	1·288

Sample:	B44	BB91	P33	B7	B1	B3	B6	B9	B11	B15	B45
Type:	IIIA	PSD	IIIB	IIIB	IIIB	IIIB	IIIB	IIIB	IIIB	IIIB	IV
Cs	0·068	0·360	0·105	0·129	0·148	0·190	0·124	0·094	0·120	0·178	0·357
Rb	0·507	0·479	0·578	1·169	1·088	1·005	0·545	0·810	1·142	0·808	2·688
Ba	0·507	0·513	6·775	0·937	1·570	4·479	2·606	1·581	1·549	0·634	6·517
Th	0·032	0·009	0·035	0·013	0·024	0·025	0·024	0·020	0·013	0·016	0·011
U	0·014	0·004	0·016	0·004	0·005	0·005	0·006	0·007	0·004	0·003	0·004
K	69·361	16·603*	104·024	135·445	113·080	72·165	96·964	108·530	41·390*	46·821	114·160
Nb	0·200	0·026	0·334	0·063	0·056	0·032	0·183	0·218	0·071	0·023	0·010
Ta	0·023	0·010	0·031	0·012	0·076	0·013	0·022	0·022	0·016	0·006	0·005
La	0·284	0·025	0·751	0·285	0·629	0·749	0·545	0·342	0·386	1·014	0·180
Ce	1·030	0·075	2·965	1·141	2·615	3·157	1·903	1·395	1·589	2·737	0·794
Pb	0·318	0·195	0·159	0·190	0·254	0·481	0·184	0·131	0·329	0·371	0·205
Pr	0·198	0·020	0·530	0·212	0·499	0·594	0·359	0·284	0·327	0·498	0·177
Sr	20·133	4·685	91·871	31·331	37·850	42·836	47·861	40·001	38·757	32·282	111·295
Nd	1·407	0·206	3·159	1·326	3·118	3·472	2·346	1·909	2·269	2·700	1·267
Hf	0·438	0·386	0·748	0·418	0·826	0·704	0·446	0·621	0·515	0·484	0·251
Zr	18·746	7·119	42·822	16·608	41·132	30·124	16·881	30·419	20·738	16·450	7·849
Ti	2283·8	3751·9*	2289·7	2202·2	2890·9	2813·6	2662·5	3192·3	2528·1*	2475·0	1256·5
Sm	0·819	0·248	1·178	0·645	1·166	1·136	1·036	1·054	0·957	0·810	0·525
Eu	0·342	0·140	0·520	0·339	0·508	0·436	0·440	0·528	0·418	0·299	0·297
Gd	2·044	1·391	1·976	1·465	1·906	1·831	1·718	2·607	1·557	1·144	0·856
Tb	0·473	0·428	0·365	0·303	0·353	0·375	0·346	0·564	0·280	0·201	0·169
Dy	3·964	4·071	2·470	2·117	2·562	2·907	2·654	4·223	1·901	1·318	1·226
Ho	0·918	1·003	0·465	0·416	0·551	0·569	0·569	0·868	0·360	0·240	0·233
Y	29·741	30·826	13·191	12·186	15·840	17·464	17·116	27·756	10·452	7·102	6·917
Er	3·047	3·486	1·288	1·222	1·590	1·626	1·577	2·668	0·995	0·670	0·616
Tm	0·500	0·610	0·189	0·185	0·229	0·264	0·230	0·435	0·147	0·102	0·090
Yb	3·311	4·152	1·189	1·134	1·484	1·843	1·502	2·847	0·924	0·657	0·580
Lu	0·534	0·667	0·177	0·167	0·249	0·313	0·243	0·443	0·139	0·100	0·092
Nb_N/La_N	0·665	0·959	0·421	0·210	0·084	0·041	0·317	0·604	0·174	0·022	0·050
Gd_N/Yb_N	0·500	0·272	1·347	1·047	1·041	0·805	0·927	0·742	1·366	1·411	1·197

(continued)

Table 3: Continued

Sample:	B46-3	LZP3	LZP4	LZP2	B17	B5
Type:	IV	Sp Lz	Sp Lz	Sp Lz	Sp Lz	Sp Lz
Cs	0·267	0·000	0·007	0·014	0·046	0·164
Rb	0·701	0·041	0·069	0·095	0·150	0·627
Ba	4·864	0·168	0·095	0·275	0·347	0·588
Th	0·007	0·005	0·003	0·010	0·008	0·021
U	0·004	0·002	0·002	0·004	0·002	0·004
K	54·122	12·630	25·457	18·754	0·000*	39·637
Nb	0·029	0·023	0·023	0·066	0·044	0·034
Ta	0·032	0·011	0·017	0·013	0·036	0·019
La	0·245	0·074	0·101	0·607	0·171	0·491
Ce	0·814	0·245	0·364	0·248	0·709	1·805
Pb	0·140	0·064	0·076	0·084	0·115	0·201
Pr	0·166	0·045	0·071	0·046	0·138	0·300
Sr	258·220	5·384	8·114	5·301	14·167	19·039
Nd	1·151	0·288	0·468	0·309	0·856	1·693
Hf	0·253	0·081	0·115	0·075	0·127	0·444
Zr	7·570	2·882	4·415	3·044	5·823	17·172
Ti	1084·6	386·1	508·0	325·9	514·4*	1477·8
Sm	0·481	0·120	0·186	0·122	0·250	0·549
Eu	0·316	0·053	0·081	0·052	0·091	0·217
Gd	0·783	0·210	0·316	0·199	0·291	0·798
Tb	0·142	0·041	0·062	0·039	0·047	0·142
Dy	1·013	0·310	0·470	0·300	0·312	0·998
Ho	0·211	0·068	0·104	0·068	0·062	0·206
Y	5·432	1·884	2·573	1·888	1·657	5·411
Er	0·583	0·205	0·309	0·206	0·167	0·574
Tm	0·081	0·031	0·046	0·031	0·023	0·081
Yb	0·509	0·211	0·309	0·214	0·148	0·513
Lu	0·083	0·036	0·053	0·037	0·024	0·084
Nb_N/La_N	0·112	0·293	0·216	0·103	0·241	0·066
Gd_N/Yb_N	1·248	0·807	0·831	0·757	1·597	1·261

K and Ti from LA-ICP-MS measurement (except where otherwise noted). Pyroxenite types are the same as in Table 2. *K and Ti from XRF measurements.

international standards PCC-1 and UB-N (Garrido *et al.*, 2000; Godard *et al.*, 2008) was generally better than 5% for most elements (>50 ppb) and 10–20% for Nb, Ta, Hf, U and Th (<50 ppb). Detection limits were <2 ppb for Cs, Rb, Ba, Pb, Zr, Sr and Y; <1 ppb for La, Ce, Pr, Nd, Sm, Eu, Gd, Tb, Dy, Ho, Er, Tm, Yb and Lu; and <0·5 ppb for Th, U, Nb, Ta and Hf. K and Ti were measured by laser ablation (LA)-ICP-MS (at the Institute for Geochemistry and Petrology, ETH Zurich) on the fused lithium tetraborate glass beads used for XRF analyses. The glass beads were broken and the homogeneous internal parts analyzed. The laser-ablation system used is a GEOLAS 193 nm Ar–F excimer laser, combined with a Perkin Elmer Elan 6100 DRC ICP-MS system. The spot size was 60 μm and a 15 Hz repetition rate was used. Concentrations were calculated following Longerich *et al.* (1996) and counts converted to concentrations using NIST 610 as an external standard and CaO measurements from XRF analysis as an internal standard. Mean run detection limits were 1·8 ppm for K and 4·5 ppm for Ti. For each sample three spot analyses were averaged.

Mineral major and trace element analysis

Mineral major elements were analyzed on 60–100 μm thick polished thin sections using a JEOL JXA-8200 electron

microprobe at ETH Zurich, using a beam current of 20 nA, a beam diameter of 1–4 μm and 15·0 kV acceleration voltage. Standards consist of natural (wollastonite, Ca and Si; aegirine, Na; K-feldspar, K; chromite, Cr) and synthetic (fayalite, Fe; corundum, Al; periclase, Mg; bunsenite, Ni; pyrolusite, Mn; rutile, Ti) minerals. Counting times were 40 s for Si, Al, K, Na, Ca, Mg, Ti, Cr and Ni, and 20 s for Mn and Fe. Average major element compositions measured on 3–30 spots in the core of each mineral are reported with their analytical precision (2σ) in Tables 4–7. Mineral heterogeneity is mainly observed in pyroxenes owing to subsolidus exsolution. A full set of mineral analyses with core compositions, core–rim profiles, mineral neoblasts and kelyphite compositions is given in Electronic Appendices 1–7 (available for downloading at http://www.petrology.oxfordjournals.org).

Mineral trace elements were measured by LA-ICP-MS (as above). Nineteen polished thin sections were analyzed focusing on garnet and cpx. Concentrations were calculated as described by Longerich *et al.* (1996) and counts were converted to concentrations using NIST 610 as an external standard. CaO and Al_2O_3 were used as internal standards from electron microprobe analysis (EMPA) of cpx and garnet respectively. All data were processed and spikes eliminated using the SILLS software (version 1.0.5) from Guillong *et al.* (2008). Each mineral was analyzed on 3–6 spots of 40 μm diameter using 15 Hz repetition rates. Limits of detection (LOD) are calculated from background standard deviations following Longerich *et al.* (1996) and using the SILLS software. Average LODs (3σ) and limits of quantification (LOQ), defined here as 10σ of the background (McNeill *et al.*, 2009), are given in Appendix 4. Average analytical precision (1σ % RSD) based on 42 cpx and repeated spot analysis in mineral cores was 3–10% for Ti, Sr, Y, Zr, La, Ce and Pr; 10–15% for Nb, Nd, Sm Eu, Gd, Tb, Dy, Ho, Er, Lu, Hf, Ta and U; and 15–25% for Ba, Tm, Yb, Th and Pb. Average analytical precision based on 43 garnet analyses was 4–10% for Ti, Y, Tb, Dy, Ho, Er and Tm; and 10–20% for Ce, Nd, Nd, Sm, Eu, Gd, Yb, Lu and Hf; whereas Nb, Ba, La, Ta, Pb, Th and U are below the detection limit in garnet. Average values and their 2σ errors from analyses of 2–6 cpx and garnet cores per thin sections are given in Tables 8 and 9.

LA-ICP-MS: analytical difficulties arising from subsolidus exsolution in cpx

Depending on the pyroxenite type, clino- and orthopyroxenes show variations in the size and amount of exsolution lamellae. Consequently, laser ablation craters were located on backscattered electron images to evaluate the representativeness of the analyzed cpx and their opx exsolution lamellae. In most cases, the exsolution lamellae are thin and heterogeneous; average laser craters include both lamellae and host mineral (Fig. 6g). Major element concentrations used as internal standards for trace element concentration calculations were corrected for the amount of lamellae if the lamellae size was large enough to measure by EMPA: (1) where exsolution lamellae were small we used a defocused beam (~20 μm) to reintegrate the exsolution lamellae; (2) where the exsolution lamellae were too wide we used the average of a line scan across the pyroxene employing a 20 μm defocused beam and a step size of 10 μm, thereby reintegrating a 100–300 μm × 20 μm area; (3) alternatively, exsolution lamellae and host were measured separately and reintegrated using backscattered electron images for relative surface area estimates. Reconstructed compositions of cpx and opx are given in Tables 4 and 5, together with the original host pyroxene core compositions and their exsolution lamellae when measurable. Major element concentration changes of integrated cpx and opx compared with the uncorrected values amount to 1–3 wt % CaO and/or MgO except for the subcalcic augites (PSD sample) for which the correction amounts to 3–8 wt %.

BULK-ROCK GEOCHEMISTRY

A list of all the analysed samples with details including modal compositions, global positioning system (GPS) locations and rock types are given in Appendix 1. The bulk-rock major and trace element data for the studied samples are provided as Supplementary Data (http://www.petrology.oxfordjournals.org/).

Bulk-rock major elements and transition metals

Bulk-rock major element compositions (Fig. 8) correlate roughly with observed mineral modes reflecting the cumulative nature of most pyroxenites. Nevertheless, trends are observed between the different pyroxenites and peridotites in plots of major elements vs Mg-number. The latter ranges from 60·9 to 91·4, and Type-I and Type-II pyroxenites have the highest values of all pyroxenites. High Mg-number indicates a more primitive character of the parental melt compared with other pyroxenites and/or re-equilibration with the host peridotite. This primitive character is also reflected in high Cr and Ni contents, both of which are positively correlated with Mg-number.

Type-I pyroxenites have nearly constant Mg-number and variably high Cr_2O_3, TiO_2, Na_2O, Al_2O_3, CaO and SiO_2 compared with peridotites in which TiO_2, Na_2O, Al_2O_3, CaO and SiO_2 correlate negatively with Mg-number. This corresponds well to the mineral chemistry; that is, Cr-diopsides from Type-I pyroxenites have variable Na but nearly constant Mg-number. Comparison of the bulk-rock chemistry of peridotites and Type-I Cr-diopside websterites indicates that the relatively constant Mg-number is buffered by the host-rock peridotites, whereas the variations of TiO_2, Na_2O, Al_2O_3, CaO and

Table 4: Selected average EMPA cpx major elements representative for each pyroxenite and peridotite sample

Sample:	6[1] host	6[1] e.l.	CP2[1] host	CP2[1] e.l.	B15-3[2] host	B15-3[2] e.l.	BB91[3] host	BB91[3] e.l.
Type:	I	I	I	I	II	II	PSD	PSD
No.:	15	3	5	5	5	5	4	4
SiO_2	52·6 (5)	54·6 (17)	51·9 (6)	54·3 (1)	49·3 (3)	51·8 (6)	51·5 (2)	52·7 (1)
TiO_2	0·32 (6)	0·10 (16)	0·33 (5)	0·06 (1)	1·10 (7)	0·17 (3)	1·24 (5)	0·28 (3)
Cr_2O_3	1·85 (14)	1·06 (53)	1·86 (11)	0·89 (4)	0·59 (2)	0·33 (4)	0·24 (8)	0·09 (4)
Al_2O_3	5·90 (22)	4·22 (142)	6·01 (20)	4·07 (16)	9·41 (26)	6·54 (18)	8·48 (34)	4·40 (33)
FeO	2·73 (36)	5·93 (138)	2·64 (17)	6·39 (20)	3·99 (37)	10·77 (49)	6·58 (118)	17·14 (17)
MnO	0·09 (3)	0·15 (1)	0·10 (4)	0·15 (3)	0·11 (3)	0·21 (3)	0·24 (2)	0·36 (2)
NiO	0·04 (3)	0·08 (7)	0·04 (5)	0·12 (2)	0·04 (2)	0·09 (3)	0·01 (3)	0·02 (3)
MgO	15·4 (13)	30·4 (76)	14·3 (3)	33·4 (7)	12·6 (9)	29·1 (5)	12·2 (11)	25·2 (4)
CaO	20·6 (15)	4·02 (81)	20·9 (5)	0·52 (5)	19·6 (9)	0·51 (8)	18·3 (17)	0·58 (1)
Na_2O	1·83 (17)	0·38 (74)	1·97 (12)	0·03 (3)	2·29 (29)	0·06 (2)	2·42 (23)	0·02 (1)
Total	101·4	101·0	100·1	99·9	99·2	99·6	101·2	100·7
X_{Mg}	0·909	0·901	0·906	0·903	0·850	0·828	0·768	0·723

Sample:	B9[4] host	B9[4] e.l.	LZP4[5] host	LZP4[5] e.l.	B17-2[6] host	B17-2[6] e.l.	B21[6] host	B21[6] e.l.
Type:	IIIB	IIIB	Sp Lz	Sp Lz	Sp Lz	Sp Lz	Dunite	Dunite
No.:	5	3	8	3	10	5	5	5
SiO_2	50·4 (3)	52·9 (3)	51·3 (3)	53·9 (2)	51·7 (6)	54·7 (1)	52·1 (2)	55·5 (1)
TiO_2	1·04 (23)	0·14 (1)	0·50 (4)	0·07 (1)	0·61 (8)	0·07 (4)	0·44 (5)	0·08 (1)
Cr_2O_3	0·07 (3)	0·04 (0)	0·93 (5)	0·58 (2)	0·84 (6)	0·48 (5)	3·22 (10)	1·26 (2)
Al_2O_3	9·09 (71)	7·53 (32)	7·50 (19)	5·60 (9)	7·73 (46)	5·29 (29)	4·98 (17)	2·99 (8)
FeO	3·67 (56)	9·77 (8)	2·68 (12)	6·83 (7)	3·09 (54)	8·11 (31)	2·21 (6)	5·96 (11)
MnO	0·09 (2)	0·16 (3)	0·09 (4)	0·16 (5)	0·09 (3)	0·18 (4)	0·17 (47)	0·00 (0)
NiO	0·05 (4)	0·09 (3)	0·04 (2)	0·10 (1)	0·05 (5)	0·08 (4)	0·04 (2)	0·10 (2)
MgO	13·7 (6)	29·8 (4)	13·9 (3)	32·0 (8)	14·2 (15)	32·0 (6)	15·0 (4)	33·4 (6)
CaO	21·6 (9)	0·43 (0)	21·1 (3)	0·39 (0)	20·7 (17)	0·50 (4)	21·8 (6)	0·74 (0)
Na_2O	1·44 (9)	0·03 (1)	1·88 (10)	0·02 (1)	1·86 (20)	0·03 (4)	1·88 (9)	0·06 (1)
Total	101·2	100·9	99·9	99·7	100·9	101·5	101·9	100·1
X_{Mg}	0·869	0·845	0·902	0·893	0·892	0·875	0·924	0·909

Sample:	6[1] reconstr.	CP2[1] reconstr.	B15-3[2] reconstr.	G7 core	P16 core	P21 core	BB91[3] reconstr.
Type:	I	I	II	IIIA	IIIA	IIIA	PSD
No.:	18	10	10	9	9	5	8
SiO_2	52·9 (6)	52·3 (5)	49·5 (3)	52·8 (5)	50·2 (4)	51·0 (3)	52·1 (2)
TiO_2	0·29 (7)	0·30 (5)	1·03 (6)	0·58 (8)	0·71 (7)	0·92 (8)	0·76 (4)
Cr_2O_3	1·74 (20)	1·72 (10)	0·57 (2)	0·02 (2)	0·08 (5)	0·43 (5)	0·16 (6)
Al_2O_3	5·66 (38)	5·74 (20)	9·18 (25)	6·99 (68)	8·99 (37)	5·94 (22)	6·44 (33)
FeO	3·18 (50)	3·17 (18)	4·53 (38)	6·16 (127)	5·79 (14)	5·57 (15)	11·86 (67)
MnO	0·10 (3)	0·10 (4)	0·12 (3)	0·08 (4)	0·10 (58)	0·11 (4)	0·30 (2)
NiO	0·05 (4)	0·05 (4)	0·05 (2)	0·07 (3)	0·02 (3)	0·05 (2)	0·02 (3)
MgO	17·5 (22)	17·0 (3)	14·0 (9)	13·0 (15)	11·3 (2)	13·5 (0)	18·7 (7)
CaO	18·3 (24)	18·0 (4)	18·1 (9)	18·5 (20)	20·9 (2)	21·1 (2)	9·4 (9)
Na_2O	1·63 (25)	1·70 (11)	2·11 (27)	2·72 (30)	2·13 (7)	1·58 (9)	1·22 (12)
Total	101·4	100·0	99·2	101·0	100·2	100·2	101·0
X_{Mg}	0·907	0·905	0·846	0·790	0·777	0·812	0·737

(continued)

Table 4: Continued

Sample:	B7 core	B15 core	P33 core	B9[4] reconstr.	B47-3 core	B47 core	B46-3 core
Type:	IIIB	IIIB	IIIB	IIIB	IV	IV	IV
No.:	8	25	5	8	5	10	6
SiO_2	47·5 (2)	51·4 (6)	52·4 (3)	50·8 (3)	51·7 (6)	52·4 (3)	50·9 (4)
TiO_2	0·66 (2)	0·77 (14)	0·88 (5)	0·91 (20)	0·31 (2)	0·06 (4)	0·25 (5)
Cr_2O_3	0·13 (2)	0·22 (6)	0·17 (1)	0·06 (2)	0·84 (3)	0·36 (8)	0·12 (5)
Al_2O_3	13·05 (18)	9·38 (58)	6·53 (29)	8·86 (65)	5·90 (11)	6·08 (25)	11·29 (29)
FeO	4·62 (13)	4·53 (113)	3·72 (115)	4·59 (49)	2·97 (5)	3·12 (14)	2·98 (16)
MnO	0·08 (3)	0·12 (3)	0·07 (6)	0·10 (2)	0·00 (0)	0·05 (4)	0·04 (2)
NiO	0·03 (2)	0·05 (2)	0·07 (2)	0·06 (4)	0·05 (4)	0·04 (3)	0·02 (3)
MgO	11·2 (1)	14·3 (28)	14·8 (18)	16·1 (6)	14·8 (5)	15·1 (2)	11·9 (2)
CaO	19·9 (2)	18·7 (32)	20·2 (31)	18·4 (7)	22·0 (5)	22·2 (3)	19·4 (3)
Na_2O	2·38 (7)	2·01 (41)	1·76 (17)	1·23 (8)	1·76 (10)	1·31 (5)	2·99 (12)
Total	99·5	101·4	100·6	101·1	100·4	100·8	100·0
X_{Mg}	0·812	0·849	0·877	0·862	0·899	0·896	0·877

Sample:	B46-1 core	B45 core	LZP4[5] reconstr.
Type:	IV	IV	Sp Lz
No.:	10	5	11
SiO_2	53·2 (2)	52·9 (7)	51·4 (3)
TiO_2	0·38 (3)	0·39 (4)	0·48 (3)
Cr_2O_3	0·79 (5)	0·36 (6)	0·91 (5)
Al_2O_3	6·88 (21)	8·87 (19)	7·41 (18)
FeO	3·11 (15)	3·08 (60)	2·89 (12)
MnO	0·08 (3)	0·04 (4)	0·09 (4)
NiO	0·04 (2)	0·05 (4)	0·04 (2)
MgO	14·2 (3)	13·3 (13)	14·8 (3)
CaO	20·7 (3)	19·6 (18)	20·1 (3)
Na_2O	2·09 (11)	2·59 (11)	1·79 (9)
Total	101·5	101·2	99·9
X_{Mg}	0·891	0·885	0·901

Sample:	B17-2[6] reconstr.	B48 core	B21[6] reconstr.
Type	Sp Lz	Dunite	Dunite
No.:	15	9	8
SiO_2	52·0 (6)	52·8 (13)	52·5 (2)
TiO_2	0·55 (7)	0·12 (3)	0·40 (5)
Cr_2O_3	0·79 (6)	1·07 (7)	2·98 (9)
Al_2O_3	7·44 (44)	4·10 (27)	4·74 (16)
FeO	3·69 (51)	2·55 (71)	2·66 (6)
MnO	0·10 (3)	0·08 (3)	0·15 (41)
NiO	0·05 (5)	0·05 (3)	0·05 (2)
MgO	16·4 (14)	16·4 (17)	17·2 (4)
CaO	18·3 (15)	21·5 (24)	19·3 (5)
Na_2O	1·64 (18)	1·24 (24)	1·67 (8)
Total	100·9	100·0	101·7
X_{Mg}	0·888	0·920	0·920

Types are the same as in Table 2. No., number of measurements. Host, cpx host; e.l., opx exsolution lamellae; reconstr., calculated from cpx host and opx e.l. based on per cent exsolution lamellae when applicable. Values in parentheses represent the 2σ standard deviation of the last unit cited.
[1]14%, [2]8%, [3]50%, [4]15%, [5]5%, [6]12% correspond to estimated opx exsolution lamellae content in cpx based on back-scattered images. Reconstructed cpx values are given for the corresponding samples using the general formula: cpx corrected = [x e.l. + (1 − x) host].

Table 5: Selected average EMPA opx major elements representative for each pyroxenite and peridotite sample

Sample:	CP2[2] opx	CP2[2] e.l.	B48[1] opx	B48[1] e.l.	B21[3] opx	B21[3] e.l.	6 core	CP2[2] reconstr.
Type:	I	I	Hz	Hz	Hz	Hz	I	I
No.:	5	3	5	3	3	3	10	8
SiO_2	53·3 (2)	51·2 (2)	54·7 (3)	51·9 (3)	54·8 (6)	51·3 (13)	55·8 (3)	53·0 (2)
TiO_2	0·11 (2)	0·38 (2)	0·04 (1)	0·17 (1)	0·15 (5)	0·75 (2)	0·12 (5)	0·14 (2)
Cr_2O_3	0·92 (2)	1·81 (5)	0·98 (5)	1·97 (6)	1·53 (1)	3·49 (5)	0·86 (10)	1·05 (2)
Al_2O_3	4·37 (13)	5·79 (8)	4·22 (12)	5·55 (5)	3·44 (6)	5·48 (6)	3·74 (30)	4·57 (12)
FeO	6·29 (10)	2·50 (14)	5·93 (10)	2·40 (4)	5·73 (7)	2·25 (3)	6·14 (14)	5·76 (10)
MnO	0·14 (6)	0·07 (2)	0·15 (3)	0·08 (2)	0·00 (0)	0·00 (0)	0·14 (3)	0·13 (5)
NiO	0·10 (2)	0·05 (2)	0·10 (2)	0·06 (2)	0·11 (2)	0·06 (3)	0·10 (3)	0·10 (2)
MgO	33·3 (1)	14·6 (1)	33·4 (3)	14·8 (2)	33·6 (7)	15·7 (3)	33·9 (5)	30·7 (1)
CaO	0·74 (16)	20·8 (4)	0·57 (10)	22·0 (1)	0·73 (53)	20·4 (33)	0·81 (34)	3·54 (20)
Na_2O	0·09 (5)	2·06 (16)	0·05 (2)	1·59 (4)	0·08 (6)	1·89 (24)	0·06 (6)	0·36 (7)
Total	99·3	99·2	100·2	100·5	100·1	101·4	101·7	99·3
X_{Mg}	0·904	0·912	0·909	0·917	0·913	0·926	0·908	0·905

Sample:	B15-3 core	B15 core	P33 core	B46-1 core	LZP4 core	B17-2 core	B48[1] reconstr.	B21[3] reconstr.
Type:	II	IIIB	IIIB	IV	Sp Lz	Sp Lz	Hz	Hz
No.:	5	19	1	3	4	6	8	6
SiO_2	53·3 (12)	53·3 (16)	54·9	56·3 (2)	53·5 (8)	53·8 (1)	54·4 (3)	54·5 (7)
TiO_2	0·28 (4)	0·18 (6)	0·17	0·06 (1)	0·12 (5)	0·15 (4)	0·05 (1)	0·20 (4)
Cr_2O_3	0·26 (3)	0·17 (4)	0·09	0·31 (2)	0·41 (5)	0·48 (3)	1·08 (5)	1·68 (1)
Al_2O_3	5·82 (27)	7·01 (144)	4·13	3·78 (4)	4·93 (105)	6·16 (15)	4·36 (11)	3·61 (6)
FeO	9·86 (30)	9·71 (31)	8·45	8·15 (7)	6·28 (17)	7·21 (28)	5·58 (10)	5·45 (7)
MnO	0·16 (1)	0·15 (3)	0·10	0·14 (2)	0·15 (3)	0·14 (3)	0·15 (3)	0·00 (0)
NiO	0·09 (3)	0·10 (2)	0·15	0·07 (3)	0·10 (2)	0·10 (3)	0·10 (2)	0·11 (2)
MgO	30·1 (5)	30·3 (16)	32·4	31·9 (10)	32·8 (10)	32·3 (5)	31·6 (3)	32·1 (6)
CaO	0·78 (65)	0·45 (18)	0·44	0·47 (1)	0·73 (75)	0·73 (44)	2·71 (11)	2·31 (52)
Na_2O	0·06 (3)	0·04 (7)	0·01	0·02 (2)	0·05 (5)	0·07 (7)	0·20 (2)	0·22 (8)
Total	100·7	101·5	100·9	101·2	99·1	101·2	100·2	100·2
X_{Mg}	0·845	0·848	0·872	0·875	0·903	0·889	0·910	0·913

Types are the same as in Table 2. No., number of measurements. Host, opx host; e.l., cpx exsolution lamellae; reconstr., calculated from opx host and cpx e.l. based on per cent exsolution lamellae when applicable. Values in parentheses represent the 2σ standard deviation of the last unit cited.
[1]10%, [2]14%, [3]8% correspond to estimated cpx exsolution lamellae content in opx based on backscattered images. Reconstructed cpx values are given for the corresponding samples using the general formula: opx corrected = [x e.l. + (1 − x) host].

SiO_2 in Type-I pyroxenites and peridotites may be related to the composition of the infiltrating melts.

Type-II pyroxenites have variably high Mg-number ranging from 83·7 to 90·0. Their Cr_2O_3 and NiO contents are similar to those observed in the host peridotites, possibly indicating re-equilibration and, in part, incorporation of mantle minerals during sample preparation as a consequence of the very thin Type-II pyroxenite bands sampled. Nevertheless, some Type-II pyroxenites contain higher amounts of TiO_2, Na_2O, Al_2O_3 and CaO than the peridotites, plotting close to Type-IIIB pyroxenites, whereas their SiO_2 concentrations remain close to those of the peridotites. This is consistent with their mineral chemistry, in particular with the relatively high Ti and Al contents in cpx compared with Type-I pyroxenites.

Type-IIIA pyroxenites show the largest spread in major element composition and include the most evolved samples of this study; they have the lowest Cr and Ni

Table 6: Selected average EMPA spinel major elements representative for each pyroxenite and peridotite sample

Sample:	CP2	6	B15-3	B47-3	B46-3	LZP4	B17-2	LZP2	B48
Type:	I	I	II	IV	IV	Sp Lz	Sp Lz	Sp Lz	Dunite
No.:	3	3	5	3	6	3	8	3	3
TiO_2	0·16 (2)	0·23 (8)	0·08 (2)	<0·01	<0·02	0·08 (0)	0·08 (3)	0·11 (4)	0·10 (2)
Cr_2O_3	25·0 (2)	29·5 (1)	5·4 (1)	1·3 (0)	1·1 (1)	10·8 (1)	8·5 (2)	15·1 (2)	31·1 (3)
Al_2O_3	42·6 (3)	38·6 (1)	61·6 (2)	64·8 (5)	65·8 (5)	56·2 (2)	58·3 (4)	49·3 (3)	41·5 (2)
FeO	14·2 (2)	14·9 (1)	14·6 (2)	12·6 (1)	13·2 (3)	11·8 (1)	12·6 (1)	13·5 (2)	15·7 (2)
MnO	0·15 (2)	0·17 (2)	0·11 (5)	0·00 (0)	0·08 (2)	0·10 (1)	0·11 (2)	0·12 (2)	0·19 (1)
NiO	0·24 (2)	0·21 (3)	0·45 (4)	0·40 (5)	0·35 (2)	0·40 (1)	0·41 (6)	0·35 (5)	0·19 (2)
MgO	18·6 (2)	17·9 (2)	19·4 (1)	19·5 (3)	20·8 (3)	20·5 (1)	20·6 (2)	19·9 (0)	17·2 (1)
Total	101·0	101·5	101·7	98·6	101·3	99·8	100·6	98·3	105·9
Cr-no.	0·282	0·339	0·056	0·014	0·011	0·114	0·089	0·170	0·334
Fe^{3+}	0·087	0·087	0·052	0·019	0·054	0·057	0·066	0·109	0·038
Fe^{2+}	0·238	0·258	0·258	0·249	0·221	0·198	0·204	0·195	0·310
yAl	0·687	0·632	0·920	0·977	0·962	0·860	0·880	0·785	0·653
yFe	0·044	0·043	0·026	0·009	0·027	0·029	0·033	0·055	0·019
yCr	0·270	0·324	0·054	0·013	0·010	0·111	0·086	0·161	0·328

Types are the same as in Table 2. No., number of measurements. Values in parentheses represent the 2σ standard deviation of the last unit cited. The Cr-number is the Cr/(Al + Cr) ratios with the atoms in mol per formula unit normalized to three cations. Fe^{3+} and Fe^{2+} calculated based on charge balance. yAl, yFe and yCr correspond to mol% based on (Al + Fe + Cr).

concentrations and lower Mg-number than other pyroxenite types. Type-IIIB pyroxenites have more restricted but higher Mg-numbers ranging from 78·0 to 85·1, and intermediate Cr and Ni concentrations. Type-IV pyroxenites have intermediate Cr and Ni concentrations and relatively high Mg-number, similar to Type-IIIB pyroxenites, but elevated CaO, Al_2O_3 and Na_2O and low TiO_2. Type-III pyroxenites have similar high Al_2O_3 and CaO contents to Type-IV owing to the presence of garnet, plagioclase, spinel and Al-rich cpx, but significantly lower Na_2O, indicating that plagioclase in Type-III pyroxenites is likely of metamorphic origin, in accordance with textural observations. SiO_2 concentrations correlate positively with Mg-number and negatively with modal garnet (including kelyphitized garnet) for Type-III garnet pyroxenites. SiO_2 variations are most pronounced in Type-IIIA garnet pyroxenites. Positive correlations of Mg-number and SiO_2 have also been observed for garnetites, garnet-bearing hornblendites and pyroxenites from the lower part of the Kohistan arc (Jagoutz, 2010; Jagoutz *et al.*, 2011), and can be attributed to magmatic accumulation of garnet. Similar trends for garnet pyroxenites have previously been observed in studies of Beni Bousera (Kornprobst, 1969; Pearson *et al.*, 1993; Kumar *et al.*, 1996).

FeO/MgO ratios of Type-III and -IV pyroxenites correlate positively with Al_2O_3, with highly variable FeO/MgO at slightly increasing Al_2O_3 for Type-IIIA pyroxenites, and slightly increasing FeO/MgO with more variable Al_2O_3 for Type-IIIB and -IV pyroxenites (Fig. 9). The high variability in FeO in Type-IIIA pyroxenites is similar to that in the Type-I pyroxenites of Kornprobst *et al.* (1990). The low FeO contents of Type-IV metagabbros together with their high Al_2O_3 and Mg-number, is similar to those of Type-II pyroxenites of Kornprobst *et al.* (1990). Type-IIIB pyroxenites are intermediate between the two types of Kornprobst *et al.* (1990). Type-I and -II pyroxenites represent a different class of pyroxenites with the lowest FeO/MgO ratios and Al_2O_3 contents.

In peridotites, Na_2O, Al_2O_3, CaO are negatively correlated with Mg-number, in accordance with previous studies of the Beni Bousera and Ronda massifs (e.g. Frey *et al.*, 1985; Pearson *et al.*, 1993; Lenoir *et al.*, 2001).

Bulk-rock trace elements

Trace element patterns are distinct for each pyroxenite type. Type-I Cr-diopside websterites (Fig. 10a) are generally characterized by the highest light rare earth element of middle rare earth element (LREE/HREE) ratios compared with all other pyroxenites of the Beni-Bousera massif. LREE and MREE are slightly enriched compared with heavy REE (HREE), with the MREE slightly elevated over the LREE. Overall, REE concentrations are slightly higher than for primitive mantle. Furthermore, there is a systematic high field strength element (HFSE;

Table 7: Selected average EMPA garnet major elements representative for each pyroxenite and peridotite sample

Sample:	G7	P16	P21	BB91	B15	B7	B9	P33	B47
Type:	IIIA	IIIA	IIIA	PSD	IIIB	IIIB	IIIB	IIIB	IV
No.:	5	8	5	5	20	5	8	5	5
SiO_2	40·2 (2)	40·1 (2)	40·7 (3)	41·3 (2)	42·7 (3)	41·6 (3)	42·5 (3)	42·4 (3)	42·8 (1)
TiO_2	0·12 (7)	0·20 (4)	0·24 (3)	0·29 (6)	0·32 (4)	0·14 (2)	0·29 (3)	0·29 (3)	0·05 (2)
Cr_2O_3	0·03 (3)	0·05 (4)	0·46 (3)	0·22 (6)	0·29 (5)	0·09 (1)	0·08 (1)	0·32 (2)	0·38 (5)
Al_2O_3	23·1 (1)	22·8 (1)	22·6 (1)	22·7 (2)	23·3 (2)	24·7 (2)	23·1 (1)	23·5 (2)	23·3 (1)
FeO	17·5 (2)	19·0 (2)	14·6 (2)	17·5 (4)	10·2 (3)	14·5 (3)	9·5 (1)	9·5 (2)	8·5 (1)
MnO	0·34 (2)	0·49 (5)	0·39 (3)	0·68 (2)	0·33 (3)	0·33 (3)	0·30 (2)	0·27 (1)	0·25 (2)
MgO	15·5 (4)	11·8 (2)	16·1 (2)	14·2 (4)	20·2 (4)	16·2 (1)	19·4 (3)	20·0 (2)	20·8 (2)
CaO	4·74 (6)	8·12 (14)	5·49 (16)	4·75 (6)	4·95 (14)	5·72 (8)	5·47 (5)	5·01 (8)	5·67 (8)
Na_2O	0·04 (2)	0·03 (4)	0·03 (2)	0·06 (3)	0·04 (3)	0·02 (2)	0·02 (2)	0·03 (2)	0·01 (2)
Total	101·5	102·6	100·6	101·7	102·4	103·3	100·7	101·4	101·7
X_{Mg}	0·612	0·527	0·662	0·592	0·778	0·667	0·784	0·789	0·814
Alm	0·254	0·301	0·240	0·344	0·157	0·254	0·176	0·157	0·122
Sps	0·006	0·009	0·008	0·014	0·006	0·006	0·006	0·005	0·005
Prp	0·509	0·398	0·544	0·507	0·662	0·557	0·668	0·672	0·677
Grs	0·112	0·196	0·134	0·122	0·117	0·141	0·135	0·121	0·133
Adr	0·117	0·095	0·061	0·008	0·050	0·038	0·012	0·036	0·054
Uvt	0·001	0·001	0·013	0·006	0·008	0·003	0·002	0·009	0·011

Sample:	B45	B47-3	B46-3	B46-1
Type	IV	IV	IV	IV
Nr	5	5	6	8
SiO_2	42·6 (1)	41·1 (2)	42·2 (3)	42·6 (2)
TiO_2	0·07 (5)	0·06 (3)	0·08 (2)	0·15 (2)
Cr_2O_3	0·14 (8)	0·32 (2)	0·25 (2)	0·79 (3)
Al_2O_3	23·8 (2)	22·9 (3)	23·7 (1)	24·6 (2)
FeO	10·9 (2)	8·1 (2)	9·4 (2)	9·1 (2)
MnO	0·21 (5)	–	0·20 (3)	0·29 (3)
MgO	18·3 (2)	20·5 (2)	20·0 (2)	19·6 (7)
CaO	6·52 (3)	4·93 (3)	5·73 (14)	5·13 (4)
Na_2O	0·02 (1)	0·07 (4)	0·01 (2)	0·02 (2)
Total	102·6	98·1	101·5	102·4
X_{Mg}	0·749	0·818	0·791	0·793
Alm	0·181	0·131	0·135	0·175
Sps	0·004	–	0·004	0·006
Prp	0·615	0·685	0·657	0·671
Grs	0·157	0·121	0·135	0·126
Adr	0·039	0·054	0·062	0·000
Uvt	0·004	0·010	0·007	0·022

Types are the same as in Table 2. No., number of measurements. Values in parentheses represent the 2σ standard deviation of the last unit cited. Alm, almandine; Sps, spessartine; Prp, pyrope; Grs, grossular; Adr, andradite; Uvt, uvarovite.

Table 8: Cpx trace element concentrations (ppm) measured by LA-ICP-MS

Sample:	6	CP2	B21	B15-3	G7	P16	BB91	P21
Type:	I	I	I	II	IIIA	IIIA	IIIA	IIIA
No.:	3	2	3	4	3	5	4	4
Ba	–	–	–	–	*0·429* (362)	–	–	–
Th	0·136 (73)	0·138 (104)	0·870 (459)	*0·022* (3)	–	–	–	*0·023* (18)
U	*0·034* (10)	*0·039* (6)	0·107 (51)	–	–	–	–	*0·014* (6)
Nb	0·204 (102)	0·221 (163)	0·310 (279)	*0·076* (44)	*0·050* (17)	–	–	*0·119* (40)
Ta	–	–	*0·053* (36)	–	–	–	–	–
La	2·384 (273)	2·394 (890)	9·283 (1081)	0·999 (137)	0·123 (42)	–	–	0·775 (293)
Ce	8·945 (803)	9·018 (2429)	29·343 (2919)	4·691 (515)	0·964 (181)	0·057 (21)	0·046 (18)	3·458 (771)
Pb	*0·195* (136)	*0·150* (140)	0·281 (141)	*0·054* (46)	–	–	*0·095* (133)	*0·039* (28)
Pr	1·498 (147)	1·552 (583)	4·448 (350)	0·998 (127)	0·247 (83)	*0·030* (12)	*0·026* (10)	0·745 (164)
Sr	135·3 (64)	139·7 (280)	167·7 (222)	63·7 (48)	51·7 (116)	2·2 (8)	1·0 (4)	60·3 (37)
Nd	8·270 (990)	8·782 (1979)	21·135 (2257)	6·790 (1126)	2·134 (569)	*0·230* (125)	*0·209* (96)	5·062 (1330)
Hf	0·972 (242)	0·956 (460)	0·891 (322)	1·663 (383)	0·540 (170)	*0·285* (95)	*0·368* (72)	0·654 (245)
Zr	32·65 (800)	26·11 (540)	31·77 (560)	57·27 (980)	15·72 (530)	7·74 (530)	5·28 (90)	14·16 (620)
Ti	1807 (266)	1615 (413)	2567 (482)	5718 (595)	4816 (513)	4584 (913)	4065 (656)	5611 (958)
Sm	2·522 (435)	2·542 (782)	4·561 (659)	2·889 (698)	0·861 (217)	*0·480* (204)	*0·274* (117)	2·155 (550)
Eu	0·921 (167)	0·885 (250)	1·235 (147)	1·129 (135)	0·343 (55)	*0·103* (48)	*0·125* (56)	0·810 (255)
Gd	2·812 (655)	2·613 (597)	3·700 (1025)	4·195 (957)	1·015 (390)	0·914 (322)	0·803 (180)	2·355 (595)
Tb	0·397 (100)	0·383 (139)	0·458 (71)	0·759 (170)	0·142 (55)	0·174 (90)	0·156 (49)	0·295 (111)
Dy	2·376 (504)	2·299 (742)	2·356 (439)	4·915 (848)	0·913 (368)	0·848 (484)	1·143 (223)	1·374 (483)
Ho	0·440 (102)	0·411 (133)	0·392 (88)	0·986 (225)	0·160 (71)	0·129 (87)	0·207 (62)	0·185 (111)
Er	1·113 (299)	1·317 (541)	0·996 (246)	2·927 (731)	*0·370* (192)	*0·441* (247)	*0·459* (206)	*0·302* (185)
Yb	0·784 (401)	0·755 (404)	0·831 (286)	2·686 (532)	*0·315* (138)	*0·288* (148)	*0·286* (165)	*0·183* (108)
Lu	0·113 (48)	*0·095* (37)	*0·085* (41)	0·352 (125)	*0·042* (11)	*0·042* (17)	*0·041* (12)	*0·024* (12)

Sample:	P33	B9	B15	B7	B45	B47	B46-3	B46-1
Type:	IIIB	IIIB	IIIB	IIIB	IV	IV	IV	IV
No.:	2	3	3	3	2	3	5	2
Ba	–	–	–	–	*0·379* (234)	*0·232* (104)	*0·385* (157)	*0·313* (97)
Th	*0·053* (13)	*0·053* (27)	*0·046* (9)	–	–	–	–	–
U	*0·031* (10)	–	–	–	–	–	–	–
Nb	0·244 (48)	0·309 (160)	–	*0·080* (16)	–	*0·047* (11)	–	*0·052* (23)
Ta	*0·049* (19)	*0·048* (14)	–	–	–	–	–	–
La	2·189 (201)	0·888 (161)	1·522 (306)	0·433 (79)	0·361 (183)	0·168 (59)	0·392 (143)	0·472 (74)
Ce	8·793 (1684)	3·357 (659)	6·760 (759)	1·855 (242)	1·613 (544)	0·527 (101)	1·500 (437)	1·795 (200)
Pb	*0·068* (23)	*0·062* (6)	0·179 (82)	*0·078* (33)	*0·145* (59)	*0·069* (38)	*0·108* (100)	*0·127* (48)
Pr	1·504 (266)	0·677 (195)	1·190 (170)	0·323 (84)	0·339 (61)	0·082 (29)	0·301 (110)	0·347 (91)
Sr	97·6 (140)	86·9 (85)	72·5 (76)	48·5 (11)	168·9 (179)	96·2 (72)	307·1 (925)	271·5 (132)
Nd	8·542 (1139)	4·762 (1335)	6·280 (1163)	2·161 (280)	2·257 (318)	0·531 (203)	1·830 (547)	2·157 (567)
Hf	1·312 (108)	0·881 (451)	0·835 (221)	0·419 (103)	*0·348* (188)	–	0·484 (181)	*0·322* (140)
Zr	39·90 (280)	23·38 (1140)	23·52 (300)	8·53 (210)	8·74 (220)	*0·79* (50)	7·54 (450)	8·10 (300)
Ti	4596 (752)	5644 (1298)	3910 (552)	3352 (156)	2183 (274)	389 (46)	1793 (818)	2395 (91)
Sm	2·510 (391)	2·101 (490)	1·906 (577)	0·900 (367)	0·803 (203)	*0·189* (94)	0·618 (270)	0·837 (184)
Eu	0·811 (181)	0·808 (187)	0·647 (131)	0·375 (111)	0·405 (110)	*0·105* (43)	0·286 (112)	0·434 (141)
Gd	1·768 (497)	2·743 (490)	2·217 (633)	1·113 (270)	0·678 (264)	*0·187* (25)	*0·620* (256)	0·816 (136)
Tb	0·184 (27)	0·356 (79)	0·343 (104)	0·156 (59)	*0·072* (22)	–	*0·067* (31)	0·121 (50)
Dy	0·799 (161)	2·059 (408)	1·995 (442)	0·925 (315)	*0·278* (109)	–	*0·344* (150)	*0·392* (91)
Ho	*0·093* (18)	0·322 (103)	0·344 (109)	0·139 (61)	*0·051* (15)	–	*0·067* (35)	*0·065* (28)
Er	*0·143* (56)	0·677 (192)	0·838 (293)	*0·305* (99)	–	–	*0·188* (29)	–
Yb	–	*0·387* (140)	*0·663* (159)	*0·330* (122)	–	–	–	–
Lu	–	*0·046* (14)	*0·080* (27)	–	–	–	–	–

(continued)

Table 8: Continued

Sample:	B47-3	LZP4	B17
Type:	IV	Sp Lz	Sp Lz
No.:	3	5	5
Ba	–	*0·235* (65)	–
Th	–	–	–
U	–	–	–
Nb	–	*0·094* (35)	*0·101* (76)
Ta	–	–	–
La	0·256 (65)	0·769 (126)	1·024 (174)
Ce	0·985 (98)	2·892 (356)	3·901 (449)
Pb	*0·097* (85)	*0·077* (37)	*0·101* (18)
Pr	0·206 (72)	0·576 (76)	0·739 (121)
Sr	127·9 (71)	63·9 (69)	74·5 (54)
Nd	1·322 (321)	3·562 (801)	4·388 (686)
Hf	*0·227* (89)	0·734 (263)	0·906 (403)
Zr	3·83 (150)	23·28 (490)	30·54 (370)
Ti	1473 (501)	2592 (292)	3102 (324)
Sm	*0·474* (210)	1·418 (466)	1·740 (554)
Eu	0·258 (98)	0·610 (149)	0·726 (230)
Gd	*0·439* (176)	2·233 (712)	2·525 (813)
Tb	*0·064* (36)	0·427 (93)	0·481 (86)
Dy	*0·245* (99)	3·023 (581)	3·189 (423)
Ho	*0·037* (10)	0·648 (137)	0·642 (155)
Er	–	1·954 (553)	2·015 (574)
Yb	–	1·919 (604)	1·766 (523)
Lu	–	0·260 (152)	0·263 (93)

No., number of different minerals analyzed per thin section. No values are under detection limit. LOD and LOQ are given in Appendix 4. Italic values represent data values between LOD and LOQ. Values in parentheses represent the 2σ standard deviation.

Hf, Ti and Zr) depletion and a positive Pb anomaly that may relate, together with the LREE and MREE variations, to the pyroxenite parent melt, as the presence of opx in these pyroxenites (60–80 vol. %) precludes the Ti and Zr depletions in the bulk-rock of Type-I pyroxenites being related solely as a result of the incorporation of those elements into fractionating opx (Rampone *et al.*, 1991). Metasomatized mantle has shown to exhibit similar HFSE-depleted patterns (e.g. Ionov *et al.*, 2002; Scambelluri *et al.*, 2006). The depletion of Nb and Ta relative to La is frequently used as a fingerprint for arc magmatic settings that display significant Nb/La fractionation (e.g. Kelemen *et al.*, 1993). Nb and, to a lesser extent, Ta are depleted in Type-I pyroxenites over neighboring elements with similar incompatibilities, with Nb_N/La_N ratios ranging between 0·11 and 0·22.

Type-II spinel websterites (Fig. 10a) are characterized by a more pronounced LREE depletion compared with the MREE and HREE, contrasting with the Type-I pyroxenites. Furthermore, Type-II pyroxenites do not have significant negative Zr and Hf anomalies, and have only slight Ti anomalies, in accordance with the large modal amounts of opx in Type-II (40–50 vol. %). Type-II pyroxenites have a slight depletion of Nb and Ta, with fractionated Nb_N/La_N ratios ranging between 0·10 and 0·26, similarly to Type-I pyroxenites.

Type-III garnet pyroxenites (Fig. 10c and d) have generally convex-upward REE patterns comparable with 'group A' pyroxenites from the Ronda massif (e.g. Suen & Frey, 1987; Garrido & Bodinier, 1999) and with the previously described garnet pyroxenites of the Beni Bousera massif (e.g. Loubet & Allègre, 1982; Kornprobst *et al.*, 1990; Pearson *et al.*, 1991, 1993). They correlate with the geochemical characteristics of the Type-I pyroxenites of Kornprobst *et al.* (1990). The trace element patterns of Type-III pyroxenites show significant variations in

Table 9: Garnet trace element concentrations (ppm) measured by LA-ICP-MS

Sample:	P21	G7	P16	BB91	P33	B15	B9	B45
Type:	IIIA	IIIA	IIIA	PSD	IIIB	IIIB	IIIB	IV
No.:	3	5	6	6	3	1	3	4
La	–	–	–	–	–	–	–	–
Ce	*0·029* (13)	–	–	–	*0·058* (49)	–	–	–
Pb	–	*0·092* (25)	–	–	–	–	–	–
Pr	–	–	–	–	0·029 (18)	–	–	–
Sr	*0·072* (49)	0·356 (231)	0·269 (153)	–	*0·088* (53)	–	*0·073* (27)	0·581 (310)
Nd	*0·350* (156)	–	–	–	0·482 (248)	0·626 (378)	*0·294* (137)	*0·227* (46)
Hf	0·331 (135)	*0·249* (156)	–	*0·184* (92)	0·501 (160)	0·603 (177)	0·452 (175)	*0·250* (82)
Zr	15·60 (640)	6·17 (620)	3·12 (130)	4·98 (140)	36·24 (580)	38·48 (150)	27·41 (520)	4·33 (160)
Ti	1594 (571)	853 (415)	1011 (260)	1486 (421)	1247 (443)	2132 (457)	1609 (457)	331 (69)
Sm	0·703 (150)	*0·343* (163)	0·323 (169)	*0·172* (74)	0·702 (261)	1·066 (258)	0·615 (197)	*0·299* (97)
Eu	0·523 (92)	0·183 (66)	0·135 (68)	0·142 (77)	0·390 (78)	0·529 (103)	0·438 (138)	0·282 (67)
Gd	3·135 (291)	0·898 (271)	2·223 (737)	1·529 (393)	1·733 (266)	2·540 (759)	2·480 (501)	1·159 (334)
Tb	0·697 (114)	0·297 (120)	0·769 (161)	0·599 (182)	0·355 (88)	0·591 (139)	0·614 (89)	0·268 (81)
Dy	6·068 (607)	3·098 (1120)	7·947 (1441)	6·852 (1276)	2·584 (358)	5·052 (1187)	5·567 (985)	1·986 (351)
Ho	1·520 (103)	0·939 (249)	2·240 (384)	1·938 (418)	0·560 (77)	1·109 (192)	1·309 (96)	0·418 (94)
Er	4·563 (335)	3·814 (1080)	8·231 (1274)	7·727 (1523)	1·888 (157)	3·545 (560)	4·483 (527)	1·390 (397)
Yb	4·814 (757)	5·049 (1599)	9·630 (1842)	9·625 (2150)	1·547 (457)	4·332 (775)	4·817 (1080)	1·437 (548)
Lu	0·718 (79)	0·815 (189)	1·492 (275)	1·495 (333)	0·227 (52)	0·706 (60)	0·705 (140)	0·165 (48)

Sample:	B47	B46-3	B46-1	B47-3
Type:	IV	IV	IV	IV
No.:	3	5	3	3
La	–	–	–	–
Ce	–	–	–	–
Pb	–	–	–	–
Pr	–	–	–	–
Sr	–	0·173 (109)	–	–
Nd	–	*0·240* (154)	*0·288* (61)	–
Hf	–	*0·262* (90)	*0·217* (105)	–
Zr	*0·87* (60)	9·61 (290)	12·42 (250)	2·81 (120)
Ti	185 (48)	516 (294)	690 (89)	304 (29)
Sm	–	*0·365* (161)	*0·359* (160)	–
Eu	*0·107* (26)	0·275 (117)	0·333 (92)	0·147 (61)
Gd	*0·315* (96)	1·001 (491)	1·180 (322)	*0·372* (149)
Tb	*0·050* (26)	0·231 (90)	0·293 (131)	0·109 (33)
Dy	*0·234* (119)	1·696 (716)	2·457 (832)	0·933 (189)
Ho	*0·061* (34)	0·398 (196)	0·612 (311)	0·211 (86)
Er	*0·189* (62)	1·331 (659)	1·926 (870)	0·697 (233)
Yb	*0·385* (100)	1·121 (773)	1·763 (710)	0·707 (452)
Lu	*0·068* (50)	0·146 (86)	0·326 (144)	*0·080* (39)

No., number of minerals analyzed per thin section. No values are under detection limit. LOD is given in Appendix 4. Italic values represent data values between LOD and LOQ. Values in parentheses represent the 2σ standard deviation.

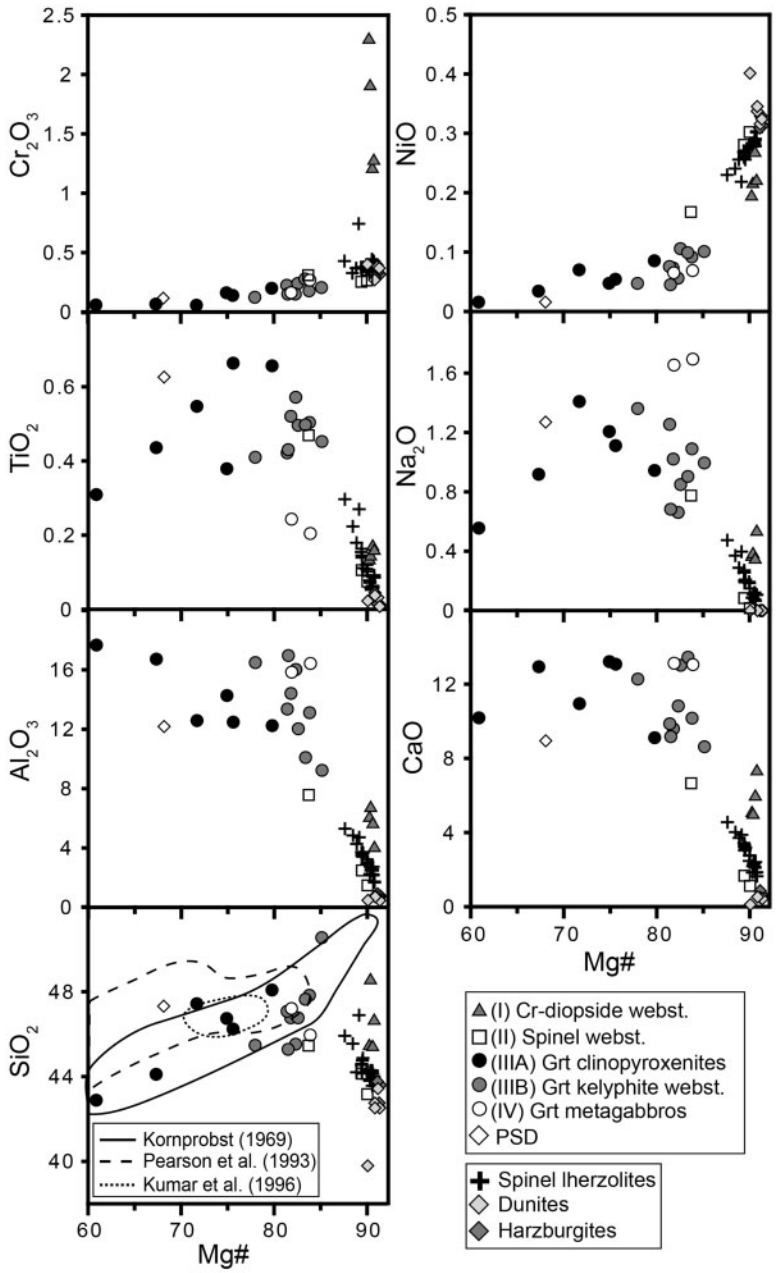

Fig. 8. Bulk-rock major element concentrations (wt %) vs Mg-number of pyroxenites and peridotites.

LREE/HREE ratios and HREE to MREE fractionation. Gd_N/Yb_N ratios of typical Type-IIIB garnet kelyphite websterites range between 0·74 and 1·41 (Fig. 10c), whereas more fractionated Gd_N/Yb_N ratios of 0·19–1·29 are found in Type-IIIA garnet clinopyroxenites (Fig. 10c and d and Table 3). Furthermore, Type-III pyroxenites show positive Pb anomalies, slight positive Sr anomalies and variable HFSE from slightly depleted to enriched, with Type-IIIB having the highest HFSE contents. Nb is strongly depleted and Ta slightly enriched in some cases, with high and variably fractionated Nb_N/La_N varying from 0·02 to 0·67 in Type-III pyroxenites and unfractionated in the PSD with Nb_N/La_N of 0·96. Certain Type-IIIA pyroxenites are characterized by high HREE/LREE ratios and fractionated HREE to MREE, and display two distinct patterns illustrated in Fig. 10d: (1) samples B44 and G7 have relatively undepleted LREE–MREE patterns; (2) sample BB91 (PSD) and P16 have LREE depletions compared with other Type-III pyroxenites. Samples P16 and BB91 have the highest HREE/LREE ratios and fractionated

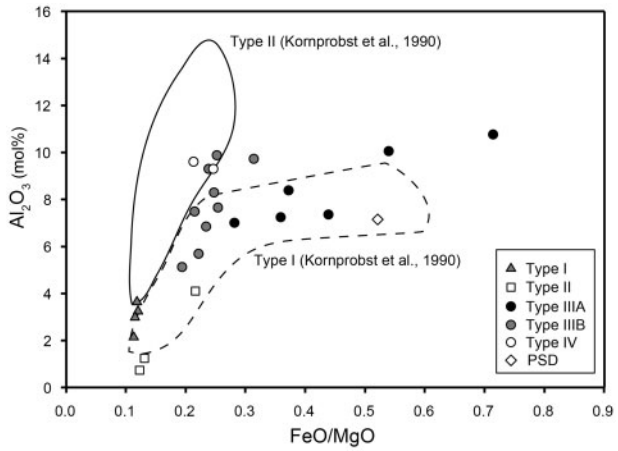

Fig. 9. Comparison of bulk-rock Al_2O_3 vs FeO/MgO of the pyroxenites from this study with the pyroxenite types defined by Kornprobst *et al.* (1990). Type-IIIA pyroxenites are characterized by a strong FeO enrichment whereas Type-IIIB and -IV have a weak increase in FeO/MgO with increasing Al_2O_3.

HREE to MREE with Gd_N/Yb_N ratios of 0·19–0·27. They are distinguished from samples G7 and B44 by their much steeper LREE/HREE patterns. The high HREE contents of these pyroxenites correlate with their higher modal amounts of garnet compared with other Type-III pyroxenites. The trace element patterns of these garnet pyroxenites display typically negative Eu anomalies [$Eu_N/Eu^*_N = 0{\cdot}48–0{\cdot}73$, with $Eu^* = (Sm \times Gd)^{0{\cdot}5}$] and positive Sr, Pb and Ti anomalies.

Type-IV garnet metagabbros (Fig. 10c) are characterized by positive Eu anomalies ($Eu_N/Eu^*_N = 1{\cdot}35–1{\cdot}57$), LREE depletion, and low and flat HREE patterns similar to the Type-II corundum-bearing clinopyroxenites of Kornprobst *et al.* (1990), and to certain garnet websterites analyzed by Pearson *et al.* (1993). In Type-IV metagabbros, HREE are the lowest of all garnet-bearing pyroxenites and the MREE/HREE are close to unity, despite the presence of 20–40% garnet. This suggests that garnet in the Type-IV metagabbros is dominantly metamorphic. High positive Sr anomalies associated with a positive Eu anomalies and elevated Na_2O contents indicate together that the plagioclase observed in these rocks may be of original magmatic origin (Kornprobst *et al.*, 1990) and thus formed by shallow-level crystallization (<15 kbar). Furthermore, Type-IV garnet metagabbros are depleted in HFSE and show a strong Nb_N/La_N fractionation (0·05–0·11) similar to the lower crust in arc settings (e.g. Jagoutz *et al.*, 2011).

Spinel lherzolites are compared in Fig. 10b, with secondary spinel lherzolites occurring within pyroxenite-rich zones (sample B5 and B17). The Beni Bousera spinel lherzolites are REE depleted compared with primitive mantle, except for sample B5. Samples B5 and B17

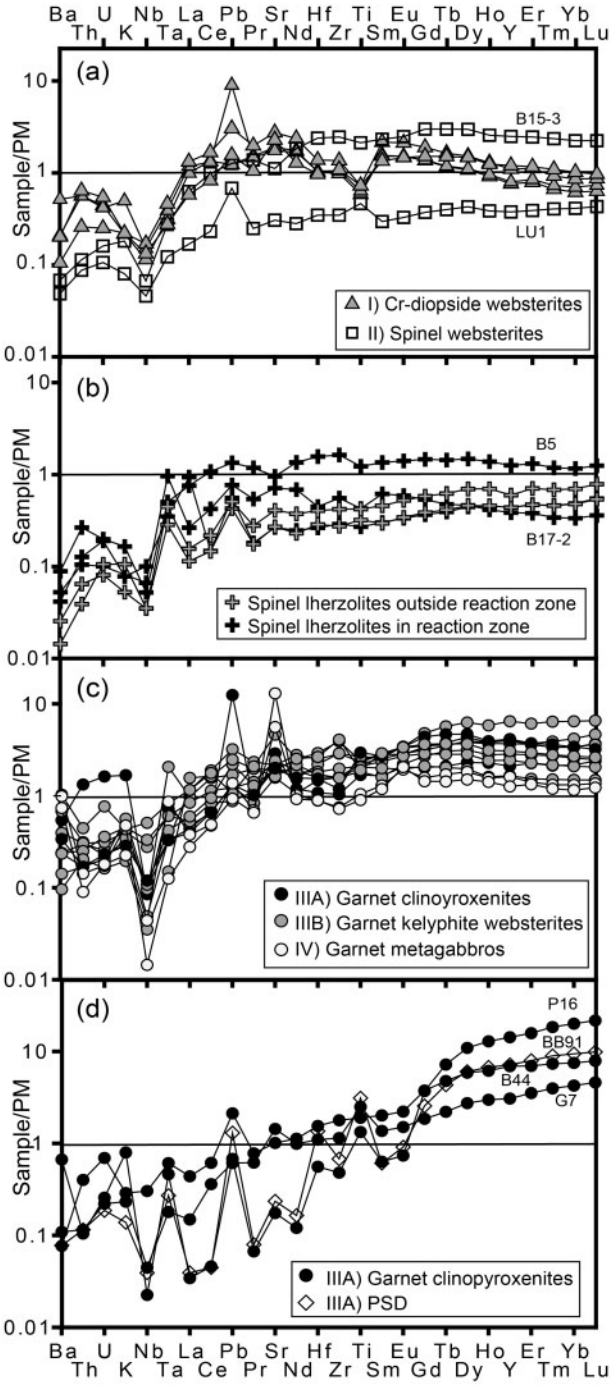

Fig. 10. Bulk-rock trace element concentrations normalized to primitive mantle (McDonough & Sun, 1995). (a) Type-I and Type-II pyroxenites. (b) Spinel lherzolites and secondary spinel lherzolites (samples B17-2 and B5). (c) Comparison between Type-IIIA, -IIIB and Type-IV pyroxenites. (d) Comparison between highly fractionated HREE to MREE Type-IIIA garnet pyroxenites with the high-pressure graphite pseudomorph after diamond garnet pyroxenite pattern (PSD).

represent refertilized spinel lherzolites with LREE enrichment and high Ba, U, and Th compared with spinel lherzolites occurring outside the pyroxenite-rich zones. The latter are characterized by higher LREE/HREE fractionation than refertilized lherzolites and by positive Ta and Pb anomalies. The peridotites, similar to all observed pyroxenites, have fractionated Nb_N/La_N (0·07–0·29).

MAJOR ELEMENT MINERAL CHEMISTRY

Clinopyroxene

Cpx displays a variety of subsolidus re-equilibration textures ranging from simple, small-scale (<1 to 5 μm) to larger-scale (5–10 μm) opx exsolution lamellae in the cpx of the Type-I and -II pyroxenites to multiple opx, garnet and plagioclase exsolutions in part recrystallized to neoblasts around older cpx porphyroclasts; for example, in the diamond-pseudomorph-bearing garnet pyroxenites (PSD). Additionally, cpx show moderate core to rim zonation. In our analyses, we differentiated between older porphyroclasts and younger neoblasts, and reintegrated where possible exsolved cpx to their original compositions.

Figure 11 shows the composition of host cpx and associated opx exsolution lamellae and reconstructed compositions of exsolved pyroxenes (containing >5% lamellae). Cpx cores from each pyroxenite type have distinct Fe/Mg but vary considerably in Ca/Mg, the latter being attributable to subsolidus re-equilibration upon cooling towards more Ca-rich compositions. Host cpx grains that have not been reintegrated for opx exsolution lamellae have, as expected, higher Ca contents (Fig. 11a) than reconstructed cpx compositions (Fig. 11b; see also Table 4). As mentioned above, the most pronounced cpx subsolidus re-equilibration is present in pyroxenites with diamond pseudomorphs. Their reintegrated cpx plot as a distinct group with low X_{Mg} and Ca, and the highest Fe contents (Fig. 11b). These originally subcalcic augites now contain up to 40–50% opx exsolution lamellae and small-scale exsolution of plagioclase, garnet and spinel. The re-equilibrated cpx hosts have ~16–18 wt % CaO, whereas reintegrated subcalcic augites have 9–12 wt % CaO (Table 4). This is consistent with low-Ca cpx compositions replacing high-Ca cpx with increasing pressure (e.g. Longhi & Bertka, 1996).

Most pyroxenes exhibit some core to rim zonation and/or smaller-scale zonation patterns spatially related to exsolution lamellae. Figure 12 shows the variation in jadeite (Jad) vs Ca-Tschermak (CaTs) component from cpx porphyroclast profiles as well as the composition of secondary neoblasts. The observed zonation of the porphyroclasts is visible in trends of variable jadeite content, reflecting different degrees of subsolidus re-equilibration and opx exsolution during cooling. Inter-sample variations are more pronounced than within-grain variations, indicating that original magmatic variations may be partly preserved. The porphyroclasts are generally characterized by increasing jadeite from core to rim (e.g. in the subcalcic augite porphyroclasts in the PSD). The variations in the CaTs component are less pronounced than for jadeite in the porphyroclast profiles. However, large variations in CaTs component are observed in cpx from Type-IIIB and -IV as well as in Type-IV neoblasts showing increased CaTs component (≥0·2 mol % CaTs) compared with the porphyroclasts. This trend pointing towards the composition of recrystallized cpx exsolution is interpreted as a metamorphic trend. Similar cpx with high CaTs/Jad ratios have been observed in corundum-bearing garnet pyroxenites from the Ronda massif (Morishita *et al.*, 2001) and in the Type-II corundum-bearing garnet pyroxenites of Kornprobst *et al.* (1990), for which prograde metamorphism leading to the formation of corundum (co), sapphirine (saph) or secondary spinel/garnet(II) may be described by the reaction

$$\text{plag} + \text{lowCaTscpx} \pm \text{grt(I)} = \text{highCaTscpx} + \text{grt(II)} \pm \text{co} \pm \text{saph} \pm \text{sp}. \quad (2)$$

The highest CaTs content was found in the Type-IVB sample containing spinel and no plagioclase (B46-3), plotting closer to the secondary recrystallized cpx neoblasts. The presence of opx and spinel in some Type-IV pyroxenites also indicates that the formation of secondary garnet and cpx may be described by the following reaction (e.g. Kushiro & Yoder, 1966):

$$\text{plag} + \text{opx} + \text{cpx} + \text{sp} = \text{grt} \pm \text{cpx}. \quad (3)$$

Both reactions are consistent with our petrographic observations; that is, secondary garnet neoblasts forming along cpx triple points and the presence of only minor amounts of corundum in a few pyroxenite layers (Kornprobst *et al.*, 1990).

The X_{Mg} of cpx porphyroclast cores and reintegrated compositions ranges from 0·75 to 0·92 (Fig. 13; Electronic Appendices 1 and 2; http://www.petrology.oxfordjournals@.org). Cpx neoblasts and cpx porphyroclasts show core to rim zonation that plots between the cpx host and exsolution lamellae compositions, indicating that heterogeneities are associated mainly with subsolidus re-equilibration (Fig. 13). Cr-diopside in Type-I pyroxenites and Cr-diopside pockets in dunites have the highest X_{Mg} (>0·90) and are similar. They have low Al (<0·3 atoms per formula unit; a.p.f.u.) and Ti (<0·015 a.p.f.u.), intermediate Na (~0·10–0·15 a.p.f.u.) and high Cr (≥0·02 a.p.f.u.) compared with cpx from other pyroxenites. Cpx in Type-II spinel websterites is characterized by intermediate X_{Mg} (~0·85), high Al (up to ~0·35 a.p.f.u.)

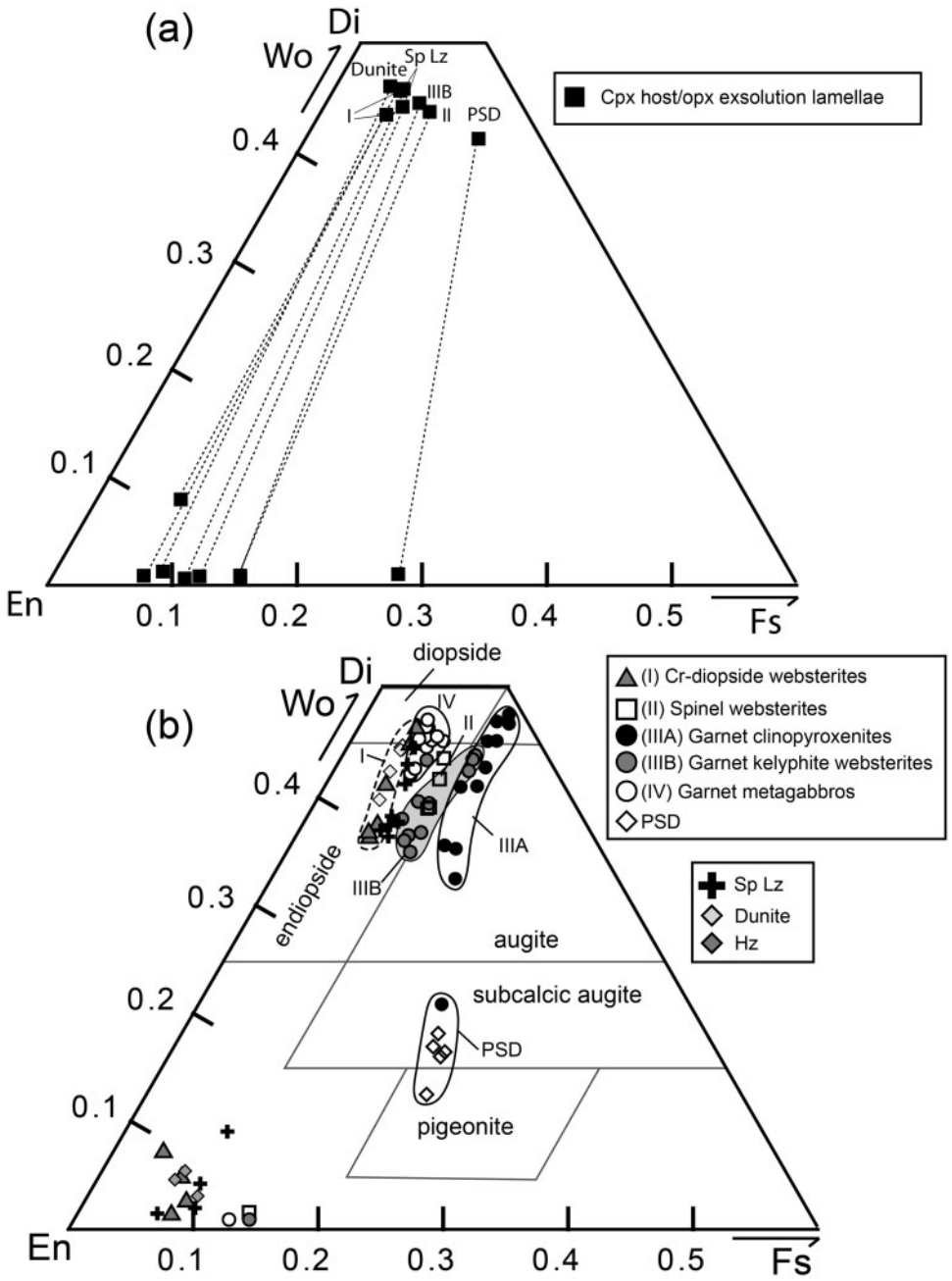

Fig. 11. Pyroxene quadrilateral [cpx normalized after Cawthorn & Collerson (1974)] showing cpx and opx compositions from the Beni Bousera pyroxenites, spinel lherzolites (Sp Lz), harzburgites (Hz) and dunites. (a) Cpx host and corresponding opx exsolution lamellae pairs (dashed lines). (b) Cpx and opx mineral compositions and contour fields of cpx from various pyroxenite types.

and Ti (~0·025–0·03 a.p.f.u.), and intermediate Na (~0·15 a.p.f.u.) and Cr (0·02 a.p.f.u.) concentrations. Type-IIIA augite compositions display the lowest X_{Mg} (<0·85) and intermediate Al (~0·2–0·4 a.p.f.u.), large Na variations (<0·05–0·25 a.p.f.u.), intermediate to high Ti (<0·01 to >0·03 a.p.f.u.) and low Cr contents (<0·02 a.p.f.u.). Secondary cpx neoblasts recrystallized from exsolutions in the PSD are similar to Type-IIIA cpx, indicating that they may result from subsolidus re-equilibration of originally subcalcic augite. Cpx in Type-IIIB pyroxenites is characterized by higher X_{Mg} (~0·85–0·87) than in Type-IIIA, large Al variations (~0·25 to >0·5 a.p.f.u.), intermediate Na (~0·07–0·17 a.p.f.u.) and Ti (~0·015–0·03 a.p.f.u.), and low Cr (<0·01 a.p.f.u.) contents. Secondary neoblasts plot close to most cpx porphyroclasts, in which strong zoning or chemical changes associated with metamorphism are absent.

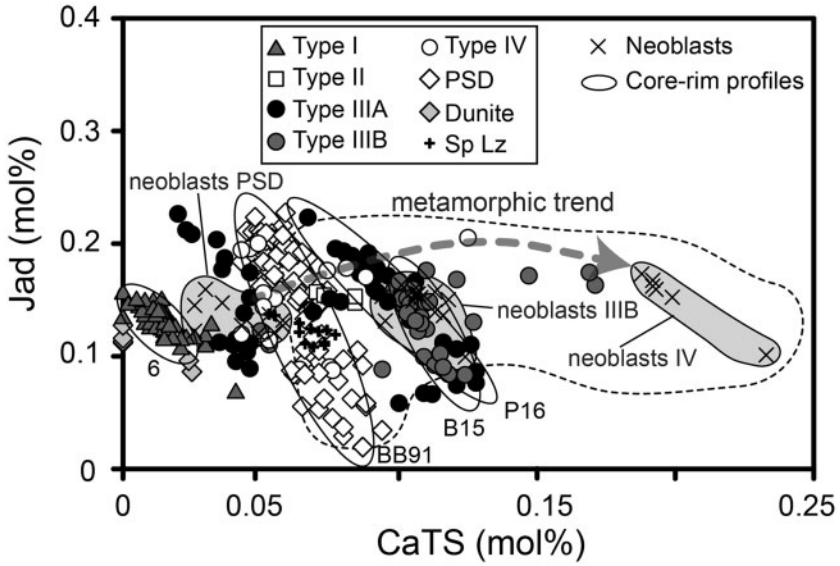

Fig. 12. Jadeite (Jad) vs Ca-Tschermak (CaTs) in cpx porphyroclast profiles, porphyroclast cores and in secondary neoblasts [cpx normalized after Cawthorn & Collerson (1974)]. The trends indicate opx exsolution in the cpx porphyroclasts with variability in the jadeite content, and metamorphic reactions in Type-IIIB and -IV cpx indicated by large variations in the calculated CaTs content towards secondary cpx neoblasts. Sample numbers correspond to core–rim profiles (delineated by ellipses). The dashed line indicates the field for cpx from Type-II pyroxenites from Kornprobst *et al.* (1990).

Type-IV garnet metagabbro cpx is characterized by large variations in Al (~0·20 to >0·50 a.p.f.u.) and Na (<0·10 to ~0·20 a.p.f.u.), but nearly constant low Ti (<0·015 a.p.f.u.) and low to intermediate Cr (<0·01 to ~0·03 a.p.f.u.). Furthermore, their X_{Mg} and Cr contents are higher than in Type-III garnet pyroxenite cpx. Type-IV cpx cores show highly variable Na, Al and CaTs component with strong chemical variations between cores and secondary neoblasts, indicating more important metamorphic reactions in Type-IV pyroxenites compared with other pyroxenites.

From the above observations, three trends can be emphasized. Primarily, the variations in cpx chemistry are due to subsolidus exsolution of opx lamellae upon cooling with relatively constant CaTs and X_{Mg}, and higher variability in jadeite, Ti and Cr contents. Second, exsolved augite, recrystallized in neoblasts from the originally subcalcic augites of the PSD trend towards Type-IIIA cpx compositions. Most probably, Type-IIIA augites result from complete subsolidus re-equilibration of originally subcalcic augites originating from either similar high pressures such as recorded in the PSD samples (from the diamond stability field) or at least from pressures higher than recorded in the exsolved subcalcic augites. Third, cpx porphyroclasts in some Type-IIIB and all Type-IV pyroxenites and their secondary cpx neoblasts show strong compositional variations as a result of exsolution and metamorphic reactions that involve Al-rich phases such as plagioclase, garnet, spinel and rarely corundum or sapphirine owing to pressure changes. Nevertheless, in this study, no corundum or sapphirine was identified in the Type-IV pyroxenites.

Orthopyroxene

Opx porphyroclasts have near constant Ca/Mg ratios (Fig. 11b), except for opx from Type-I Cr-diopside websterites and spinel lherzolites, which have higher and more variable Ca contents. X_{Mg} in opx cores ranges from 0·84 to 0·91. Opx displays core to rim zoning and the formation of secondary neoblasts (see Electronic Appendix 3 and 4, http://www.petrology.oxfordjournals.org). Variations in opx chemistry trend from the opx host towards cpx exsolution lamellae, affecting Al and Ti contents, as in the cpx porphyroclasts. Nevertheless, no significant variations have been observed in the opx, possibly as a result of metamorphic re-equilibration such as observed in cpx for certain Type-IIIB and especially Type-IV pyroxenites. Type-IIIB opx porphyroclasts show the most important exsolution. Recrystallized secondary cpx and opx neoblasts form clusters that reach into the fragmented porphyroclasts. Typical cpx and opx porphyroclast profiles and compositions of secondary cpx and opx neoblasts for Type-IIIB pyroxenites are given in Appendix 5.

Opx core compositions in Type-I pyroxenites are characterized by high X_{Mg} (~0·905), high Cr (0·020–0·030 a.p.f.u.), intermediate Al (0·15–0·19 a.p.f.u.), variable Na (0·005–0·025 a.p.f.u.) and low Ti (~0·003 a.p.f.u.). Furthermore, their cores have variable and high Ca

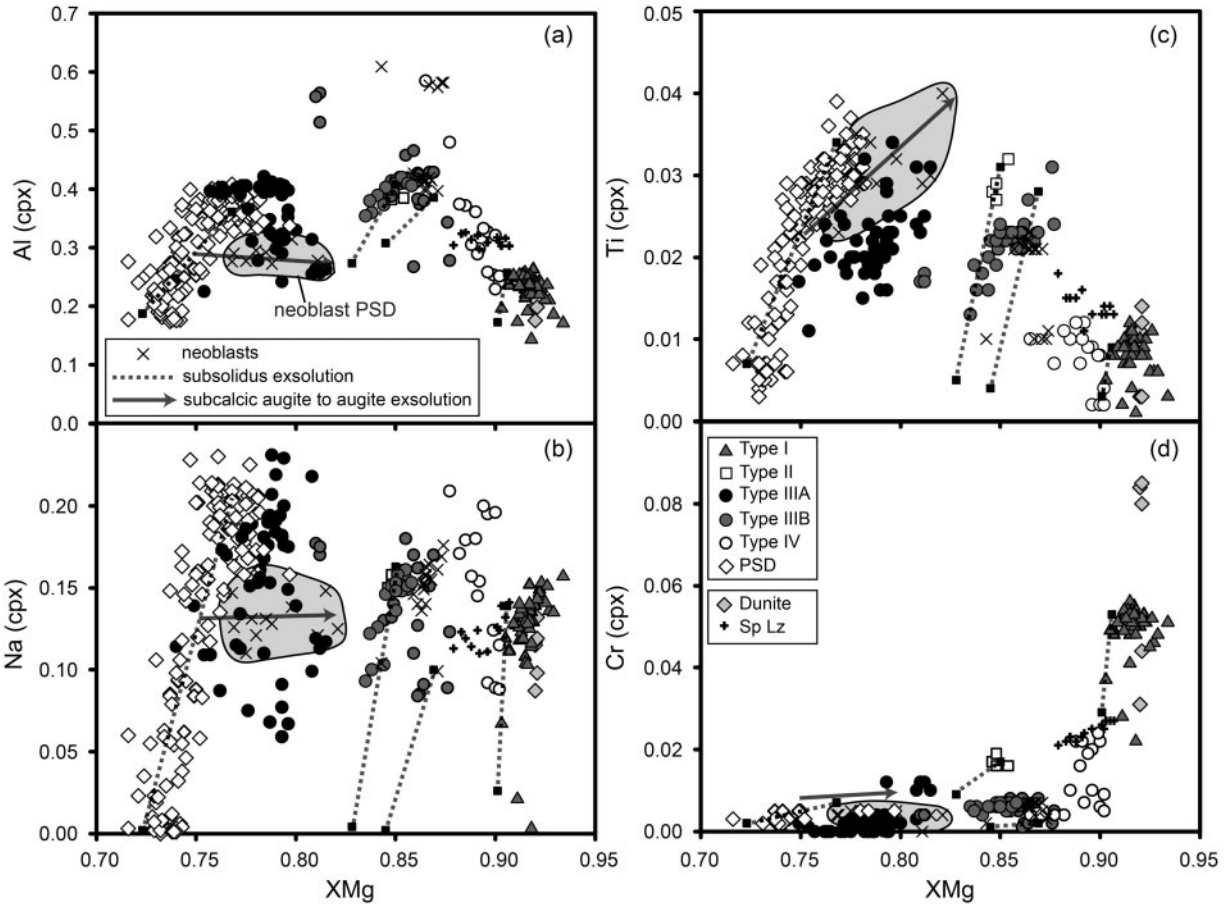

Fig. 13. Cpx chemistry of porphyroclast profiles and secondary cpx neoblasts. The chemical variations in the profiles are dominated by the exsolution of opx in the cpx porphyroclasts. Cpx porphyroclasts in Type-IIIA pyroxenites plot towards augite neoblasts that originate from exsolution of originally subcalcic augite formed at high pressure in the diamond pseudomorph-bearing Type-IIIA garnet pyroxenite (PSD). Typical cpx porphyroclast profiles in Type-IIIB pyroxenite are shown in Appendix 5. Units are atoms per formula unit normalized to six oxygens.

contents of 0·03–0·133 a.p.f.u., whereas other pyroxenites have Ca in opx <0·03 a.p.f.u. Measured core to rim profiles indicate homogeneous porphyroclasts. Opx cores in Type-II pyroxenites are characterized by low X_{Mg} (0·824), high Al (0·24 a.p.f.u.), Ti (0·007 a.p.f.u.) and Cr (0·007 a.p.f.u.), and low Na (0·004 a.p.f.u.). Opx porphyroclast cores in Type-IIIB pyroxenites have intermediate X_{Mg} (0·848–0·872 a.p.f.u.), high and variable Al (0·17–0·31 a.p.f.u.), and low Ti (0·004–0·005 a.p.f.u.), Cr (0·002–0·005 a.p.f.u.) and Na (0–0·003 a.p.f.u.). Porphyroclast profiles show only weak zoning, the inner 100 μm being constant in composition, followed by a decrease in X_{Mg} from 0·852 to 0·845 in the rim (Appendix 5). These porphyroclasts are further characterized by a slight increase of Al towards the rim. Secondary opx neoblasts are enriched in Al, Ca and Na compared with opx porphyroclasts (Appendix 5). This is in agreement with the exsolution of not only opx but also plagioclase, now recrystallized on cpx porphyroclast rims and between secondary opx and cpx. Type-IV pyroxenites have opx with intermediate X_{Mg} (0·875), Al (0·15 a.p.f.u.) and Cr (0·008 a.p.f.u.), and low Ti (0·004 a.p.f.u.) and Na (0·002 a.p.f.u.).

The variations in opx chemistry reflect mainly two processes. Primarily, limited changes in opx chemistry occur owing to subsolidus exsolution in Type-I and -II pyroxenites. Second, zoning in the porphyroclasts of Type-IIIB pyroxenites displays X_{Mg} variations from core to rim, which indicate pressure and temperature variations.

Spinel

Beni Bousera spinels show a clear compositional variations in Cr–Al, with Cr ranging from 0·018 to 0·654 a.p.f.u., Al from 1·258 to 1·953 a.p.f.u. and Fe^{3+} from 0·018 to 0·109 a.p.f.u. In a ternary Cr–Al–Fe^{3+} diagram (Fig. 14a), three groups of spinels may be distinguished. Spinels in Type-I Cr-diopside websterites and dunites are Cr-rich and plot near the field of typical spinels from ocean floor basalts. Hercynite and Cr-spinel in Type-II spinel

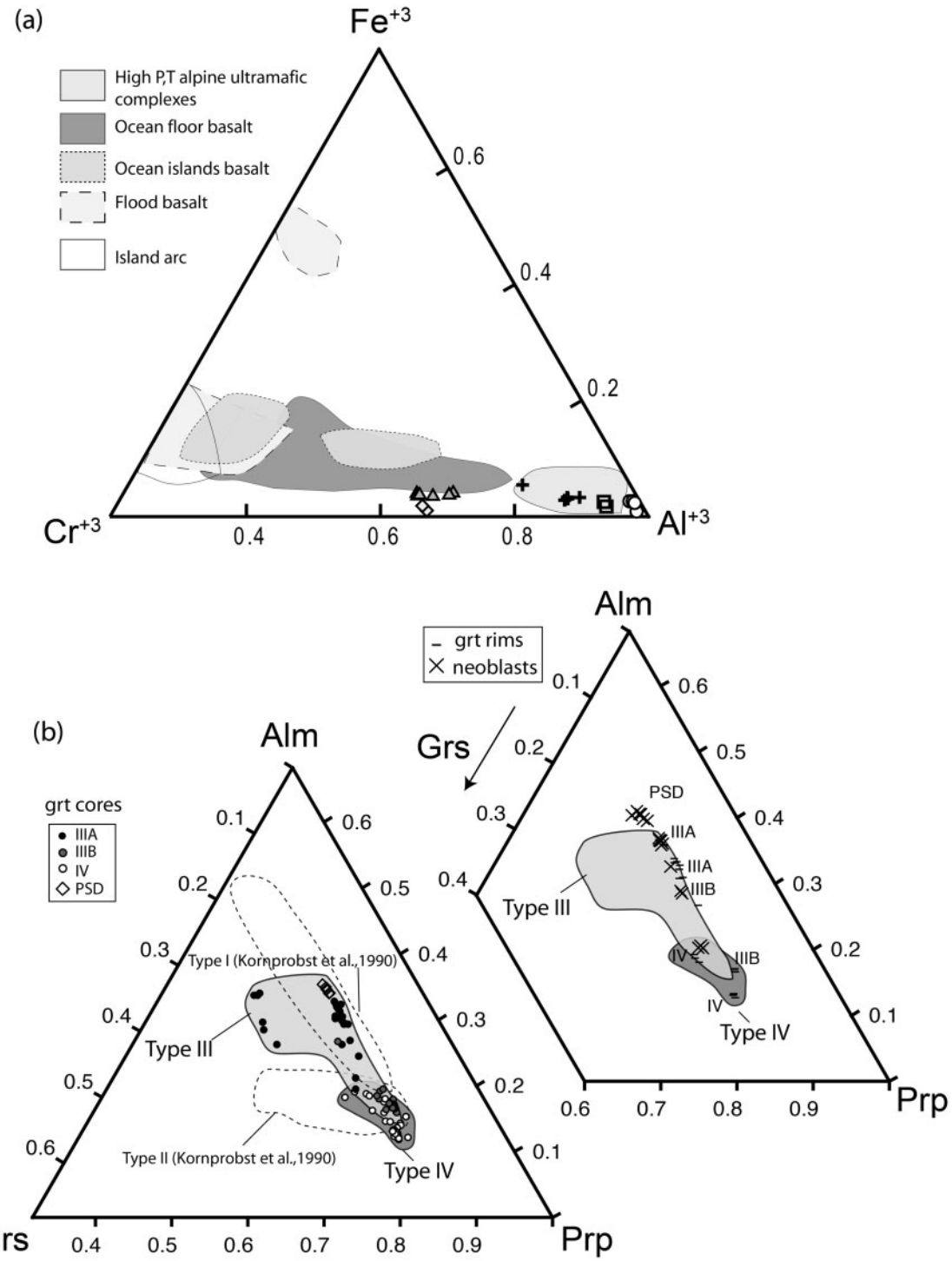

Fig. 14. (a) Spinel chemistry in the Beni Bousera pyroxenites, lherzolites and dunites dominated by a Cr–Al trend. Spinel fields are from data compiled by Barnes & Roeder (2001). (b) Ternary garnet diagram showing the composition of garnet cores, rims and secondary neoblasts. Dashed contour fields from Kornprobst *et al.* (1995) corresponding to their Type-I and Type-II pyroxenites (Kornprobst *et al.*, 1990). Prp, pyrope; Grs, grossular; Alm, almandine.

websterites and spinel lherzolites have intermediate Cr and Al values typical for high-*T* alpine ultramafic complexes (e.g. Barnes & Roeder, 2001). Type-IV garnet metagabbros contain spinels that are the most Al-rich and may originate from a reaction involving an Al-rich phase, such as the recrystallization of plagioclase as described by reaction (2).

Garnet

Garnet cores have X_{Mg} ranging from 0·52 to 0·82 with Type-IIIA pyroxenites having the lowest, Type-IIIB intermediate and Type-IV the highest values. Garnets (Fig. 14b) from the diamond-pseudomorph-bearing pyroxenites and from Type-IIIA pyroxenites plot in the field of garnets from Type-I pyroxenites of Kornprobst *et al.* (1990), Type-IIIB in both fields, and Type-IV garnets plot towards the Type-II pyroxenites of Kornprobst *et al.* (1990). Garnets from Type-III garnet pyroxenites have high, variable Fe contents (0·163–0·354 mol % almandine); garnets from Type-IIIB have the lowest Fe and highest Mg (0·585–0·707 mol % pyrope) compared with Type-IIIA garnets (0·440–0·644 mol % pyrope). Furthermore, Type-IIIA contain garnets enriched in Ca (0·122–0·237 mol % grossular). Garnets in Type-IV pyroxenites have nearly constant Ca and are characterized by high pyrope contents (0·636–0·749 mol %) similar to garnets from Type-IIIB pyroxenites.

Profiles across garnet porphyroclasts display zoning (Electronic Appendix 6) in major elements, except for X_{Mg}, which decreases from core to rim (Fig. 14b). Secondary garnet is characterized by increased Fe and decreased Ca compared with porphyroclast core compositions for both Type-III and -IV pyroxenites. Details of garnet heterogeneities in Type-IV garnet metagabbros (sample B45) are given in Electronic Appendix 7. Garnet neoblasts are depleted in Ca (0·423–0·441 mol %), enriched in Fe (0·688–0·693 mol %) and have lower X_{Mg} (0·735–0·736) compared with porphyroclast core and rim compositions (Ca 0·482–0·491 mol %, Fe 0·631–0·644, X_{Mg} 0·748–0·753 mol %). This is consistent with the formation of secondary garnet from either cpx porphyroclasts and/or secondary recrystallized cpx at increasing pressure.

Olivine

X_{Mg} of olivines in the peridotites varies between 0·884 and 0·904 (Table 2 and Appendix 2). NiO concentrations range from 0·383 to 0·409 wt % and as expected correlate positively with X_{Mg}. Dunites and harzburgites have the highest X_{Mg} and highest Ni contents. The most primitive spinel lherzolite sample (LZP4) has high NiO (0·394 wt %) and X_{Mg} (0·897).

Minor phases

Plagioclase (Appendix 3) is present as an interstitial phase in all except Type-I pyroxenites. Minute grains along pyroxene grain boundaries and in kelyphitic rims have distinct compositions. Plagioclase along grain boundaries is $\sim An_{45-50}$, whereas plagioclase in kelyphites and symplectites is $\sim An_{60}$ and results from destabilization of garnet. Figure 6e and f shows backscattered electron images of garnet and associated kelyphitic reaction rims with compositions listed in Electronic Appendix 7. Kelyphites are mainly composed of opx, Al-rich cpx, plagioclase, spinel and garnet relicts ± amphibole ± Fe–Ti-oxides. Amphiboles are mainly pargasite and pargasitic hornblende. One Type-IIIA pyroxenite (sample G7) with larger amphiboles has an amphibole X_{Mg} of 0·68–0·70, 10·96–11·08 wt % CaO and 0·13–0·14 wt % K_2O (Appendix 3). The presence of amphibole in Type-III pyroxenites indicates that metasomatism might have affected some pyroxenite bands at grain boundaries.

GARNET AND CPX TRACE ELEMENT GEOCHEMISTRY

Garnet and cpx trace element concentrations are listed in Tables 8 and 9. Figure 6g and h shows backscattered electron images of cpx with different opx exsolution lamellae and 40 μm craters resulting from laser ablation. Opx lamellae and their cpx host minerals have been analyzed separately in Type-I and -IIIB pyroxenites with large lamellae (Fig. 6h) to test the effect of exsolution on trace element concentrations. Bulk trace element concentrations measured in exsolved cpx hosts are not significantly shifted, indicating that subsolidus exsolution does not substantially affect cpx trace element patterns. Trace element concentrations are about one order of magnitude lower in opx exsolution lamellae (Appendix 6) compared with the cpx host mineral, consistent with the secondary ionization mass spectrometry (SIMS) study of Hellebrand *et al.* (2005). In their work they concluded that in this context only Ti and Yb are significantly fractionated by opx. Trace element partitioning has been investigated as a function of temperature for cpx–opx in spinel lherzolite xenoliths by Witt-Eickschen & O'Neill (2005). A significant fraction of the incompatible trace elements (in particular Ti and Zr) was found to be held in opx at magmatic temperatures but repartitioning into cpx occurred upon subsolidus cooling. Opx exsolution lamellae in cpx are frequently too thin to be measured separately from the cpx host by LA-ICP-MS (Fig. 6g). We measured several cpx core compositions per thin section and for each pyroxenite suite several samples. Mineral trace element patterns are systematically (within error) identical for a given sample, without significant trace element zoning associated with diffusion or subsolidus re-equilibration. This shows that even though opx exsolution lamellae might present a potential minor problem, average trace element concentrations yield reliable and reproducible results.

Rare earth elements (REE)

Cr-diopsides in Type-I pyroxenites are enriched in LREE compared with MREE and HREE, and are enriched in LREE compared with cpx from other pyroxenite types and spinel lherzolites (Fig. 15). Such high LREE/HREE ratios are comparable with those for cpx from peridotite xenoliths from Spitsbergen, ascribed to result from mantle metasomatism (Ionov *et al.*, 2002). Cpx from a dunite with Cr-diopside–spinel patches (sample B21) is highly enriched in LREE and has similar patterns to cpx in the Type-I Cr-diopside websterites, suggesting that the patches are linked to the Type-I pyroxenites. The HREE depletion in Type-I pyroxenite cpx can be interpreted to result either from garnet fractionation (at greater depth) or from partial melting of a garnet-rich mantle source. Type-II pyroxenite cpx (sample B15-3) have trace element patterns that are slightly enriched in MREE compared with spinel lherzolites. Cpx trace element patterns in Type-II pyroxenites do not have fractionated MREE to HREE, and hence do not indicate any evidence for garnet fractionation, in accordance with the general absence of garnet in these rocks. All cpx grains from Type-III pyroxenites have depleted HREE compared with the MREE, suggesting equilibration of cpx with magmatic garnet. Additionally, three patterns can be distinguished in cpx from Type-III pyroxenites (Fig. 15b): (1) two garnet clinopyroxenite samples (P16 and BB91) have cpx that is strongly depleted in LREE compared with MREE and shows negative Eu anomalies ($Eu_N/Eu^*_N = 0{\cdot}47–0{\cdot}81$); (2) Type-IIIA pyroxenite G7 has intermediate LREE and is enriched in MREE; (3) there is high variability in LREE-enriched patterns corresponding to most Type-IIIA and -IIIB pyroxenites. The REE patterns of cpx in samples P16 and BB91 (the latter containing diamond pseudomorphs) are similar to those of the cpx from the diamond pseudomorph pyroxenites of Pearson *et al.* (1993). In most cases, negative Eu anomalies may be interpreted in terms of plagioclase fractionation, but considering the presence of diamond pseudomorphs and relatively high pressures of formation, the negative Eu anomaly should rather be attributed to a relatively low oxygen fugacity (e.g. Schwandt & McKay, 1998). Cpx in Type-IV pyroxenites (Fig. 15c) is characterized by slight LREE depletion compared with the MREE, low absolute HREE concentrations, mostly close to or below detection limits, and positive Eu anomalies ($Eu_N/Eu^*_N = 1{\cdot}41–1{\cdot}72$), indicating that the cpx now present in these rocks is of metamorphic origin and replaces plagioclase.

Garnets in Type-III pyroxenites (Fig. 16) are highly enriched in HREE compared with MREE with steep convex-upward patterns. Together with the observed bulk-rock HREE enrichment and HREE depletion in cpx, this indicates that the garnet probably results from high-pressure magmatic accumulation as suggested for 'Type-I' pyroxenites by Kornprobst *et al.* (1990). The steepest HREE patterns are found in samples G7, P16 and BB91, with negative Eu anomalies ($Eu_N/Eu^*_N = 0{\cdot}48–0{\cdot}85$) in samples P16 and BB91 (Fig. 16b). Type-IV

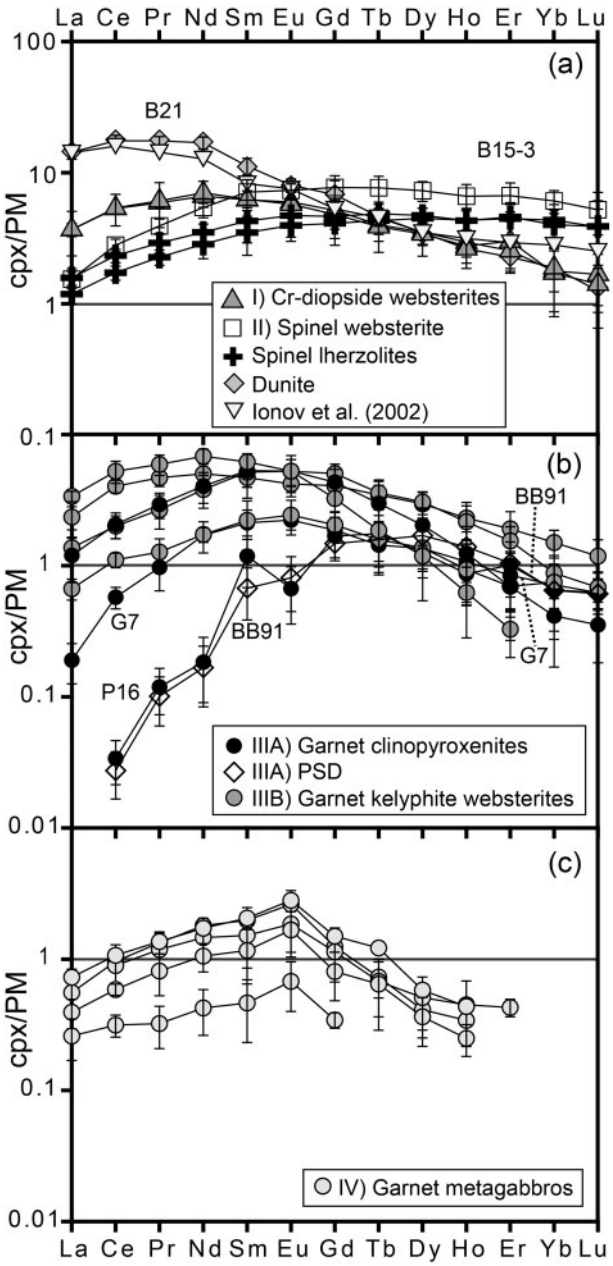

Fig. 15. Cpx REE compositions from Beni Bousera pyroxenites and spinel lherzolites normalized to primitive mantle (McDonough & Sun, 1995). (a) Type-I and -II pyroxenites compared with spinel lherzolites. Cr-diopside formed from Type-I pyroxenite parental melts (in Type-I pyroxenites and in the dunites) shows LREE enriched patterns similar to mantle xenoliths from Ionov *et al.* (2002). (b) Augites from Type-IIIA and -IIIB pyroxenites with variable LREE enrichment patterns. (c) Diopside from Type-IV pyroxenites with positive Eu anomalies. Error bars represent 2σ.

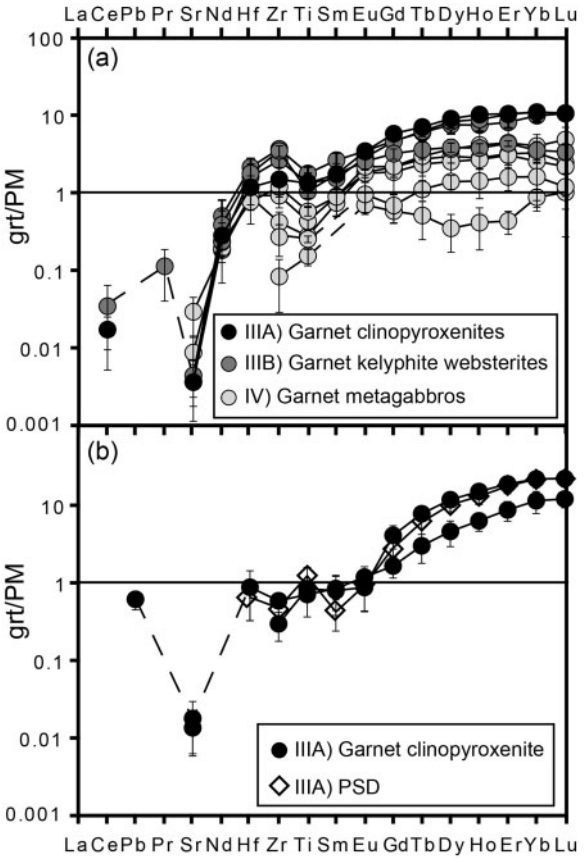

Fig. 16. Garnet trace element compositions from Beni Bousera pyroxenites normalized to primitive mantle (McDonough & Sun, 1995). (a) Comparison between Type-IIIA, -IIIB and -IV pyroxenites. (b) Comparison between some diamond-free Type-IIIA and diamond-pseudomorph-bearing garnet pyroxenites (PSD) with identical patterns. Error bars represent 2σ.

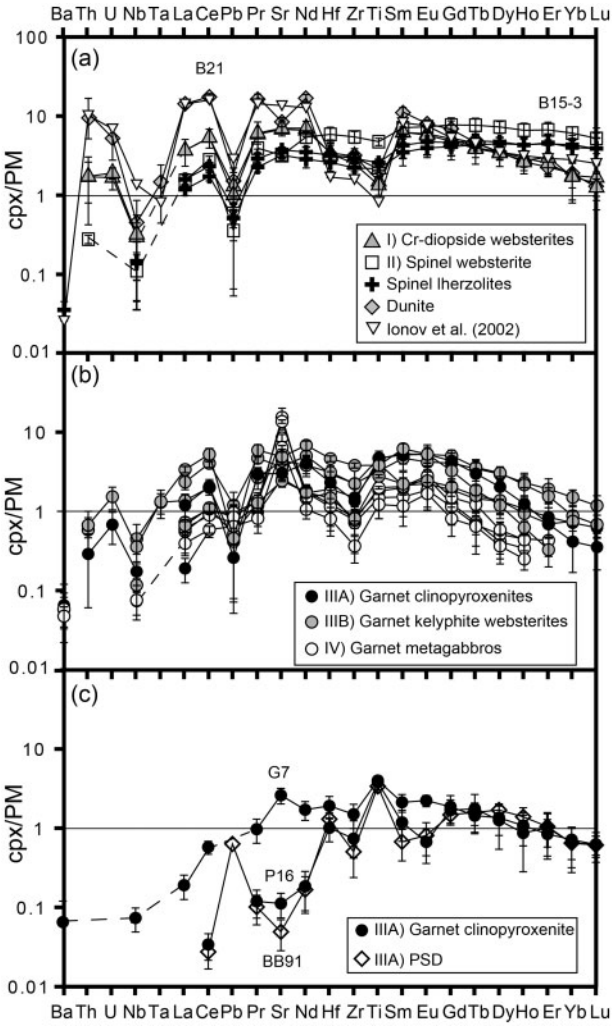

Fig. 17. Clinopyroxene trace element compositions from Beni Bousera pyroxenites and spinel lherzolites normalized to primitive mantle (McDonough & Sun, 1995). (a) Comparison between cpx from Type-I and -II pyroxenites, dunites and spinel lherzolites. (b) Comparison between cpx of Type-IIIA, -IIIB and -IV pyroxenites. (c) Comparison between cpx in Type-IIIA pyroxenites and PSD. For interpretation see text.

pyroxenites exhibit positive Eu anomalies ($Eu_N/Eu^*_N = 1{\cdot}39–1{\cdot}56$) in garnet and flat HREE patterns, suggesting prograde metamorphism of plagioclase to garnet (and cpx). HREE concentrations in garnets from Type-IV pyroxenites are the lowest of all the garnet-bearing pyroxenites of Beni Bousera, reflecting the bulk-rock chemistry and supporting a non-magmatic origin for this type of garnet.

HIGH FIELD STRENGTH ELEMENTS (HFSE) AND OTHER TRACE ELEMENTS

Cr-diopsides in Type-I pyroxenites have primitive mantle normalized $Th_N \geq U_N$ (Fig. 17a), whereas augites in Type-III pyroxenites have $Th_N < U_N$ (Fig. 17b). With increasing depth, cpx in mantle assemblages becomes more aluminous and less calcic, at pressures >15 kbar the ideal radius of the M2-site is reduced such that U^{4+} (0·98 Å) becomes favored over Th^{4+} (1·041 Å) (Wood & Blundy, 1997; Wood *et al.*, 1999; Landwehr *et al.*, 2001). This confirms that Type-I pyroxenites crystallized cpx at lower pressures (<15 kbar) than Type-III pyroxenites. The Nb_N/Ta_N ratios of cpx from the Cr-diopside–spinel patches in dunite associated with Type-I pyroxenite are highly fractionated; that is, 0·32 for sample B21, Ta being below the detection limit for the two other Type-I pyroxenite samples whereas Nb_N varies within a limited range (0·30–0·45). The Zr_N/Hf_N ratio of Cr-diopside in Type-I pyroxenites is between 0·74 and 0·96; that is, weakly frctionated to unfractionated. Furthermore, cpx in Type-I pyroxenites is

characterized by negative HFSE anomalies similar to the bulk-rock chemistry. The Cr-diopside–spinel patch in the dunite also has a negative HFSE anomaly with values similar to the Type-I pyroxenites.

Cpx grains in Type-II pyroxenites show trace element patterns similar to those of cpx from spinel lherzolites (Fig. 17a). Their trace abundances, in particular Th and Nb, are low and often below the detection limit; Pb and Sr exhibit negative anomalies and Ti has a slightly negative one.

Cpx grains in Type-III pyroxenites are less depleted in HFSE, especially in Ti. Type-IIIA and -IIIB cpx mainly show differences in LREE/HREE ratios, whereas the patterns of the other trace elements are similar (Fig. 17b). They show strong negative Pb anomalies, Nb_N/Ta_N fractionation (0·27–0·35), and weakly to highly fractionated Zr_N/Hf_N (0·39–0·82). Figure 17c shows the trace element pattern of cpx from two Type-III pyroxenites (samples G7 and P16) and the diamond-pseudomorph garnet pyroxenite (sample BB91). The cpx from the latter has the most fractionated Zr_N/Hf_N, and is Sr-depleted compared with most cpx in Type-III pyroxenites.

Cpx in Type-IV pyroxenites is characterized by high positive Sr anomalies, low HFSE (Hf, Zr and Ti), and slight negative Pb anomalies (Fig. 17b). Th, U and Ta are below the detection limit. These cpx grains have generally higher Zr_N/Hf_N ratios (0·42–0·68) than in Type-III garnet pyroxenites.

DISCUSSION

Metamorphic vs magmatic relationships

Field relations and microtextural observations indicate that the Beni Bousera pyroxenites have undergone different degrees of subsolidus re-equilibration. To understand the petrogenesis of each pyroxenite type, metamorphic features need to be distinguished from magmatic ones. In the following, we relate microtextural observations to calculated temperatures and pressures for cpx–opx, garnet–cpx and garnet–opx mineral pairs. Together with the garnet and cpx trace element and the bulk-rock chemistry, we then determine which mineral compositions reflect near-magmatic conditions. We use these mineral compositions to calculate their parental melt compositions to constrain the origins and geodynamic settings in which these melts may have formed.

Figure 18 provides an overview of the temperatures and pressures calculated (Table 10) from (1) porphyroclast mineral pairs, (2) opx and garnet exsolved from cpx porphyroclasts (yielding cooling temperatures), and (3) secondary neoblasts formed from cpx and secondary opx-cpx formed from garnet in kelyphites. In general, the calculated temperatures, often of $\leq$1200°C, are typical for these kinds of rocks, and are below the basalt liquidus, inferred to broadly represent the conditions of formation of the melts parental to the pyroxenites.

Type-I pyroxenites mostly record temperatures of ~1200°C at ~11–15 kbar with cpx–opx mineral pairs yielding as low as 900–1000°C at ~12 kbar [pressures calculated from the two-pyroxene barometer of Putirka (2008)]; that is, temperatures of subsolidus re-equilibration. Peak temperatures of ~1350°C are calculated using the cpx–opx thermometer of Brey & Köhler (1990), indicating that near-magmatic temperatures have in part been preserved in Type-I pyroxenites. Type-II pyroxenites record cooling temperatures of ~1000°C at 12 kbar with maximum temperatures reaching 1000–1080°C. Cpx porphyroclasts and exsolved opx lamellae in Type-II pyroxenites yield even lower temperatures of ~800–900°C.

Type-III pyroxenites record large variations in pressure and temperature ranging from the diamond stability field at ~1250°C and >45 kbar in the PSD sample to ~15–30 kbar and ~1175°C, down to cooling temperatures of ~900°C. The calculated pressures of secondary exsolved garnet, cpx and opx recrystallized as neoblasts in the PSD indicate relatively high pressures up to ~35 kbar, whereas exsolved grt and opx lamellae from the subcalcic augite record lower pressures of ~20 kbar, both at ~1070°C. Augites from Type-III pyroxenites have compositions similar to exsolved and recrystallized cpx neoblasts from the originally subcalcic augites from the PSD. This is consistent with the formation of Type-III pyroxenites at temperatures and pressures well in excess of 1070°C and 20 kbar and subsequent subsolidus re-equilibration of most Type-IIIA garnet clinopyroxenites to temperatures of ~900°C and <20 kbar. In this context, the famous graphite pseudomorphs after diamond demonstrate that the melts forming the PSD originated from the diamond stability field (Slodkevitch, 1983; Pearson *et al.*, 1989, 1993), but do not demonstrate that the pyroxenites effectively crystallized in the stability field of diamond (path 1a in Fig. 18). Alternatively, the diamonds could have been transported as xenocrysts in the ascending melts (any path between 1a and 1b in Fig. 18). It is thus possible that the surrounding peridotite (i.e. the massif itself) could have remained somewhat shallower, and thus emplacement pressures could have remained lower, than necessary for diamond formation.

Type-IIIA pyroxenites and the PSD have cpx and garnet pairs with cpx/grt trace element ratios ($D_{cpx/grt}$ in Appendix 7a) comparable with those predicted by experimental partition coefficients (Green *et al.*, 2000), implying that our calculated melts yield correct trace element patterns. The high HREE contents in both bulk-rock and garnet indicate magmatic accumulation of garnet and the cpx/grt trace element partitioning indicates that no major redistribution of trace elements has occurred during the metamorphic overprint. Type-IIIB pyroxenites have

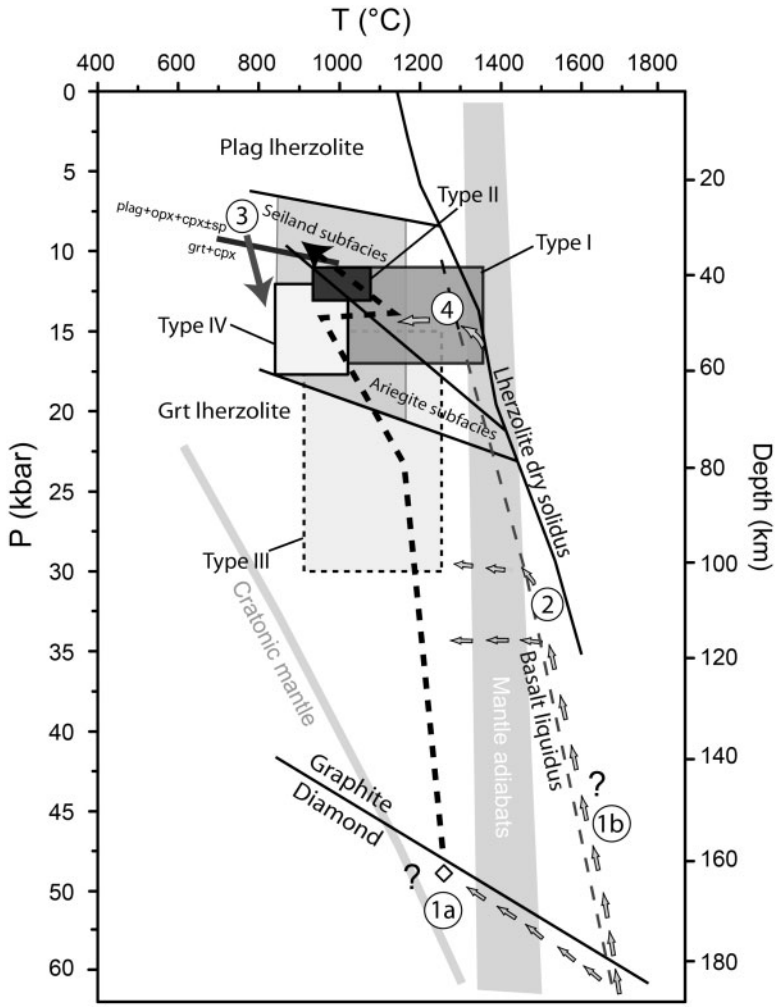

Fig. 18. Pressure–temperature (P–T) diagram with calculated P–T conditions based on geothermobarometry on garnet, cpx and opx porphyroclasts using the values listed in Table 10. Bold dashed line is the inferred P–T path recorded in the Beni Bousera pyroxenites. Path 1a indicates emplacement of the diamond-pseudomorph-bearing garnet pyroxenites in the diamond stability field, whereas path 1b indicates migration of the melts carrying diamond xenocrysts to somewhat shallower levels. (For interpretation see text.) Phase equilibria for Type-IV pyroxenites prograde reaction [see reaction (3) in text] calculated using Perple_X (Connolly, 2005) and the sample B45 bulk composition. Basalt liquidus from Yasuda *et al.* (1994) and Takahashi *et al.* (1998); lherzolite dry solidus from Takahashi (1986) and Takahashi *et al.* (1993); diamond to graphite transition from Kennedy & Kennedy (1976). Mantle adiabats and cratonic mantle geotherm from Rudnick & Nyblade (1999).

$D_{cpx/grt}$ different from the experimentally derived values (Green *et al.*, 2000), especially the HREE (Appendix 7b). This can be related to the presence of metamorphic garnet in some Type-IIIB pyroxenites, corroborating the relatively low pressures of re-equilibration of some garnet–opx pairs at ~15 kbar. Other Type-IIIB pyroxenites record pressures of ~24–30 kbar, closer to those inferred for Type-IIIA pyroxenites. Differences in $D_{cpx/grt}$ may also result from variations in equilibration conditions such as pressure, temperature and H_2O content (Gaetani *et al.*, 2003). The observed variations in $D_{cpx/grt}$ are similar to those observed between hydrous (Green *et al.*, 2000) and anhydrous experiments (Hauri *et al.*, 1994) (see Appendix 7).

Type-IIIB pyroxenites yield metamorphic temperatures of ~900–1130°C. Microtextures show an annealing of exsolution lamellae and large cpx and opx porphyroclasts recrystallizing to undeformed secondary cpx and opx clusters. Furthermore, strongly to totally kelyphitized garnets, as well as the presence of anhedral hercynite, indicate important retrograde reactions. These reactions may have affected the mineral trace element distribution in Type-IIIB pyroxenites, and thus calculated melt compositions have to be interpreted carefully. Kelyphitization continued during the last metamorphic overprint at <12 kbar and <900°C, as kelyphites have also formed on the secondary cpx and opx clusters yielding these P–T conditions.

Table 10: P–T calculations for Beni Bousera pyroxenites and spinel lherzolites

Sample	Type	No.	T (°C)[1] Wells (1977)	T (°C)[2] BKN (1990)	T (°C)[3] NG (2010)	T (°C)[4] NK (2009)	T (°C)[5] E&G (1979)	T (°C)[6] BKN (1990)	T (°C)[7] Taylor (1998)	P (kbar)[1] BKN (1990)	P (kbar)[2] N&G (1985)	P (kbar)[3] Putirka (2008)
Porphyroclasts												
6	I	4	**1036** ± 182	1004 ± 217	–	–	–	1164 ± 246	948 ± 214	–	–	**11** ± 3
CP2	I	3	**1152** ± 68	1150 ± 71	–	–	–	1345 ± 162	1096 ± 77	–	–	**14** ± 4
9X	I	7	**969** ± 158	935 ± 173	–	–	–	1068 ± 175	872 ± 177	–	–	**12** ± 4
B15-3	II	4	**1006** ± 74	981 ± 96	–	–	–	962 ± 8	913 ± 98	–	–	**12** ± 1
G7	IIIA	12	–	–	–	919 ± 129	951 ± 110	–	–	–	–	–
P16	IIIA	5	–	–	–	861 ± 16	929 ± 17	–	–	–	–	–
P21	IIIA	5	–	–	–	884 ± 102	885 ± 91	–	–	–	–	–
BB91	PSD	5	–	–	–	**1253** ± 29	1210 ± 24	–	–	–	–	–
B15	IIIB	5	**1132** ± 65	1119 ± 66	1122 ± 37	1119 ± 51	1154 ± 43	835 ± 14	1091 ± 77	17 ± 2	**15** ± 3	25 ± 3
P33	IIIB	1	**1174** ± 70[a]	1200 ± 30[a]	1094 ± 35[a]	1254 ± 74[a]	1266 ± 85[a]	878 ± 35[a]	1142 ± 35[a]	30 ± 2[a]	**24** ± 3[a]	23 ± 4[a]
B7	IIIB	3	–	–	–	**912** ± 45	965 ± 36	–	–	–	–	–
B9	IIIB	4	–	–	–	**1039** ± 60	1095 ± 52	–	–	–	–	–
B45	IV	2	–	–	–	**884** ± 74[a]	968 ± 85[a]	–	–	–	–	–
B46-3	IV	6	–	–	–	**841** ± 103	921 ± 97	–	–	–	–	–
B47-3	IV	2	–	–	–	654 ± 237	741 ± 233	–	–	–	–	–
B47	IV	3	–	–	–	**838** ± 28	921 ± 85[a]	–	–	–	–	–
B46-1	IV	2	**950** ± 70[a]	927 ± 106	977 ± 35[a]	935 ± 74[a]	1008 ± 85[a]	837 ± 22	858 ± 98	15 ± 3	**14** ± 4	16 ± 3
LZP4	Sp Lz	7	**956** ± 116	921 ± 149	–	–	–	920 ± 21	868 ± 157	–	–	**12** ± 3
B17-2	Sp Lz	4	**1147** ± 16	1154 ± 20	–	–	–	993 ± 44	1110 ± 22	–	–	**15** ± 2
Exsolution lamellae												
CP2	I	1	**843** ± 70[a]	784 ± 30[a]	–	–	–	–	724 ± 35[a]	–	–	**11** ± 4[a]
6	I	1	995 ± 70[a]	982 ± 30[a]	–	–	–	–	937 ± 35[a]	–	–	17 ± 4[a]
B15-3	II	1	**898** ± 70[a]	839 ± 30[a]	–	–	–	–	788 ± 35[a]	–	–	**16** ± 4[a]
B9	IIIB	1	**920** ± 70[a]	839 ± 30[a]	–	–	–	–	827 ± 35[a]	–	–	**15** ± 4[a]
BB91	PSD	5	**1067** ± 40	994 ± 45	810 ± 22	863 ± 26	902 ± 22	919 ± 50	967 ± 47	**20** ± 3	15 ± 2	21 ± 3
LZP4	Sp Lz	1	**839** ± 70[a]	768 ± 30[a]	–	–	–	–	726 ± 35[a]	–	–	**15** ± 4[a]
B17-2	Sp Lz	1	**927** ± 70[a]	885 ± 30[a]	–	–	–	–	836 ± 35[a]	–	–	**14** ± 4[a]
Neoblasts												
B15	IIIB	13	**863** ± 53	808 ± 84	–		–	938 ± 47	769 ± 81	–	–	**13** ± 2
BB91	PSD	12	**1075** ± 94	995 ± 120	801 ± 63	831 ± 113	866 ± 94	987 ± 40	987 ± 128	34 ± 10	**23** ± 6	16 ± 4
B45	IV	5	–	–	–	**775** ± 40	859 ± 43	–	–	–	–	–
Kelyphite												
B45	IV	2	**985** ± 70[a]	845 ± 30[a]	–	–	–	745 ± 96	876 ± 35[a]	–	–	**12** ± 4

Temperatures calculated using: (1) cpx–opx from Wells (1977), (2) cpx–opx from Brey & Köhler (1990), (3) opx–grt from Nimis & Grütter (2010), (4) cpx–grt from Nakamura (2009), (5) cpx–grt from Ellis & Green (1979), (6) Ca-in-opx from Brey & Köhler (1990) corrected according to Nimis & Grütter (2010), (7) cpx–opx from Taylor (1998). Pressures calculated using: (1) opx–grt from Brey & Köhler (1990), (2) opx–grt from Nickel & Green (1985), (3) cpx–opx equation (38) from Putirka (2008). Temperature (2, 3, 6, 7) calculated with pressure (2) if available, otherwise with pressure (3). Temperature (4, 5) calculated with pressure (2) if available, otherwise from pressure estimates (45 kbar for the PSD, 20 kbar for Type-IIIA, 15 kbar for Type-IIIB, 14 kbar for Type-IV). Bold values represented in Fig. 18 as path. Errors represent 1σ from the average of several mineral pairs (No.).
[a]Approximate errors associated to the geothermometer and barometer when number of mineral pairs <3.

Type-IV garnet metagabbros record maximum pressures of ~14 kbar and temperatures between 800 and 980°C. Secondary cpx and garnet neoblasts yield 800°C at ~12 kbar, indicating that the neoblasts formed with increasing pressure as a result of reaction (3). The kelyphites that overprint the neoblasts instead record temperatures of ~980°C, suggesting that they formed during a later prograde stage, possibly associated with a heating event. This is consistent with microtextural evidence (e.g. kelyphitization of large garnet porphyroclasts and secondary neoblasts). Cpx and garnet both show positive Eu anomalies, and cpx grains have high CaTs contents in secondary cpx neoblasts (Fig. 12) consistent with a prograde metamorphism forming secondary garnet and in some cases corundum (Kornprobst *et al.*, 1990) from cpx and primary plagioclase as shown by reaction (2). Furthermore, the low HREE of bulk-rocks containing up to 40% garnet and recrystallization of secondary garnet at cpx triple grain boundaries (Fig. 6e) indicate that the garnet is metamorphic.

Figure 19 shows that most cpx in Type-I-III pyroxenites have low Eu_N/Eu^*_N (~0·8–1·2) and Sr/Nd (~5–25), comparable with the data of Pearson *et al.* (1993), with only one of their samples having Eu_N/Eu^*_N >1·2 and Sr/Nd ~40. In contrast, Type-IV pyroxenites have Eu_N/Eu^*_N >1·4 and Sr/Nd ranging between 80 and 200, implying that plagioclase accumulation has played an important role during the genesis of Type-IV pyroxenites. These observations indicate that garnet and cpx are metamorphic and that Type-IV pyroxenites recrystallized from a cumulate that contained plagioclase. The high Sr contents of ~1430 ppm in interstitial plagioclase (Fig. 5j, sample B45; Electronic Appendix 8) and high bulk-rock Sr (~30–260 ppm) of other Type-IV pyroxenites not containing plagioclase indicate that the plagioclase present is of magmatic origin, that cpx re-equilibrated with plagioclase following reaction (2), and that opx re-equilibrated with plagioclase following reaction (3). The texture of this type of plagioclase is different from that of the retrograde plagioclase exsolving from and recrystallizing along cpx and opx grain boundaries from both porphyroclasts and secondary clusters found mainly in Type-III pyroxenites (Figs 5i and 6c).

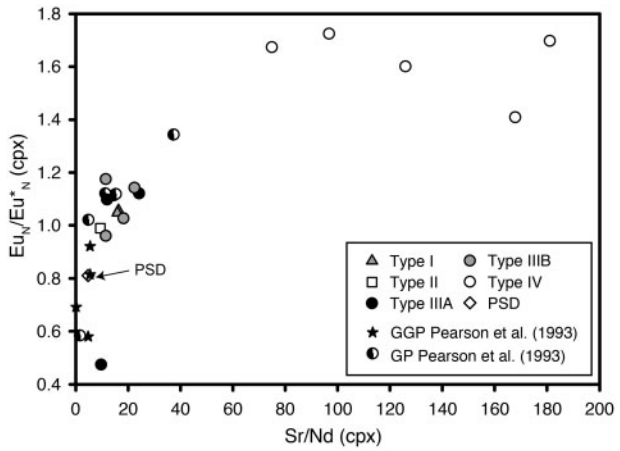

Fig. 19. Mineral Eu_N/Eu^*_N [$Eu^* = (Sm \times Gd)^{0.5}$] normalized to primitive mantle (McDonough & Sun, 1995) vs Sr/Nd ratios in cpx from all pyroxenite types. High Eu_N/Eu^*_N and Sr/Nd ratios of cpx from Type-IV pyroxenites indicate accumulation of magmatic plagioclase. GGP corresponds to cpx from the graphite pseudomorph after diamond-bearing pyroxenite, and GP to cpx from garnet pyroxenites from Pearson *et al.* (1993). Symbols show cpx averages for single samples.

Origin of the mafic rocks and the ultramafic massif

Characteristic features of all the rocks studied from Beni Bousera are the negative Nb and in some instances also Ta anomalies with respect to similarly incompatible elements (e.g. La and K), and positive Pb anomalies. These are typical for arc lavas and deep-seated intrusions in subduction zone settings (e.g. Kelemen *et al.*, 1993, 2003; Jagoutz *et al.*, 2007, 2011). However, using chemical characteristics to infer geodynamic settings is difficult, as the pyroxenites represent cumulates formed by mineral fractionation. Indeed, the overall lack of incompatible element enrichment observed in the mafic and ultramafic rocks of Beni Bousera reflects the dominance of pyroxene, garnet and olivine in their magmatic mineralogy. An influence of a subduction component in the formation of most of the pyroxenites of Beni Bousera is in accordance with their heterogeneous but generally evolved isotopic compositions, which indicate that crustal recycling could account for the geochemical diversity observed in some Beni Bousera pyroxenites (e.g. Allègre & Turcotte, 1986; Hamelin & Allègre, 1988; Pearson *et al.*, 1991, 1993; Blichert-Toft *et al.*, 1999). Below, we first discuss the observed Nb/Ta anomalies, then calculate the trace element compositions of the melts in equilibrium with the preserved magmatic pyroxenite mineralogies (Fig. 20) and finally compare the ultramafic–mafic rocks from Beni Bousera with the ultramafic–mafic cumulates from the Kohistan paleoarc (Fig. 21). We use these observations to infer possible parental melts and discuss the magmatic setting in which the different pyroxenite types were formed.

Nb/Ta fractionation

A striking feature of the trace element characteristics of the pyroxenites and peridotites from Beni Bousera is the highly fractionated Nb/Ta ratios owing to elevated Ta concentrations (Figs 10 and 21). Similar Nb/Ta ratios are observed in the ultramafic and mafic cumulates from the Kohistan arc (Dhuime *et al.*, 2007; Jagoutz *et al.*, 2011) and in the peridotites from the Horoman massif (Takazawa *et al.*, 2000). A positive Ta anomaly is also observed in mineral–melt partition coefficient studies under hydrous

high-pressure conditions (Green *et al.*, 2000). Under elevated pressures (20–75 kbar) and strongly hydrous conditions (5–27 wt %), Green *et al.* (2000) showed that the garnet–melt and cpx–melt partition coefficients (D) result in higher Nb/Ta fractionation ($D_{Ta} > D_{Nb}$) compared with anhydrous experiments. In contrast, recent experiments conducted by Fulmer *et al.* (2010) indicate a much lower partitioning of Nb and Ta into garnet, and that at pressures <25 kbar amphibole plays a more important role in the Nb–Ta budget of hydrous igneous systems.

The driving processes for the Nb/Ta fractionation observed in arcs are generally thought to be controlled by accessory phases in the source and transport through fluids and hydrous melts. Experimental studies have shown the importance of accessory residual phases such as rutile, titanite and allanite on the trace element budget in subduction zones, especially for incompatible elements such as Nb and Ta that are depleted relative to K and LREE (e.g. Klimm *et al.*, 2008). Foley *et al.* (2002) showed that low Nb/Ta, as well as low Nb/La, might result from the crystallization of amphibole from slab-derived, silica-rich aqueous fluids that fractionates Nb from Ta in the residual fluids. This is in accordance with D_{Nb}/D_{Ta} greater than unity for low-Mg-number amphiboles (Tiepolo *et al.*, 2000). The exact reason for the Nb/Ta fractionation observed in the Beni Bousera pyroxenites remains unclear.

Melt composition modelling

The compositions of the melts in equilibrium with cpx and garnet of the Type-I, -II and -III pyroxenites were modeled using cpx and garnet trace element concentrations combined with experimental mineral–melt partition coefficients (D, Table 11). Partition coefficients vary with cpx and garnet composition, temperature, pressure and the water content of the melt (e.g. Wood & Blundy, 1997; Van Westrenen *et al.*, 2001; Gaetani *et al.*, 2003). The D values chosen were selected mainly from the experiments from Hart & Dunn (1993) for Type-I and -II pyroxenites to model a hot (>1300°C) primitive melt fractionating cpx, and from Green *et al.* (2000) for Type-III garnet pyroxenites, as the intermineral partition coefficients ($D_{cpx/grt}$) of Green *et al.* (2000) are similar to the $D_{cpx/grt}$ values observed in Type-III pyroxenites and differ from the anhydrous experiments of Hauri *et al.* (1994) (Appendix 7), which could indicate that the melts parental to Type-III pyroxenites were hydrous.

These calculations are straightforward to model the parental melts of Type-I and -II pyroxenites, interpreted to represent cumulates from melts that crystallized mainly cpx, opx and spinel. Type-III pyroxenites are more difficult to interpret, as they have a more pronounced metamorphic history. Nevertheless, based on our observations above, porphyroclastic magmatic garnet and cpx in Type-III pyroxenites are interpreted to have formed by fractionation from a melt under high pressure, as originally suggested by Kornprobst *et al.* (1990). Figure 20 illustrates the calculated melt compositions, which exhibit distinct trace element patterns for the different pyroxenite types.

Table 11: Cpx and garnet melt partition coefficients used in this study for Type-I and -II pyroxenites (D1), and Type III pyroxenites (D2 and D3)

	*D*1 (cpx/melt)	*D*2 (cpx/melt)	*D*3 (grt/melt)
Ba	0·00068[1]	0·0058[2]	
Th	0·012[2]	0·014[2]	
U	0·0103[2]	0·0127[2]	
Nb	0·0077[1]	0·0067[6]	
Ta	0·024[3]	0·022[6]	
La	0·0536[1]	0·057[6]	
Ce	0·0858[1]	0·12[6]	0·0029[6]
Pb	0·072[1]	0·01[2]	
Pr	0·14[4]	0·2[6]	0·0083[6]
Sr	0·1283[1]	0·066[6]	0·0023[6]
Nd	0·1873[1]	0·33[6]	0·03[6]
Hf	0·256[1]	0·31[6]	0·07[6]
Zr	0·1234[1]	0·18[6]	0·12[6]
Ti	0·384[1]	0·53[6]	0·22[6]
Sm	0·291[1]	0·58[6]	0·18[6]
Eu	0·328[5]	0·77[6]	0·33[6]
Gd	0·39[4]	0·77[6]	0·75[6]
Tb	0·42[4]	0·95[6]	1·5[6]
Dy	0·442[1]	1·1[6]	2·4[6]
Ho	0·41[4]	1·1[6]	3·7[6]
Er	0·387[1]	1·1[6]	4·4[6]
Yb	0·430[1]	1·2[6]	6·5[6]
Lu	0·433[1]	0·98[6]	6·7[6]

[1]Hart & Dunn (1993).
[2]Hauri *et al.* (1994).
[3]Nb/Ta ratio from Lundstrom *et al.* (1998).
[4]Interpolated *D* values calculated from adjacent REE.
[5]Sm/Eu ratio from Hauri *et al.* (1994).
[6]Green *et al.* (2000), run 1802 for cpx and run 1787 for garnet.

The melts calculated to be in equilibrium with cpx from Type-I Cr-diopside websterites (Fig. 20a) have LREE-enriched trace element patterns and negative HFSE anomalies relative to adjacent elements (Nb_N/La_N <1). These overall characteristics are strongly indicative of a subduction signature and support an origin of the melts parental to Type-I pyroxenites from a metasomatized mantle source. The calculated melts are similar to those of the Gourougou volcanic field lavas from the Alboran Basin (Duggen *et al.*, 2005). These Alboran Basin lavas are

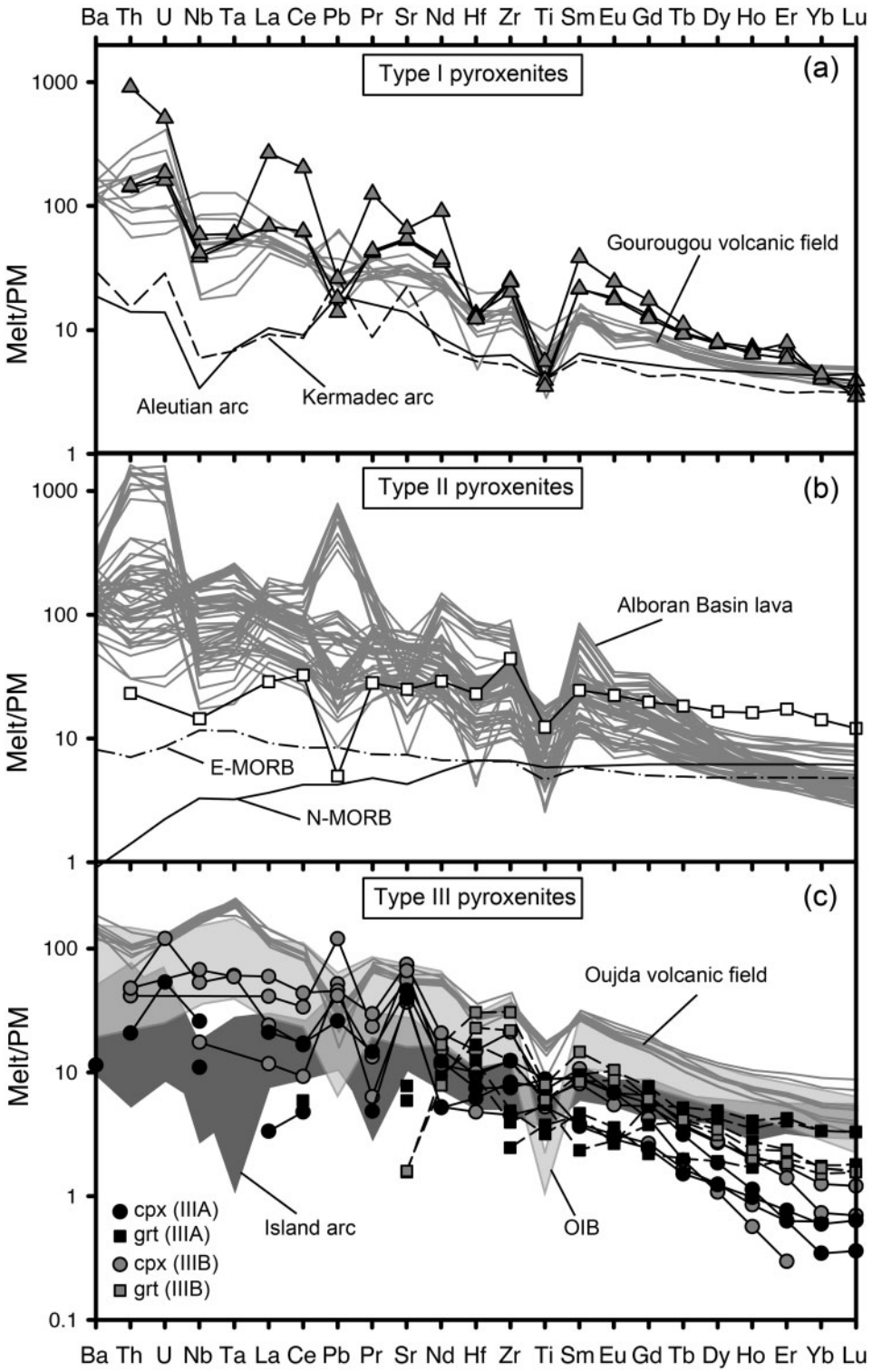

Fig. 20. Calculated melt compositions from cpx (a–c) and garnet (c) normalized to primitive mantle (McDonough & Sun, 1995). Light grey lines correspond to Alboran Basin lavas from Duggen *et al.* (2005), light grey shaded area to ocean island basalts (OIB) from Willbold & Stracke (2006) and dark grey shaded area corresponds to island arc field from Kelemen *et al.* (2003). N-MORB and E-MORB from Sun & McDonough (1989). Aleutian arc and Kermadec arc from Kelemen *et al.* (2003); Gourougou and Oujda volcanic fields from Duggen *et al.* (2005).

interpreted to be derived from a subduction-related metasomatized mantle source (Duggen *et al.*, 2005).

Melt compositions calculated to be in equilibrium with cpx from Type-II spinel websterites differ from those for the Type-I pyroxenites, and are slightly enriched in LREE and HFSE, except for Ti, which is slightly depleted. Pb shows a negative anomaly, with the overall calculated patterns intermediate between enriched (E)-MORB and Alboran Basin lavas (Fig. 20b).

Melts in equilibrium with cpx (Fig. 20c) from Type-IIIA are characterized by MREE to HREE fractionation ($Dy_N/Yb_N = 2{\cdot}1–5{\cdot}4$), slightly enriched Nb relative to La ($Nb_N/La_N = 1{\cdot}2–3{\cdot}3$), and relatively undepleted HFSE. Overall the trace element patterns of the melts calculated to be in equilibrium with garnet from the Type-IIIA pyroxenites are similar to those calculated from cpx. The melts in equilibrium with garnet are less depleted in the HREE, except for the weakly fractionated Zr relative to Ti, and slight Hf enrichment relative to Zr and Sr depletion.

Melts calculated to be in equilibrium with cpx of Type-IIIB pyroxenites (Fig. 20c) are enriched in LREE and show fractionated MREE to HREE ($Dy_N/Yb_N = 2{\cdot}0–3{\cdot}8$). Furthermore, they exhibit a slight HFSE enrichment, except that Ti is depleted, Zr is slightly enriched relative to Hf, and Nb is unfractionated to enriched relative to La ($Nb_N/La_N = 0{\cdot}9–2{\cdot}8$). Melts calculated from garnet are generally more enriched in HREE and depleted in Sr, and show HFSE patterns similar to the melts calculated from cpx.

The computed melts for Type-III pyroxenites are variably enriched in incompatible elements with Nb_N/La_N generally >1, and show MREE to HREE fractionation and an overall absence of HFSE depletion. These characteristics are different from those of island arc basalts and, therefore, the melts parental to Type-III pyroxenites cannot directly be related to a subduction setting. Their trace element patterns are instead more similar to those of intra-plate type magmas. Their overall calculated melt compositions are similar to those of the Oujda volcanic field lavas from the Alboran Basin (Duggen *et al.*, 2005). The differences between the melts calculated for Type-IIIA and -IIIB pyroxenites are mainly observed in the LREE enrichment, variations in HFSE, and in the MREE to HREE fractionation. In particular, the LREE variation may result from post-formation metasomatism by melts similar to the melts parental to Type-I pyroxenites. The strong MREE to HREE fractionation indicates that garnet played an important role during the formation and/or the evolution of the melts parental to the Type-III pyroxenites.

Melt Mg-numbers were calculated for melts in equilibrium with cpx based on the correlation of Wood & Blundy (1997) and measured X_{Mg} from cpx (Electronic Appendix 1). The Mg-numbers are highest in the parental melts of Type-I and -II pyroxenites, with calculated averages of 0·75 and 0·60, respectively. The average Mg-numbers of equilibrium melts calculated for Type-III pyroxenites are lower, with average values of 0·49 for Type-IIIA, 0·42 for the PSD and 0·60 for Type-IIIB pyroxenites. The low, non-primitive, Mg-numbers of the melts parental to Type-IIIA pyroxenites and the PSD indicate that these melts were most probably not in equilibrium with the host peridotites. The Mg-numbers of Type-IIIB parental melts are nevertheless closer to those of mantle-derived melts.

Type-I pyroxenites: pervasive melt infiltration and metasomatism

Type-I Cr-diopside websterites are primitive with high Mg-number (90·2–90·78), Cr (4100–7830 ppm) and Ni (1570–2120 ppm). Furthermore, high Cr contents in minerals such as spinel and cpx are characteristic of relatively unfractionated mantle-derived melts. Fractionated bulk LREE/HREE ratios may be interpreted in terms of low-degree partial melting of a spinel lherzolite or a moderate degree melting of a garnet lherzolite source. Cpx trace element patterns are comparable with those of metasomatized xenoliths found in Spitsbergen (Ionov *et al.*, 2002) and calculated melt compositions are similar to those of lavas erupted in the Alboran Basin (Duggen *et al.*, 2005). The characteristic HFSE depletion and LREE enrichment trends observed in the bulk-rock and cpx geochemistry both indicate an enriched, metasomatized mantle source and a subduction signature. Field observations demonstrate that Type-I pyroxenites texturally overprint the surrounding peridotites. They locally modify their host-rock chemistry, especially the bulk LREE content, most prominently in the secondary lherzolites from the pyroxenite-rich zones (see Fig. 10b). This indicates that the melt responsible for the formation of Type-I pyroxenites pervasively metasomatized the surrounding peridotites during infiltration. The low CaTs and intermediate jadeite contents, and high to unfractionated Th/U ratios of cpx indicate that Type-I pyroxenites equilibrated at relatively low pressures (<15 kbar) in the Seiland subfacies of the spinel lherzolite stability field. Type-I pyroxenites therefore record a melt infiltration stage within the Beni Bousera mantle peridotites during which porous flow led to changes in the texture and geochemistry of the host spinel lherzolites (forming secondary lherzolites).

Cr-rich bands similar to the Type-I pyroxenites have also been observed in the Ronda peridotite and have been interpreted as resulting from metasomatic replacement of previous mafic layers by reaction with volatile-rich melts percolating through the peridotites ('group D' pyroxenites; Garrido & Bodinier, 1999). Field relations in the Beni Bousera massif do not indicate that the Type-I pyroxenites replace older pyroxenite bands; rather they form networks in the otherwise pyroxenite-free host lherzolite. Type-I pyroxenite bands are more abundant and less deformed in

the Beni Bousera massif than the sometimes isoclinally folded (Garrido & Bodinier, 1999) 'group D' pyroxenites in Ronda. Furthermore, the Type-I pyroxenites are all LREE enriched. The magmatic temperatures recorded by the Type-I pyroxenites (~1350°C), their limited subsolidus re-equilibration and mostly undeformed character indicate that these pyroxenite bands are probably the youngest pyroxenite type in the massif and are younger than the Type-III garnet pyroxenites for which Re–Os model ages of 1·2–1·4 Ga have been calculated (Pearson & Nowell, 2004).

Type-II pyroxenites: melt–secondary lherzolite interaction

Type-II spinel websterites are similar to Type-I pyroxenites in terms of their high Mg-number (83·7–90·0) and high Ni (1140–2360 ppm), but have intermediate Cr contents (855–1060 ppm). Their bulk-rock and mineral Ti concentrations are higher than in Type-I pyroxenites, and most importantly, their REE patterns are only slightly enriched in LREE and close to those observed in the host peridotites. Calculated melt compositions have unfractionated primitive mantle-normalized trace element patterns with a slight enrichment of the more incompatible elements.

Pyroxenite bands similar to the Type-II pyroxenites have been described from the Ronda massif [the 'group C' pyroxenites of Garrido & Bodinier (1999)], which have characteristically high Ti contents for a given Mg-number. The 'group C' pyroxenites have been interpreted to reflect metasomatic replacement of the host peridotites by pyroxene-forming melt–rock reactions (Garrido & Bodinier, 1999; Bodinier *et al.*, 2008). In our study, the scarce occurrence of these pyroxenite bands preludes definitive conclusions on the source of these pyroxenites. Calculated melt Mg-numbers of ~0·60 and high bulk-rock and mineral Ti concentrations indicate that the melts parental to the Type-II spinel websterites were somewhat more evolved than those of the Type-I Cr-diopside websterites. The overall chemistry and the presence of amphibole in these pyroxenite bands indicates that the Type-II pyroxenite bands are not directly related to the Type-I pyroxenites that are in contrast depleted in HFSE and Ti and are very Cr-rich.

Type-III pyroxenites: high-pressure cumulates overprinted by secondary metasomatism (?)

Type-IIIA garnet clinopyroxenites and Type-IIIB kelyphite websterites have highly correlated bulk-rock major element chemistries suggesting that they are genetically linked. However, the Type-IIIB pyroxenites show some similarities to Type-IV pyroxenites; that is, variable bulk Al_2O_3 with nearly constant FeO/MgO ratios and variable CaTs in cpx. Type-IIIA pyroxenites represent the most evolved pyroxenites, as reflected in their high FeO and low Mg-number (60·9–79·8) and Ni (79–707 ppm) content. Kornprobst *et al.* (1990) termed this pyroxenite suite Type-I pyroxenites, and interpreted them as high-pressure cumulates of cpx and garnet (Kornprobst, 1969, 1970; Loubet & Allègre, 1982; Kornprobst *et al.*, 1990; Pearson *et al.*, 1991, 1993). Their bulk-rock and mineral HREE enrichment is consistent with the accumulation of garnet at high pressure and is similar to that of the garnet-bearing pyroxenites investigated by Pearson *et al.* (1993). Furthermore, the isotope systematics of these garnet pyroxenites, some containing graphite pseudomorphs after diamond, indicates that the formation of their parental melts involved hydrothermally altered oceanic crust (Pearson *et al.* 1991, 1993); nevertheless, the calculated parental melts lack clear subduction-related trace element signatures (Fig. 20). Because of the low Mg-number of the parental melts, these pyroxenites probably crystallized in a regime where melt flow was channeled and chemically isolated from the host peridotite. Our observations demonstrate that Type-III pyroxenites were emplaced and re-equilibrated over a broad range of pressures (see Fig. 18) from >45 kbar to 20–30 kbar, and therefore record an overall complex history. This is also apparent in the large variations in cpx and calculated melt LREE patterns. The pronounced LREE variations in Type-III pyroxenites may be ascribed to the REE partitioning behavior between cpx, grt and melt at high pressure under hydrous conditions (e.g. Green *et al.*, 2000; Gaetani *et al.*, 2003), to mantle metasomatism (e.g. Ionov *et al.*, 2002; Scambelluri *et al.*, 2006) or owing to the heterogeneous nature of the source of their parental melts (Pearson *et al.*, 1991, 1993).

Type-IV pyroxenites: delaminated metamorphosed gabbros

Type-IV garnet metagabbros are Al_2O_3 and Na_2O rich with high Mg-number (81·9–83·9). Their bulk-rock compositions and REE patterns are similar to the Type-II garnet clinopyroxenites of Kornprobst *et al.* (1990), interpreted to represent gabbroic oceanic crust that has been recycled back into the mantle. Some of the Type-IV pyroxenites resemble the peraluminous eclogites and grospydites present as xenoliths in kimberlites (Kornprobst *et al.*, 1987, 1990). The positive Eu and Sr anomalies in their bulk-rock compositions, coupled with elevated Na_2O contents, indicate a magmatic plagioclase signature. In fact, relict plagioclase in sample B45 with a high Sr content (1430 ppm) suggests that it is a primary phase. The plagioclase trace element signature is imprinted on metamorphic garnet and cpx, both characterized by HREE depletion and positive Eu (Eu_N/Eu^*_N) anomalies (Figs 15–17). Partly, cpx have high CaTs concentrations related to this prograde metamorphic overprint. Spinels are hercynitic, and their high Al contents formed through prograde metamorphism, which might also produce corundum and sapphirine in appropriate Al-rich bulk compositions [see reaction (2)] as described in boulders from the Oued

Mejahedid and Oued Amasiene riverbeds by Kornprobst *et al.* (1990).

Some samples (e.g. B46-3) have opx preserved and plagioclase absent, whereas others (e.g. B45) have opx absent and plagioclase preserved. We interpret this relationship with respect to reaction (3) and speculate that sample B46-3 originally had higher modal ratios of opx/plag compared with sample B45, in accordance with the higher bulk-rock MgO concentration in the former (Table 2). This evidence for the prograde formation of garnet and cpx as a result of reaction (3) indicates that the magmatic protolith of Type-IV pyroxenites originated from <10 kbar pressure (Fig. 18). The preservation of magmatic plagioclase in sample B45 indicates that the prograde metamorphism of these rocks never reached eclogite-facies conditions.

The history of the Type-IV pyroxenites thus differs significantly from the rest of the massif. Based on radiogenic isotope and REE whole-rock data, these rocks have been interpreted as stretched and thinned subducted oceanic crust remnants in a 'marble cake' mantle (Allègre & Turcotte, 1986; Kornprobst *et al.*, 1990). The preserved magmatic and metamorphic phase assemblages, however, are inconsistent with this interpretation. Our calculated low temperatures (800–980°C) and relatively lower pressures (~14 kbar), in conjunction with primary plagioclase, suggest that the prograde metamorphism of these gabbroic garnet pyroxenites was associated with a pressure increase but did not reach the depths of the garnet–spinel transition in peridotites. Rather than having already been part of a 'marble cake' mantle, the Type-IV pyroxenites were still at a 'pre-marble cake' stage; that is, they had already been introduced into the mantle but not entrained into the larger-scale mantle convection. Our extended trace element dataset allows us to clarify the origin of these rocks. Type-IV pyroxenites have pronounced negative Nb and Ta anomalies compared with neighboring elements of similar incompatibility ($Nb_N/La_N \sim 0{\cdot}10$) and positive Pb and Sr anomalies, pointing towards a supra-subduction, but not an oceanic crust setting for the formation of the Type-IV metagabbros. In the following discussion, we illustrate the similarities between the Type-IV pyroxenites and the lower crustal section of the Kohistan paleo-arc (northern Pakistan).

Comparison with the deep Kohistan arc crust

In Fig. 21, we compare the trace elements concentrations of Type-IV pyroxenites and Beni Bousera mafic–ultramafic rocks with those of other alpine-type massifs, with lower crustal gabbros from a slow-spreading mid-ocean ridge (Hart *et al.*, 1999; Bach *et al.*, 2001), and with the lower crustal sequence from the Chilas and the Southern Plutonic Complex in the Kohistan arc, northern Pakistan (Jagoutz *et al.*, 2007, 2011). The Kohistan arc constitutes the only known place where the deepest parts (>50 km) of a paleo-arc, including mafic and ultramafic cumulates, are fully exposed. The Kohistan Southern Plutonic Complex reflects a cumulate sequence of hydrous, mantle-derived melts evolving through medium- to high-pressure fractionation, whereas the Chilas Complex is formed from significantly drier parental melts. Calculated densities, based on computed phase diagrams, reveal that cumulates derived from hydrous fractionation have a stronger tendency to delaminate than those from drier sequences (Jagoutz *et al.*, 2011). The bulk-rock trace element compositions of Type-IV pyroxenites are similar to those of cumulative pyroxenites and lower crustal gabbros from the more hydrous fractionation series of the Kohistan arc, but differ strongly from mid-ocean ridge (MOR) sequences or the almost dry Chilas Complex (Fig. 21). The similarity between the Type-IV pyroxenites and the rocks from the Southern Plutonic Complex is also apparent from their calculated modal compositions (Fig. 22). Type-IV pyroxenites have lower plagioclase contents and are quartz negative, similar to mafic rocks from the more hydrous Kohistan sequence but in contrast to the dry Kohistan series and to MOR and ophiolitic gabbros. In turn, MOR gabbros and the Chilas complex have strikingly different major and trace element compositions that differ from the rocks found in Beni Bousera; only some of the 'group A' mafic rocks described from Ronda (Garrido & Bodinier, 1999) have some resemblance to the drier fractionation sequence (Fig. 21) and plot close to MOR and ophiolitic gabbros (Fig. 22). In some of the Kohistan pyroxenites from the Southern Plutonic Complex, plagioclase is a magmatic phase, becoming abundant in the lower crustal gabbros (Jagoutz *et al.*, 2011). Accordingly, a prograde metamorphic pressure increase results in an alternative interpretation for the genesis of Type-IV pyroxenites. Type-IV rocks may represent delaminated lower arc crust. To achieve such delamination or lower crust foundering, it is necessary that these metagabbros become denser than the mantle. We used Perple_X (Connolly, 2005) to calculate the average density of Type-IV pyroxenites and Beni Bousera peridotites at the quartz–fayalite–magnetite (QFM) buffer. At pressures <10 kbar, Type-IV rocks are positively buoyant and ~100 kg m^{-3} less dense than average Beni Bousera spinel lherzolites at similar P–T conditions. At pressures >10 kbar, Type-IV pyroxenites undergo metamorphic densification as a result of reaction (3) and become negatively buoyant and ~100 kg m^{-3} denser than the peridotites. To our knowledge, the Type-IV pyroxenites are the first direct evidence for delamination of lower continental crust into the upper mantle.

P–T model and pyroxenite petrogenesis

Results from the geothermobarometry calculations and field observations indicate that the Beni Bousera mantle slice has been infiltrated during its ascent by various melts

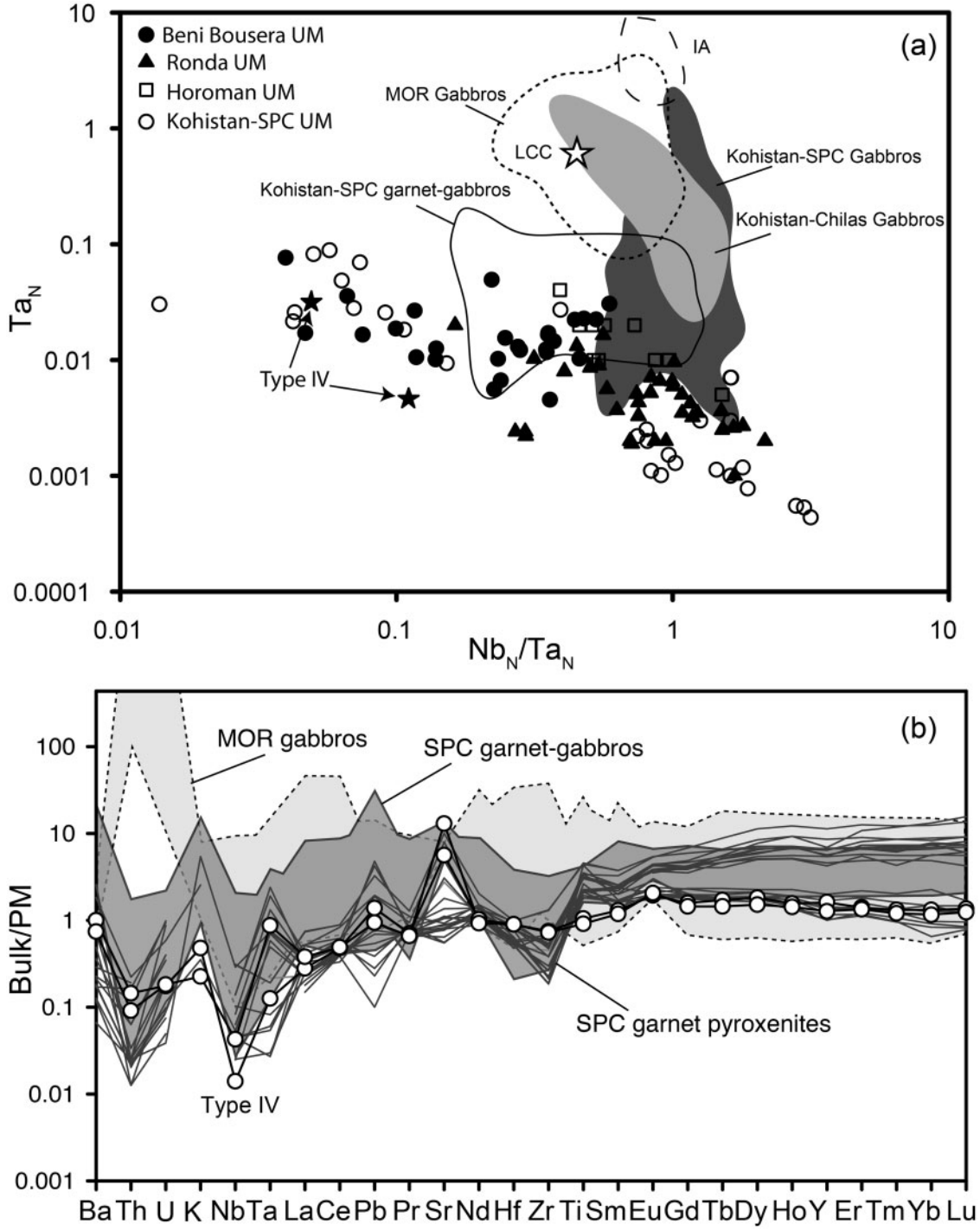

Fig. 21. (a) Ta_N vs Nb_N/Ta_N normalized to primitive mantle (McDonough & Sun, 1995) of Beni Bousera mafic–ultramafic rocks and Type-IV pyroxenites compared with Ronda (Garrido & Bodinier, 1999), Horoman (Malaviarachchi *et al.*, 2010), the Kohistan Soutern Plutonic Complex (SPC) and Chilas Complex (Jagoutz *et al.*, 2006, 2011), MOR gabbros (Hart *et al.*, 1999; Bach *et al.*, 2001), bulk lower continental crust (LCC) (Rudnick & Gao, 2003) and island arcs (IA) (Pearce *et al.*, 2005). Type-IV pyroxenites and Beni Bousera mafic–ultramafic rocks show a strong Nb/Ta fractionation. (b) Bulk-rock trace element patterns of Type-IV pyroxenites from Beni Bousera, the moderately hydrous fractionation trend of the Southern Plutonic Complex (SPC) of the Kohistan paleo-arc (Dhuime *et al.*, 2007; Jagoutz *et al.*, 2011) and from MOR gabbros (Hart *et al.*, 1999).

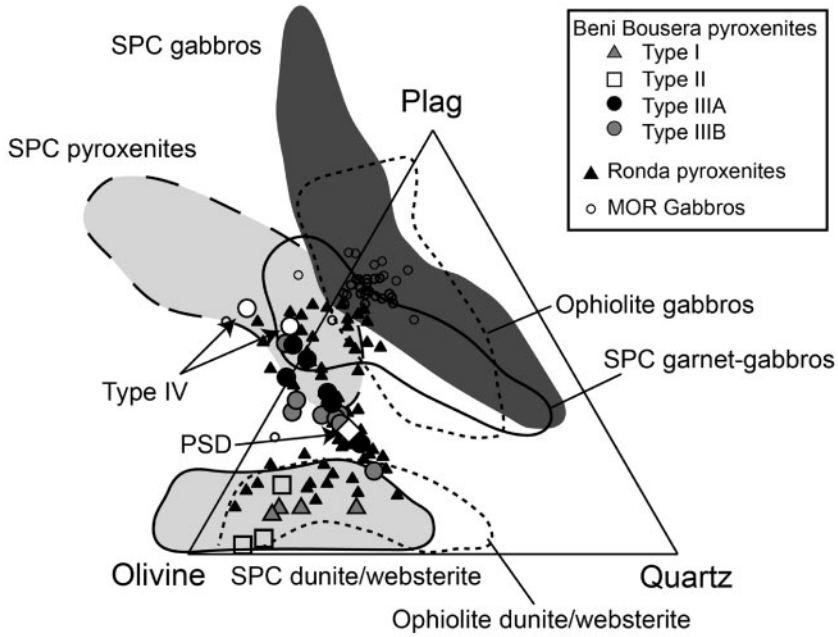

Fig. 22. Basalt tetrahedron projected from cpx comparing Beni Bousera pyroxenites with Ronda pyroxenites (Garrido & Bodinier, 1999), the lower section of the Kohistan arc Southern Plutonic Complex (SPC) (Dhuime *et al.*, 2007; Jagoutz *et al.*, 2011), MOR gabbros (Hart *et al.*, 1999) and Oman ophiolite gabbros–pyroxenites (Goodenough *et al.*, 2010). Projection from the cpx apex onto the plag–ol–qtz plane using the projection scheme of Grove (1993).

leading to the formation of diverse suites of pyroxenites at various P and T conditions. The cooling conditions recorded by most of the pyroxenites fit into a multi-stage emplacement model for the massif, somewhat similar to what has been proposed for the Ronda massif (Van der Wal & Vissers, 1993). Figure 18 shows the P–T conditions recorded in the Type-I to -IV pyroxenites. Initially, Type-IIIA pyroxenites containing graphite pseudomorphs after diamond and originating from >45 kbar, were emplaced during stage 1. Either the melts crystallized close to the diamond–graphite transition (path 1a), or they migrated to shallower levels at ~35 kbar (path 1b) as recorded in the recrystallized garnet–opx neoblasts in the PSD (~35 kbar). The melts parental to Type-III pyroxenites intruded or infiltrated the peridotites at polybaric conditions with pressures of >20~30 kbar during stage 2, the Type-III pyroxenites preserving only near-solidus or subsolidus cooling temperatures of ~900–1250°C. Next, Type-IV pyroxenites, representing supra-subduction zone gabbroic crust, were delaminated (stage 3), and emplaced into the Beni Bousera mantle accompanied by prograde metamorphism to ~800–980°C and ~14 kbar. A major heating event (stage 4) to >1200°C and 11–15 kbar led to the infiltration of the melts parental to the Type-I pyroxenites overprinting the primary lherzolites in the central part of the massif at conditions of the transition between ariegite and Seiland subfacies. The Type-II pyroxenites may represent the product of melt–peridotite interaction before and/or during the infiltration of the parental melts to the Type-I pyroxenites; however, the Type-I and -II pyroxenites were not formed from the same parental melts. The LREE variations recorded in the secondary lherzolites, as well as the Type-IIIB pyroxenites, indicate that the melts parental to the Type-I pyroxenites acted as their metasomatic agent. Nevertheless, we cannot exclude the possibility that Type-IIIB pyroxenites were subject to secondary metasomatism at earlier stages. It is not yet clear what the source of the parental melts of the Type-I pyroxenites is, but they are clearly primitive. Carbonate-rich melts were suggested to be involved in the petrogenesis of pyroxenites from Spitsbergen with a similar geochemistry (Ionov *et al.*, 2002). Nevertheless, there is no direct indication of carbonate melt involvement in the Beni Bousera Type-I pyroxenites. Type-I pyroxenites record the last melt infiltration during the mantle stage of the Beni Bousera massif.

CONCLUSIONS

We have presented a study that combines field, microtextural, mineralogical and geochemical data based on a detailed investigation of two mantle reaction zones in the valley of Sidi Yahia Aârab in the Beni Bousera massif. The main goal was first to identity the various groups of pyroxenites and second to unravel their origins and P–T paths. Our results show that melt infiltrations concentrate in pyroxenite-rich zones affecting the primary lherzolites by

changing their texture. Pyroxenites originating from melts derived from various sources and depths occur in the same pyroxenite-rich zones and record different stages during the history of the Beni Bousera mantle body. Type-III garnet pyroxenites originated from high-pressure fractionation of dominantly garnet and cpx. Their formation requires channelled melt flow as they are far from equilibrium with their host peridotite. Type-III garnet pyroxenites are in part secondarily metasomatized, possibly during cooling and/or exhumation. Type-IV garnet metagabbros come closest to but do not reach melt compositions and were formed in the lower part of an arc crust and then mechanically delaminated. After the Type-IV garnet metagabbros, the Type-II and Type-III pyroxenites were emplaced and Type-I Cr-diopside websterite melts infiltrated pervasively, metasomatizing the surrounding peridotites and eventually the pre-existing pyroxenites, during a major heating event. All the pyroxenites are cumulates, but only Type-I to -III formed from melts infiltrating the surrounding mantle. Infiltrations such as Type-I pyroxenites reflect metasomatic processes characteristic of large mantle domains and can account for the trace element characteristics of the lavas erupted in the Alboran Basin.

ACKNOWLEDGEMENTS

We would like to thank Adélie Delacour, Andreas Enggist, Eric Reusser, Lydia Zehnder, Marcel Guillong, Peter Ulmer and Pierre Bouilhol for assistance with XRF, EMPA and LA-ICP-MS analysis. Peter Nievergelt provided help and useful comments on thin section photomicrographs as well as on the field profiles and geological map. Nicole Hurtig is thanked for comments and discussions. The families in Bou Ahmed are thanked for their hospitality and guidance in the Rif mountains. We gratefully acknowledge reviews by Graham Pearson and Masaaki Obata, and editorial comments by Marjorie Wilson.

FUNDING

This project was supported by the Grubenmann foundation of ETH Zurich, and by NSF grant EAR-0910644 to O.J.

SUPPLEMENTARY DATA

Supplementary data for this paper are available at *Journal of Petrology* online.

REFERENCES

Allègre, C. J. & Turcotte, D. L. (1986). Implications of a 2-component marble-cake mantle. *Nature* **323**, 123–127.

Bach, W., Alt, J. C., Niu, Y., Humphris, S. E., Erzinger, J. & Dick, H. J. B. (2001). The chemical consequences of late-stage hydrothermal circulation in an uplifted block of lower ocean crust at the Southwest Indian Ridge: results from ODP Hole 735B (Leg 176). *Geochimica et Cosmochimica Acta* **65**, 3267–3287.

Barnes, S. J. & Roeder, P. L. (2001). The range of spinel compositions in terrestrial mafic and ultramafic rocks. *Journal of Petrology* **42**, 2279–2302.

Blichert-Toft, J., Albarède, F. & Kornprobst, J. (1999). Lu–Hf isotope systematics of garnet pyroxenites from Beni Bousera, Morocco: Implications for basalt origin. *Science* **283**, 1303–1306.

Bodinier, J. L., Garrido, C. J., Chanefo, I., Bruguier, O. & Gervilla, F. (2008). Origin of pyroxenite–peridotite veined mantle by refertilization reactions: Evidence from the Ronda peridotite (Southern Spain). *Journal of Petrology* **49**, 999–1025.

Brey, G. P. & Köhler, T. (1990). Geothermobarometry in four-phase lherzolites II. New thermobarometers, and practical assessment of existing thermobarometers. *Journal of Petrology* **31**, 1353–1378.

Cawthorn, R. G. & Collerson, K. D. (1974). Recalculation of pyroxene end-member parameters and estimation of ferrous and ferric iron content from electron-microprobe analyses. *American Mineralogist* **59**, 1203–1208.

Chalouan, A. & Michard, A. (2004). The Alpine Rif belt (Morocco): A case of mountain building in a subduction–subduction–transform fault triple junction. *Pure and Applied Geophysics* **161**, 489–519.

Chalouan, A., Michard, A., Feinberg, H., Montigny, R. A. & Saddiqi, O. (2001). The Rif mountain building (Morocco): A new tectonic scenario. *Bulletin de la Société Géologique de France* **172**, 603–616.

Connolly, J. A. D. (2005). Computation of phase equilibria by linear programming: a tool for geodynamic modeling and its application to subduction zone decarbonation. *Earth and Planetary Science Letters* **236**, 524–541.

Davies, G. R., Nixon, P. H., Pearson, D. G. & Obata, M. (1993). Tectonic implications of graphitized diamonds from the Ronda peridotite massif, southern Spain. *Geology* **21**, 471–474.

Dhuime, B., Bosch, D., Bodinier, J. L., Garrido, C. J., Bruguier, O., Hussain, S. S. & Dawood, H. (2007). Multistage evolution of the Jijal ultramafic–mafic complex (Kohistan, northern Pakistan): Implications for building the roots of island arcs. *Earth and Planetary Science Letters* **261**, 179–200.

Dickey, J. S. (1970). Partial fusion products in alpine type peridotites: Serrania de la Ronda and other examples. In: Morgan, B. A. (ed.) *Fiftieth Anniversary Symposia, Mineralogy and Petrology of the Upper Mantle. Mineralogical Society of America, Special Papers* **3**, 33–49.

Draoui, M. (1992). Étude pétro-structurale du massif ultrabasique de Beni Bousera (Rif interne, Maroc): Un modèle de mise en place, PhD Thesis, University of Cadi Ayad, Marrakesh.

Duggen, S., Hoernle, K., Van den Bogaard, P. & Garbe-Schonberg, D. (2005). Post-collisional transition from subduction- to intraplate-type magmatism in the westernmost Mediterranean: Evidence for continental-edge delamination of subcontinental lithosphere. *Journal of Petrology* **46**, 1155–1201.

Ellis, D. J. & Green, D. H. (1979). Experimental-study of the effect of Ca upon garnet–clinopyroxene Fe–Mg exchange equilibria. *Contributions to Mineralogy and Petrology* **71**, 13–22.

Foley, S., Tiepolo, M. & Vannucci, R. (2002). Growth of early continental crust controlled by melting of amphibolite in subduction zones. *Nature* **417**, 837–840.

Frey, F. A., Suen, C. J. & Stockman, H. W. (1985). The Ronda high temperature peridotite: Geochemistry and petrogenesis. *Geochimica et Cosmochimica Acta* **49**, 2469–2491.

Fulmer, E. C., Nebel, O. & Van Westrenen, W. (2010). High-precision high field strength element partitioning between garnet, amphibole and alkaline melt from Kakanui, New Zealand. *Geochimica et Cosmochimica Acta* **74**, 2741–2759.

Gaetani, G. A., Kent, A. J. R., Grove, T. L., Hutcheon, I. D. & Stolper, E. M. (2003). Mineral/melt partitioning of trace elements during hydrous peridotite partial melting. *Contributions to Mineralogy and Petrology* **145**, 391–405.

Garrido, C. J. & Bodinier, J. L. (1999). Diversity of mafic rocks in the Ronda peridotite: Evidence for pervasive melt–rock reaction during heating of subcontinental lithosphere by upwelling asthenosphere. *Journal of Petrology* **40**, 729–754.

Garrido, C. J., Bodinier, J. L. & Alard, O. (2000). Incompatible trace element partitioning and residence in anhydrous spinel peridotites and websterites from the Ronda orogenic peridotite. *Earth and Planetary Science Letters* **181**, 341–358.

Godard, M., Lagabrielle, Y., Alard, O. & Harvey, J. (2008). Geochemistry of the highly depleted peridotites drilled at ODP Sites 1272 and 1274 (Fifteen-Twenty Fracture Zone, Mid-Atlantic Ridge): Implications for mantle dynamics beneath a slow spreading ridge. *Earth and Planetary Science Letters* **267**, 410–425.

Goodenough, K. M., Styles, M. T., Schofield, D., Thomas, R. J., Crowley, Q. C., Lilly, R. M., McKervey, J., Stephenson, D. & Carney, J. N. (2010). Architecture of the Oman–UAE ophiolite: evidence for a multi-phase magmatic history. *Arabian Journal of Geosciences* **4**, 439–458.

Green, T. H., Blundy, J. D., Adam, J. & Yaxley, G. M. (2000). SIMS determination of trace element partition coefficients between garnet, clinopyroxene and hydrous basaltic liquids at 2–7·5 GPa and 1080–1200°C. *Lithos* **53**, 165–187.

Grove, T. L. (1993). Corrections to expressions for calculating mineral components in 'Origin of calc-alkaline series lavas at Medicine Lake volcano by fractionation, assimilation and mixing' and 'Experimental petrology of normal MORB near the Kane Fracture Zone: 22°–25°N, Mid-Atlantic Ridge'. *Contributions to Mineralogy and Petrology* **114**, 422–424.

Guillong, M., Meier, D. L., Allan, M. M., Heinrich, C. A. & Yardley, B. W. D. (2008). SILLS: A Matlab-based program for the reduction of laser ablation ICP-MS data of homogeneous materials and inclusions. In: Sylvester, P. (ed.) *Laser Ablation ICP-MS in the Earth Sciences: Current Practices and Outstanding Issues. Mineralogical Association of Canada, Short Course Series* **40**, 328–333.

Hamelin, B. & Allègre, J. (1988). Lead isotope study of orogenic lherzolite massifs. *Earth and Planetary Science Letters* **91**, 117–131.

Hart, R. H. & Dunn, T. (1993). Experimental cpx/melt partitioning of 24 trace elements. *Contributions to Mineralogy and Petrology* **113**, 1–8.

Hart, S. R., Blusztajn, J., Dick, H. J. B., Meyer, P. S. & Muehlenbachs, K. (1999). The fingerprint of seawater circulation in a 500-meter section of ocean crust gabbros. *Geochimica et Cosmochimica Acta* **63**, 4059–4080.

Harte, B. & Kirkley, M. B. (1997). Partitioning of trace elements between clinopyroxene and garnet: data from mantle eclogites. *Chemical Geology* **136**, 1–24.

Hauri, E. H., Wagner, T. P. & Grove, T. L. (1994). Experimental and natural partitioning of Th, U, Pb and other trace-elements between garnet, clinopyroxene and basaltic melts. *Chemical Geology* **117**, 149–166.

Hellebrand, E., Snow, J. E., Mostefaoui, S. & Hoppe, P. (2005). Trace element distribution between orthopyroxene and clinopyroxene in peridotites from the Gakkel Ridge: A SIMS and nanoSIMS study. *Contributions to Mineralogy and Petrology* **150**, 486–504.

Hirschmann, M. M. & Stolper, E. M. (1996). A possible role for garnet pyroxenite in the origin of the 'garnet signature' in MORB. *Contributions to Mineralogy and Petrology* **124**, 185–208.

Ionov, D. A., Savoyant, L. & Dupuy, C. (1992). Application of the ICP-MS technique to trace-element analysis of peridotites and their minerals. *Geostandards Newsletter* **16**, 311–315.

Ionov, D. A., Bodinier, J. L., Mukasa, S. B. & Zanetti, A. (2002). Mechanisms and sources of mantle metasomatism: Major and trace element compositions of peridotite xenoliths from Spitsbergen in the context of numerical modeling. *Journal of Petrology* **43**, 2219–2259.

Jagoutz, O. (2010). Construction of the granitoid crust of an island arc part II: a quantitative petrogenetic model. *Contributions to Mineralogy and Petrology* **160**, 359–381.

Jagoutz, O., Müntener, O., Burg, J.-P., Ulmer, P. & Jagoutz, E. (2006). Lower continental crust formation through focused flow in km-scale melt conduits: The zoned ultramafic bodies of the Chilas Complex in Kohistan Island arc (NW Pakistan). *Earth and Planetary Science Letters* **242**, 320–342.

Jagoutz, O., Müntener, O., Ulmer, P., Pettke, T., Burg, J.-P., Dawood, H. & Hussain, S. (2007). Petrology and mineral chemistry of lower crustal intrusions: the Chilas Complex, Kohistan (NW Pakistan). *Journal of Petrology* **48**, 1895–1953.

Jagoutz, O., Müntener, O., Schmidt, M. W. & Burg, J.-P. (2011). The roles of flux- and decompression melting and their respective fractionation lines for continental crust formation: Evidence from the Kohistan arc. *Earth and Planetary Science Letters* **303**, 25–36.

Jochum, K. P., Seufert, H. M. & Thirlwall, M. F. (1990). High-sensitivity Nb analysis by spark-source mass spectrometry (SSMS) and calibration of XRF Nb and Zr. *Chemical Geology* **81**, 1–16.

Kelemen, P. B. (1990). Reaction between ultramafic rock and fractionating basaltic magma I. Phase relations, the origin of calc-alkaline magma series, and the formation of discordant dunite. *Journal of Petrology* **31**, 51–98.

Kelemen, P. B., Shimizu, N. & Dunn, T. (1993). Relative depletion of niobium in some arc magmas and the continental crust: partitioning of K, Nb, La and Ce during melt/rock reaction in the upper mantle. *Earth and Planetary Science Letters* **120**, 111–134.

Kelemen, P. B., Shimizu, N. & Salters, V. J. M. (1995). Extraction of mid-ocean-ridge basalt from the upwelling mantle by focused flow of melt in dunite channels. *Nature* **375**, 747–753.

Kelemen, P. B., Hanghoj, K. & Greene, A. R. (2003). One view of the geochemistry of subduction-related magmatic arcs, with an emphasis on primitive andesite and lower crust. In: Rudnick, R. L. (ed.) *The Crust. Treatise on Geochemistry.* Oxford: Elsevier-Pergamon, pp. 593–659.

Kennedy, C. S. & Kennedy, G. C. (1976). The equilibrium boundary between graphite and diamond. *Journal of Geophysical Research* **81**, 2467–2470.

Klimm, K., Blundy, J. D. & Green, T. H. (2008). Trace element partitioning and accessory phase saturation during H_2O-saturated melting of basalt with implications for subduction zone chemical fluxes. *Journal of Petrology* **49**, 523–553.

Kornprobst, J. (1969). Le massif ultrabasique de Beni Bousera (Rif interne, Maroc): Étude des péridotites de haute température et de haute pression, et des pyroxénolites, à grenat ou sans grenat, qui leur sont associées. *Contributions to Mineralogy and Petrology* **23**, 283–322.

Kornprobst, J. (1970). Peridotites and pyroxenites from Beni Bousera (Morocco)—experimental investigation between 1100 and 1550°C from 15 to 30 kilobar dry pressure. *Contributions to Mineralogy and Petrology* **29**, 290–309.

Kornprobst, J., Piboule, M. & Tabit, A. (1987). Diversité des clinopyroxénites à grenat associées aux massifs ultramafiques orogéniques: éclogites, ariégites, griquaites et grospydites; une discussion. *Bulletin de la Société Géologique de France* **8(III)**, 345–351.

Kornprobst, J., Piboule, M., Roden, M. & Tabit, A. (1990). Corundum-bearing garnet clinopyroxenites at Beni Bousera (Morocco): Original plagioclase-rich gabbros recrystallized at depth within the mantle. *Journal of Petrology* **31**, 717–745.

Kornprobst, J., Tabit, A., Targuisti, K., Draoui, M. & Woodland, A. B. (1995). *A field trip guide for the 2nd international workshop on lherzolites and mantle processes*. Granada, Spain, pp. 1–50.

Kumar, N., Reisberg, L. & Zindler, A. (1996). A major and trace element and strontium, neodymium, and osmium isotopic study of a thick pyroxenite layer from the Beni Bousera ultramafic complex of northern Morocco. *Geochimica et Cosmochimica Acta* **60**, 1429–1444.

Kushiro, I. & Yoder, J. R. (1966). Anorthite–forsterite and anorthite–enstatite reactions and their bearing on the basalt–eclogite transformation. *Journal of Petrology* **7**, 337–362.

Landwehr, D., Blundy, J., Chamorro-Perez, E. M., Hill, E. & Wood, B. (2001). U-series disequilibria generated by partial melting of spinel lherzolite. *Earth and Planetary Science Letters* **188**, 329–348.

Lenoir, X., Garrido, C. J., Bodinier, J. L., Dautria, J. M. & Gervilla, F. (2001). The recrystallization front of the Ronda peridotite: Evidence for melting and thermal erosion of subcontinental lithospheric mantle beneath the Alboran Basin. *Journal of Petrology* **42**, 141–158.

Longerich, H. P., Jackson, S. E. & Gunther, D. (1996). Laser ablation inductively coupled plasma mass spectrometric transient signal data acquisition and analyte concentration calculation. *Journal of Analytical Atomic Spectrometry* **11**, 899–904.

Longhi, J. & Bertka, C. M. (1996). Graphical analysis of pigeonite–augite liquidus equilibria. *American Mineralogist* **81**, 685–695.

Loomis, T. P. (1972). Diapiric emplacement of Ronda high-temperature ultramafic intrusion, southern Spain. *Geological Society of America Bulletin* **83**, 2475–2496.

Loubet, M. & Allègre, C. J. (1982). Trace-elements in orogenic lherzolites reveal the complex history of the upper mantle. *Nature* **298**, 809–814.

Lundstrom, C. C., Shaw, H. F., Ryerson, F. J., Williams, Q. & Gill, J. (1998). Crystal chemical control of clinopyroxene–melt partitioning in the Di–Ab–An system: Implications for elemental fractionations in the depleted mantle. *Geochimica et Cosmochimica Acta* **62**, 2849–2862.

Malaviarachchi, S. P. K., Makishima, A. & Nakamura, E. (2010). Melt–peridotite reactions and fluid metasomatism in the upper mantle, revealed from the geochemistry of peridotite and gabbro from the Horoman peridotite massif, Japan. *Journal of Petrology* **51**, 1417–1445.

McDonough, W. F. & Sun, S.-S. (1995). The composition of the Earth. *Chemical Geology* **120**, 223–253.

McNeill, J. C. R., Pearson, D. G., Klein-BenDavid, O., Nowell, G. M., Ottley, C. J. & Chinn, I. (2009). Quantitative analysis of trace element concentrations in some gem-quality diamonds. *Journal of Physics: Condensed Matter* **21**, 1–13.

Michard, A., Chalouan, A., Feinberg, H., Goffe, B. & Montigny, R. (2002). How does the Alpine belt end between Spain and Morocco? *Bulletin de la Société Géologique de France* **173**, 3–15.

Morishita, T., Arai, S. & Gervilla, F. (2001). High-pressure aluminous mafic rocks from the Ronda peridotite massif, southern Spain: Significance of sapphirine- and corundum-bearing mineral assemblages. *Lithos* **57**, 143–161.

Morse, S. A. (1975). Plagioclase lamellae in hypersthene, Tikkoatokhakh Bay, Labrador. *Earth and Planetary Science Letters* **26**, 331–336.

Nakamura, D. (2009). A new formulation of garnet–clinopyroxene geothermometer based on accumulation and statistical analysis of a large experimental data set. *Journal of Metamorphic Geology* **27**, 495–508.

Nickel, K. G. & Green, D. H. (1985). Empirical geothermobarometry for garnet peridotites and implications for the nature of the lithosphere, kimberlites and diamonds. *Earth and Planetary Science Letters* **73**, 158–170.

Nimis, P. & Grütter, H. (2010). Internally consistent geothermometers for garnet peridotites and pyroxenites. *Contributions to Mineralogy and Petrology* **159**, 411–427.

Obata, M. (1980). The Ronda peridotite: garnet-, spinel-, and plagioclase-lherzolite facies and the P–T trajectories of a high-temperature mantle intrusion. *Journal of Petrology* **21**, 533–572.

O'Hara, M. (1968). The bearing of phase equilibria studies in synthetic and natural systems on the origin and evolution of basic and ultrabasic rocks. *Earth-Science Reviews* **4**, 69–133.

Pearce, J. A., Stern, R. J., Bloomer, S. H. & Fryer, P. (2005). Geochemical mapping of the Mariana arc–basin system: Implications for the nature and distribution of subduction components. *Geochemistry, Geophysics, Geosystems* **6**, Q07006.

Pearson, D. G. & Nowell, G. M. (2004). Re–Os and Lu–Hf isotope constraints on the origin and age of pyroxenites from the Beni Bousera peridotite massif: implications for mixed peridotite–pyroxenite mantle sources. *Journal of Petrology* **45**, 439–455.

Pearson, D. G., Davies, G. R., Nixon, P. H. & Milledge, H. J. (1989). Graphitized diamonds from a peridotite massif in Morocco and implications for anomalous diamond occurrences. *Nature* **338**, 60–62.

Pearson, D. G., Davies, G. R., Nixon, P. H., Greenwood, P. B. & Mattey, D. P. (1991). Oxygen isotope evidence for the origin of pyroxenites in the Beni Bousera peridotite massif, North Morocco: derivation from subducted oceanic lithosphere. *Earth and Planetary Science Letters* **102**, 289–301.

Pearson, D. G., Davies, G. R. & Nixon, P. H. (1993). Geochemical constraints on the petrogenesis of diamond facies pyroxenites from the Beni Bousera peridotite massif, North Morocco. *Journal of Petrology* **34**, 125–172.

Putirka, K. D. (2008). Thermometers and barometers for volcanic systems. In: Putirka, K. D. & Tepley, F. J., III (eds) *Minerals, Inclusions and Volcanic Processes. Mineralogical Society of America and Geochemical Society, Reviews in Mineralogy and Geochemistry* **69**, 61–120.

Rampone, E., Bottazzi, P. & Ottolini, L. (1991). Complementary Ti and Zr anomalies in orthopyroxene and clinopyroxene from mantle peridotites. *Nature* **354**, 518–520.

Reisberg, L., Zindler, A. & Jagoutz, E. (1989). Further Sr and Nd isotopic results from peridotites of the Ronda ultramafic complex. *Earth and Planetary Science Letters* **96**, 161–180.

Rudnick, R. L. & Gao, S. (2003). The composition of the continental crust. In: Rudnick, R. L. (ed.) *The Crust. Treatise on Geochemistry*. Oxford: Elsevier, pp. 1–64.

Rudnick, R. L. & Nyblade, A. A. (1999). The thickness and heat production of Archean lithosphere: constraints from xenoliths thermobarometry and surface heat flow. In: Fei, Y., Bertka, C. & Mysen, B. O. (eds) *Mantle Petrology: Field Observations and High Pressure Experimentation. Geochemical Society Special Publication* **6**, 3–12.

Scambelluri, M., Hermann, J., Morten, L. & Rampone, E. (2006). Melt- versus fluid-induced metasomatism in spinel to garnet wedge peridotites (Ulten Zone, Eastern Italian Alps): clues from trace element and Li abundances. *Contributions to Mineralogy and Petrology* **151**, 372–394.

Schwandt, C. S. & McKay, G. A. (1998). Rare earth element partition coefficients from enstatite/melt synthesis experiments. *Geochimica et Cosmochimica Acta* **62**, 2845–2848.

Slodkevitch, V. V. (1983). Graphite paramorphs after diamond. *Taylor & Francis, International Geology Review* **25**, 497–514.

Suen, C. J. & Frey, F. A. (1987). Origins of the mafic and ultramafic rocks in the Ronda peridotite. *Earth and Planetary Science Letters* **85**, 183–202.

Sun, S.-S. & McDonough, W. F. (1989). Chemical and isotopic systematics of oceanic basalts; implications for mantle composition and processes. In: Saunders, A. D. & Norry, M. J. (eds) *Magmatism in the Ocean Basins. Geological Society, London, Special Publications* **42**, 313–345.

Tabit, A., Kornprobst, J. & Woodland, A. B. (1997). The garnet peridotites of the Beni Bousera massif (Morocco): Tectonic mixing and iron–magnesium interdiffusion. *Comptes Rendus de l'Académie des Sciences, Série IIA* **325**, 665–670.

Takahashi, E. (1986). Melting of dry peridotite KLB-1 up to 14 GPa: implications on the origin of peridotitic upper mantle. *Journal of Geophysical Research* **91**, 9367–9382.

Takahashi, E., Shimazaki, T., Tsuzaki, Y. & Yoshida, H. (1993). Melting study of a peridotite KLB-1 to 6·5 GPa and the origin of basaltic magmas. *Philosophical Transactions of the Royal Society of London, Series A* **342**, 105–120.

Takahashi, E., Nakajima, K. & Wright, T. L. (1998). Origin of the Columbia River basalts: melting model of a heterogeneous plume head. *Earth and Planetary Science Letters* **162**, 63–80.

Takazawa, E., Frey, F. A., Shimizu, N. & Obata, M. (2000). Whole rock compositional variations in an upper mantle peridotite (Horoman, Hokkaido, Japan): Are they consistent with a partial melting process? *Geochimica et Cosmochimica Acta* **64**, 695–716.

Taylor, W. R. (1998). An experimental test of some geothermometer and geobarometer formulations for upper mantle peridotites with application to the thermobarometry of fertile lherzolite and garnet websterite. *Neues Jahrbuch für Mineralogie, Abhandlungen* **172**, 381–408.

Tiepolo, M., Vannucci, R., Oberti, R., Foley, S., Bottazzi, P. & Zanetti, A. (2000). Nb and Ta incorporation and fractionation in titanian pargasite and kaersutite: crystal-chemical constraints and implications for natural systems. *Earth and Planetary Science Letters* **176**, 185–201.

Van der Wal, D. & Bodinier, J. L. (1996). Origin of the recrystallization front in the Ronda peridotite by km-scale pervasive porous melt flow. *Contributions to Mineralogy and Petrology* **122**, 387–405.

Van der Wal, D. & Vissers, R. L. M. (1993). Uplift and emplacement of upper-mantle rocks in the western Mediterranean. *Geology* **21**, 1119–1122.

Van Westrenen, W., Blundy, J. D. & Wood, B. J. (2001). High field strength element/rare earth element fractionation during partial melting in the presence of garnet: Implications for identification of mantle heterogeneities. *Geochemistry, Geophysics, Geosystems* **2**, 1039.

Wells, P. R. A. (1977). Pyroxene thermometry in simple and complex systems. *Contributions to Mineralogy and Petrology* **62**, 129–139.

Willbold, M. & Stracke, A. (2006). Trace element composition of mantle end-members: Implications for recycling of oceanic and upper and lower continental crust. *Geochemistry, Geophysics, Geosystems* **7**, Q04004.

Witt-Eickschen, G. & O'Neill, H. S. (2005). The effect of temperature on the equilibrium distribution of trace elements between clinopyroxene, orthopyroxene, olivine and spinel in upper mantle peridotite. *Chemical Geology* **221**, 65–101.

Wood, B. J. & Blundy, J. D. (1997). A predictive model for rare earth element partitioning between clinopyroxene and anhydrous silicate melt. *Contributions to Mineralogy and Petrology* **129**, 166–181.

Wood, B. J., Blundy, J. D. & Robinson, J. A. C. (1999). The role of clinopyroxene in generating U-series disequilibrium during mantle melting. *Geochimica et Cosmochimica Acta* **63**, 1613–1620.

Yasuda, A., Fujii, T. & Kurita, K. (1994). Melting phase relations of an anhydrous mid-ocean ridge basalt from 3 to 20 GPa: Implications for the behavior of subducted oceanic crust in the mantle. *Journal of Geophysical Research* **99**, 9401–9414.

APPENDIX 1

Table A1: GPS sample locations and modal composition of Beni Bousera pyroxenites and peridotites analyzed in this study

Type	Sample	Modal proportions (%)										Coordinates
		ol	cpx	grt	opx	kel	sympl	sp	plag	amph	<1%	
I	6X	<1	20	–	80	–	–	<5	–	–	Fe–Ti-ox, serp	35 17 08·5 N, 4 53 39·8 W
I	9X	<1	20–25	–	75–80	–	–	<5	–	–	Fe–Ti-ox, serp	35 17 08·9 N, 4 53 39·7 W
I	CP2X	<1	25	–	70–80	–	–	<5	–	–	Fe–Ti-ox, serp	35 17 09·1 N, 4 53 40·4 W
I	CP2XX	<1	30–35	–	60–75	–	–	<5	–	–	Fe–Ti-ox, serp	35 17 09·1 N, 4 53 40·4 W
II	B15-3	5	20	–	65–75	–	–	10–15	–	–	py, Fe-ox	Section A
II	LU1	40–60	5–8	–	20–30	–	1–2	5	1	1	Fe–Ti-ox, serp	Section A
II	LU1*	40–60	5–8	–	20–30	–	1–2	5	1	1	Fe–Ti-ox, serp	Section A
IIIA	F2	–	75	10	–	10–15	–	–	–	2–3	py, Fe-ox	35 16 50·4 N, 4 54 40·2 W
IIIA	F6	–	–	–	–	–	–	–	–	–	–	35 16 45·4 N, 4 54 42·0 W
IIIA	G7	–	60–70	30–35	–	1–4	–	–	2	2–4	py, Fe-ox	35 16 13·3 N, 4 54 37·9 W
IIIA	P16	–	50–55	30–40	–	–	–	–	5–8	2	py, Fe-ox	35 15 53·7 N, 4 54 27·4 W
IIIA	P21	–	65–70	10–15	2–5	8–10	–	–	2	4	py, Fe-ox	35 16 39·5 N, 4 54 23·0 W
IIIA	B44	–	20–30	70–80	–	–	–	–	–	–	py, Fe-ox	Section B
PSD (IIIA)	BB91	–	50–60	40–50	–	3	–	–	–	3	graphite, py	–
IIIB	B3	–	40–45	–	30–35	10–15	–	1–3	1–2	1–2	py, Fe-ox	35 16 59·7 N, 4 54 32·3 W
IIIB	B7	–	80–85	–	5–10	8–10	–	2–3	–	–	py, Fe-ox	Section A
IIIB	B1	–	40–45	–	40–45	8–10	1–2	1	2	2	py, Fe-ox	Section A
IIIB	B11	–	70–80	–	7–10	8–10	–	1	1–2	1–2	py, Fe-ox	Section A
IIIB	B15	–	40–45	1–2	45–50	5–7	–	2	1	1	py, Fe-ox	Section A
IIIB	B6	–	70	–	20–25	5–9	–	2–4	–	–	py, Fe-ox	Section A
IIIB	B6-2	–	68–70	–	20–22	9	–	1	–	–	py, Fe-ox	Section A
IIIB	B9	–	45	5–8	45	–	–	2–3	–	1	py, Fe-ox	Section A
IIIB	P33		37	15	30	18	–	–	–	–	py, Fe-ox	35 16 55·4 N, 4 54 32·6 W
IV	B46-1	–	50–60	30–40	1–5	5	4	–	–	–	py, Fe-ox	Section B
IV	B47	–	50–60	30–40	–	8	–	–	–	–	py, Fe-ox	Section B
IV	B45	–	40–45	40	<5	3–5	–	–	5–8	–	py, Fe-ox	Section B
IV	B46-3	–	40–60	15–20	<10	5	–	5–8	–	–	py, Fe-ox	Section B
IV	B47-3	–	20–25	60–65	–	5–8	–	5–8	–	–	py, Fe-ox	Section B
Grt Lz	F3, F4	70–80	15–25	5–15	5–10	1–5	–	1–2	–	–	–	35 16 44·7 N, 4 54 43·5 W
Grt Lz	P1, P2	75–80	5–10	5–10	–	1–5	–	1–2	–	–	Fe–Ti-ox, serp	35 15 58·7 N, 4 54 45·4 W
Sp Lz	B51	75–80	10–15	–	15–20	–	–	3–5	–	–	Fe–Ti-ox, serp	Section B
Sp Lz	LZP	70–80	15–20	–	10–15	–	–	3–5	–	–	Fe–Ti-ox, serp	35 17 11·2 N, 4 53 40·9 W
Sp Lz	LZP*	75–80	10–15	–	10–15	–	–	2–4	–	–	Fe–Ti-ox, serp	35 17 11·2 N, 4 53 40·9 W
Sp Lz	LZP3	80–85	10–13	–	8–10	–	–	2–4	–	–	Fe–Ti-ox, serp	35 17 12·2 N, 4 53 33·8 W
Sp Lz	LZP4	70–80	15–20	–	8–10	–	–	2–4	–	–	Fe–Ti-ox, serp	35 17 12·1 N, 4 53 33·4 W
Sp Lz	B17	75–80	5–10	–	10–12	–	–	1–2	–	–	Fe–Ti-ox, serp	Section A
Sp Lz	B43, B43*	80–85	5–10	–	5–10	–	–	1–2	–	–	Fe–Ti-ox, serp	Section B
Sp Lz	B5	70–75	10–15	–	15–20	–	–	3–5	–	1	Fe–Ti-ox, serp	Section A
Sp Lz	BI7-2	70	10	–	15	–	–	3–5	–	–	Fe–Ti-ox, serp	Section A
Sp Lz	J10	75	8–10	–	14	–	–	3–4	–	–	Fe–Ti-ox, serp	35 16 28·8 N, 4 51 50·5 W
Sp Lz	J11	75–80	10	–	9–12	–	–	3–4	–	–	Fe–Ti-ox, serp	35 16 26·5 N, 4 51 50·2 W
Sp Lz	LZP2	70–80	5–8	–	10–15	–	–	1–3	–	–	Fe–Ti-ox, serp	35 18 21·7 N, 4 54 30·9 W

(continued)

Table A1: Continued

Type	Sample	Modal proportions (%)										Coordinates
		ol	cpx	grt	opx	kel	sympl	sp	plag	amph	<1%	
Sp Lz	B18	75–80	10–12	–	10–15	–	–	1–2	–	–	Fe–Ti-ox, serp	Section A
Sp Lz	P22	75–80	10–15	–	8–12	–	–	1–2	–	–	Fe–Ti-ox, serp	35 16 37·9 N, 4 54 18·8 W
Sp Lz	STO1	70–80	10–15	–	10–15	–	–	1–3	–	–	Fe–Ti-ox, serp	35 17 10·7 N, 4 53 33·8 W
Sp Lz	P8	74–78	5–10	–	5–10	–	–	1–3	–	–	Fe–Ti-ox, serp	35 15 51·6 N, 4 54 31·6 W
Sp Lz	B52, B52*	80–85	5–8	–	5–8	–	–	2–3	–	–	Fe–Ti-ox, serp	Section B
Sp Lz	G5	76	10–15	–	15–20	–	–	2–4	–	–	Fe–Ti-ox, serp	35 16 17·9 N, 4 54 35·6 W
Hz	B49	85–90	2–3	–	3–5	–	–	2–3	–	–	Fe–Ti-ox, serp	Section B
Hz	B18-3	80–85	2–3	–	5–10	–	–	1–2	–	–	Fe–Ti-ox, serp	Section A
Hz	B2	70–75	2–5	–	15–20	–	–	2–3	–	–	Fe–Ti-ox, serp	Section A
Hz	B4	80	5–7	–	8–10	–	–	2–4	–	1	Fe–Ti-ox, serp	Section A
Hz	B42, B42*	85–88	2–3	–	7–10	–	–	1–2	–	–	Fe–Ti-ox, serp	Section B
Hz	B50	80–85	2–3	–	5–10	–	–	1–2	–	–	Fe–Ti-ox, serp	Section B
Dunite	9 H	93–95	–	–	1–2	–	–	3–5	–	–	Fe–Ti-ox, serp	35 17 08·9 N, 4 53 39·7 W
Dunite	B16	90–95		–	5–7	–	–	2–3	–	–	Fe–Ti-ox, serp	Section A
Dunite	B20	95–98	–	–	–	–	–	2–5	–	–	Fe–Ti-ox, serp	Section A
Dunite	BB06-2	90–95	–	–	–	–	–	5–7	–	1–2	Fe–Ti-ox, serp	Section A
Dunite	B21	87–90	1–3	–	5–7	–	–	2–3	–	–	Fe–Ti-ox, serp	Section A

Estimated modal amount ranges correspond to estimated values from field samples and thin section observations. Pyroxenite types: I, Cr-diopside websterites; II, spinel websterites; IIIA, garnet clinopyroxenites; IIIB, garnet kelyphite websterites; IV, garnet metagabbros; PSD, graphite pseudomorphs after diamond. Peridotites: Grt Lz, pseudo-grt lherzolites; Sp Lz, spinel lherzolites; Hz, harzburgites; dunites. Coordinates (WGS 84, degrees minutes seconds): section A (35°17′02·5″N, 4°53′41·5″W); section B (35°15′05·3″N, 4°53′47·1″W). ox., oxides; serp, serpentine; py, pyrite, chalcopyrite.

APPENDIX 2

Table A2: Selected EMPA results for major elements in olivine

Sample:	LZP4	LZP2	B17	B21	B48
Type:	Sp Lz	Sp Lz	Sp Lz	Dunite	Dunite
No.:	6	3	3	8	3
SiO_2	40·4 (3)	38·2 (3)	41·0 (3)	40·4 (12)	40·1 (1)
FeO	9·6 (2)	9·8 (4)	10·8 (2)	9·0 (8)	9·2 (1)
MnO	0·13 (2)	0·14 (1)	0·15 (2)	0·00 (0)	0·13 (2)
NiO	0·39 (3)	0·38 (2)	0·38 (4)	0·41 (5)	0·43 (4)
MgO	49·4 (11)	50·8 (8)	49·6 (1)	50·1 (9)	49·7 (7)
CaO	0·02 (1)	0·02 (0)	0·02 (1)	0·02 (2)	0·02 (1)
Total	100·00	99·35	102·00	99·99	99·59
X_{Mg}	0·897	0·898	0·884	0·904	0·901

Na_2O, TiO_2, Al_2O_3, Cr_2O_3 below detection limit.

APPENDIX 3

Table A3: Plagioclase (B45, B7) and amphibole (G7) major element concentrations (wt %)

Sample:	G7	B45	B7	B7[1]
Type:	IIIA	IV	IIIB	IIIB
No.:	3	5	3	3
SiO_2	40·7 (1)	58·6 (3)	54·8 (2)	52·5 (3)
TiO_2	2·12 (4)	–	–	–
Al_2O_3	14·26 (16)	26·45 (8)	28·89 (15)	31·30 (14)
FeO	11·09 (17)	0·06 (2)	0·22 (4)	0·35 (1)
MnO	0·15 (0)	–	–	–
MgO	13·75 (25)	–	–	–
CaO	11·01 (6)	8·99 (20)	10·09 (17)	12·83 (8)
Na_2O	3·37 (3)	6·22 (18)	5·63 (37)	4·44 (7)
K_2O	0·13 (1)	0·23 (2)	0·02 (0)	0·01 (0)
Total	96·70	100·64	99·75	100·99
An		0·438	0·497	0·615
Alb		0·549	0·502	0·385
K-fspar		0·013	0·001	0·001

[1]Phase associated with kelyphite.
An, anorthite; Alb, albite; Kfspar, K-feldspar.

APPENDIX 4

Table A4: Cpx and grt LA-ICP-MS average detection limits (LOD) and limits of quantification (LOQ) given in ppm

	Cpx (LOD)	Grt (LOD)	Cpx (LOQ)	Grt (LOQ)
Cs	0·021		0·070	–
Rb	0·057	–	0·190	–
Ba	0·202	–	0·673	–
Th	0·028	–	0·093	–
U	0·026	–	0·087	–
Nb	0·045	–	0·150	–
Ta	0·032	–	0·107	–
La	0·027	0·022	0·090	0·073
Ce	0·028	0·022	0·093	0·073
Pb	0·072	0·058	0·240	0·193
Pr	0·023	0·018	0·077	0·060
Sr	0·049	0·035	0·163	0·117
Nd	0·151	0·111	0·503	0·370
Hf	0·125	0·096	0·417	0·320
Zr	0·371	0·346	1·237	1·153
Ti	1·7	2·2	5·7	7·3
Sm	0·178	0·140	0·593	0·467
Eu	0·053	0·039	0·177	0·130
Gd	0·194	0·157	0·647	0·523
Tb	0·030	0·023	0·100	0·077
Dy	0·128	0·095	0·427	0·317
Ho	0·031	0·024	0·103	0·080
Er	0·145	0·111	0·483	0·370
Yb	0·201	0·157	0·670	0·523
Lu	0·033	0·027	0·110	0·090

APPENDIX 5

Cpx and opx porphyroclast profiles and secondary neoblasts for Type-IIIB pyroxenites. Data given in Electronic Appendix 2 and 4.

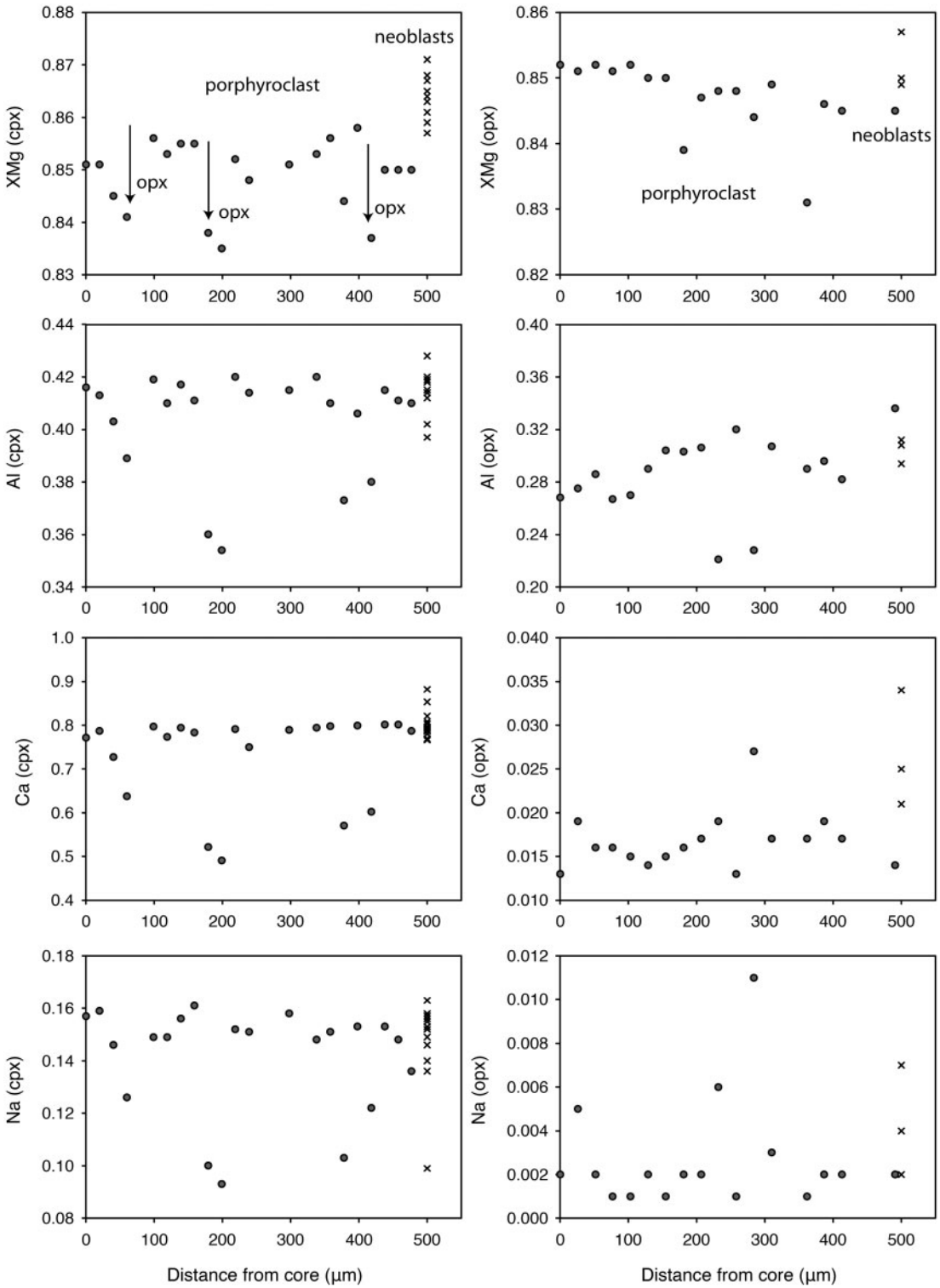

APPENDIX 6

Trace element distribution between cpx porphyroclast host and opx exsolution lamellae for Type-I and -IIIB pyroxenites. Data given in Table 8 for porphyroclasts and Electronic Appendix 8 for exsolution lamellae.

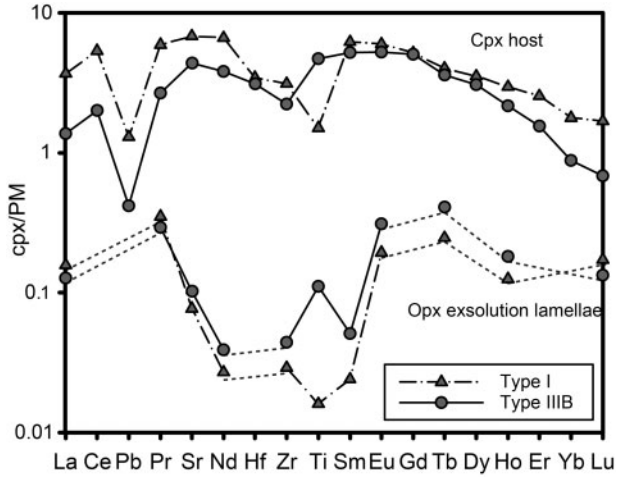

APPENDIX 7

Calculated trace element partitioning between cpx and garnet pairs in garnet-bearing pyroxenites compared with experimental and natural data. Data sources: H (94), anhydrous experiments from Hauri *et al.* (1994); H&K (97), from Harte & Kirkley (1997); G (00), hydrous experiments from Green *et al.* (2000).